Development of Portable Magnetostrictive Biosensor System

by

Kewei Zhang

A dissertation submitted to the Graduate Faculty of
Auburn University
in partial fulfillment of the
requirements for the Degree of
Doctor of Philosophy

Auburn, Alabama
December 13, 2010

Keywords: magnetostrictive particle (MSP), resonance behavior, biosensors, blocking agent, phage/antibody, frequency-domain, time-domain

Approved by

Zhongyang Cheng, Chair, Associate Professor of Materials Engineering
Jeffrey Fergus, Professor of Materials Engineering
DongJoo Kim, Associate Professor of Materials Engineering
Dongye Zhao, Associate Professor of Civil Engineering

Abstract

There is an urgent need for the detection technologies that can rapidly detect/monitor the presence of pathogens in food. Various detection technologies have recently been developed and investigated. Among these technologies, magnetostrictive particle (MSP)-based technology provides many unique advantages over others. For example, MSP is a great candidate for in-field tests. This technology is based on a mechanical resonator, whose resonance frequency changes with the binding of pathogens onto its surface. This resonator is actuated by use of the magnetostrictive effect and its vibration is sensed using a magnetic signal. The surface of an MSP is coated with a sensing element that reacts with the target of interest with a strong specificity. Phage based MSP biosensors for the detection of *B. anthracis* and *S. typhimurium* have been developed.

In this research, all aspects of the MSP detection technology are studied to fully develop the technology. First of all, a fundamental study was carried out to determine the influence of the size/dimension of an MSP on its resonance behavior. To use the widely exploited and accepted antibodies, a methodology is here introduced to effectively immobilize antibodies onto the surfaces of MSPs. Sensors for the detection of different pathogenic bacteria are developed using antibodies as a sensing element. To develop the MSP technology for in-field detection, handheld interrogation devices are here studied. Finally, to increase the sensitivity of the MSP sensors, MSPs in micro/nano-size

including bar- and tube-shapes have been fabricated.

It is found in the resonance behavior study that the apparent acoustic velocity of the MSP is dependent on the length and length to width ratio rather than a constant. It hasalso been found that although the medium has a very complicated influence on the resonance behavior, the resonance frequency of an MSP is still linearly dependent on the inverse length of the MSP. However, the apparent acoustic velocity changes with the length and length/width ratio. A new method based on using the resonance frequencies of an MSP at different harmonic modes is introduced here to determine the surface roughness of the MSP.

Thiol groups were introduced onto antibodies after modification. The modified antibodies for *E. coli*, *S. aureus,* and *L. monocytogenes* were successfully immobilized onto the gold-coated MSPs. These antibody-immobilized MSPs exhibited great performance as biosensors. For example, the biosensors using an MSP the size of 1.0 mm x 0.3 mm x 30 μm shows a detection limit of less than 10^2 cfu/ml for detection of the pathogenic bacteria in water. In the experiments, a reference sensor was used to monitor the non-specific binding, and a way to reduce the non-specific binding was studied by using different block agents.

Both frequency-domain and time-domain technologies were exploited in the development of handheld interrogation device. An indirect approach was introduced in the frequency-domain technology. Based on its principle, a circuitry was designed and a circuit was built. The circuit was examined using the MSPs with different sizes. The results show that this indirect approach works well in the characterization of MSP sensors. Additionally, a method to further enhance the signal was introduced. All of the numerical

simulation results were consistent with the experimental results. Regarding the time-domain technology, a pulse was used to actuate an MSP resonator, and the response of the MSP was analyzed using fast Fourier transform (FFT) to determine the resonance frequency. It was also experimentally proved that handheld interrogation devices based on either frequency-domain or time-domain technologies can be used for the characterization of multiple MSP-sensors simultaneously. Both devices were validated by using them to characterize the MSP sensors for the detection of pathogenic bacteria in water.

For the fabrication of the micro/nano-sized MSPs, a Co-Fe-B alloy was selected. Amorphous Co-Fe-B in the form of thin films as well as nano-bars and nano-tubes were fabricated using an electrochemical deposition method.

Acknowledgements

I would like to express my deepest appreciation to my advisor Dr. Z.-Y. Cheng for his expert guidance and persistent help during my graduate studies at Auburn University. Without his guidance and persistent help this dissertation would not have been possible. I would like to emphasize that his influence on me was not only in acquiring scientific knowledge but also as a person.

I would like to give my sincere thanks to my committee members, Dr. Jeffrey W. Fergus, Dr. Dong-Joo Kim, Dr. Dongye Zhao for their generous guidance and insightful suggestions, to Dr. Byran A. Chin for providing the bio-safety laboratory, and to Dr. Tung-Shi Huang for his helpful discussions and advice. Thanks also go to Mrs. I-Hsuan Chen for her help in the biological sample preparations, Mr. L.C. Mathison and Mr. Roy Howard for the general technical support and Mrs. Alison Mitchell for the writing/formatting corrections of the papers and dissertation.

Thanks also go to my colleagues and friends, Dr. Anxue Zhang, Dr. Suiqiong Li, Dr. Xiaobing Shan, Dr. Liling Fu, Peixuan Wu, Lin Zhang, Levar Odum, Xu Lu, Dr. Jing Hu, Dr. Shichu Huang, Shin Horikawa, Wen Shen, Michael L. Johnson, Yating Chai, Dr. Yuhong Wang, Dan Liu, Zijie Cai for all their help and suggestions. I especially would like to give thanks to Dr. Anxue Zhang for building the devices, Dr. Suiqiong Li for analyzing the resonance behavior, Dr. Liling Fu for modifying antibodies.

Most importantly, I can not give enough thanks to my wonderful family: my father

Shaoqin Zhang, my mother Ju Duan and also my older brother Kehao Zhang for their everlasting love, emotional support, encouragement and strength not only during my studies but also throughout my life. Last but not least, I would like to give my thanks to my sister-in-law Xuejie Chen for preparing delicious food everyday during my studies.

Table of Contents

List of Figures

List of Tables

List of Abbreviations

FDA	Food and drug administration
CDC	Centers for disease control and prevention
ELISA	Enzyme-linked immunosorbent assay
PCR	Polymerase chain reaction
DNA	Deoxyribonucleic acid
SPR	Surface plasmon resonance
ISE	Ion-selective electrode
ISFET	Ion-sensitive field effect transistors
AW	Acoustic wave
QCM	Quartz crystal microbalance
TSM	Thickness shear microbalance
SAW	Surface acoustic wave
IDT	Interdigital transducer
APM	Acoustic wave plate mode
SH-APM	Shear-horizontal acoustic wave plate mode
FPW	Flexural plate wave
MC	Micro-cantilever
MSMC	Magnetostrictive micro-cantilever
AC	Alternating

PAbs	Polycolonal antibodies
MAbs	Monoclonal antibodies
MSP	Magnetostrictive particles
NSB	Non-specific binding
BSA	Bovine serum albumin
PBS	Phosphate buffered saline
TBS	Tris buffered saline
PC	Personal computer
SEM	Scanning electron microscopy
EDTA	Ethylenediaminetetraacetic acid
DUT	Device under test
GUI	Graphical user interface
FCC	Face centered cubic

List of Symbols

S_m	Mass sensitivity
Q	Quality merit factor
f_n	nth harmonic resonance frequency
L	Length
W	Width
v	Acoustic velocity
E	Young's modulus
ρ	Density
σ	Poisson ratio
m	Power value
$U^*(\omega)$	Potential through DUT
$U_r^*(\omega)$	Potential through a reference
$Z^*(\omega)$	Impedance of DUT
$Z_r^*(\omega)$	Impedance of a reference
F	Faraday
H	Henry
Ω	Ohm
f_r	Resonance frequency
f_{ar}	Anti-resonance frequency

CHAPTER 1

INTRODUCTION

1.1 Introduction to pathogenic bacteria and food-borne illness

Food safety and security are topics of worldwide public concern due to various widespread food-borne disease outbreaks causing potential threats to public health from food products. The contamination of food products by pathogenic bacteria results in many outbreaks of food-borne disease and product/food recalls, which cost the food industry greatly each year. According to a report by the U.S. Food and Drug Administration (FDA), the annual costs of food-borne diseases in the United States are estimated to be between $10 and $83 billion [1]. It was estimated that about 76 million cases of food-borne illness, 324,000 hospitalizations, and 5200 deaths are caused by microbial pathogens each year in the United States [2]. Therefore, food-borne diseases caused by pathogenic bacteria have become an important public health concern worldwide. **Table 1-1** gives the statistics on outbreaks related to some pathogenic bacteria in the United Sates.

1.1.1 Foodborne pathogenic bacteria

There are many pathogenic bacteria that may contaminate food and cause foodborne diseases. Four strains of bacteria are shown in **Table 1-1** since these are the bacteria that account for most of the foodborne disease outbreaks. Backlground information about these bacteria is shown below.

***Salmonella typhimurium* (*S. typhimurium*):** *Salmonella* is a gram-negative, rod-shaped

bacterium that is widely distributed in nature and may cause gastroenteritis and enteric fever in many food poisoning cases [3]. According to the Centers for Disease Control and Prevention (CDC), it is estimated that 1.4 million human illnesses and 400 deaths are caused by *Salmonella* infections annually in the United States [4]. Infections with *salmonellosis* alone account for $1 billion in medical costs per year [5].

Table 1-1. Microorganism-specific food source profile, by proportion (%) for foodborne outbreaks reported between 1988 and 2007 [30].

Source of Microorganism	***E. coli***	***L. monocytogenes***	***S. typhimurium***	***S. aureus***
Total Number of Outbreaks	389	53	270	182
Produce	19.5	1.9	3.6	3.3
Multi-ingredient foods	11.8	5.7	10.7	22
Seafood	0.5	11.3	4.8	3.3
Beef	44.2	5.7	8.5	13.7
Pork	0.5	11.3	6.7	21.4
Dairy products	9.8	41.5	11.9	11
Chicken	1	1.9	10.4	8.2
Other meats	6.9	13.2	6.7	4.4
Bakery items	1		7.4	5
Beverages	4.4		1.1	
Turkey+ other poultry	0.3	7.6	2.2	3.3
Eggs			18.2	3.9
Other foods			1.5	0.6
Total	100%	100%	100%	100%

In 2009, more than 700 persons were infected with an outbreak of *Salmonella typhimurium* from 46 states due to contamination of peanut butter and other peanut-containing products [6]. Poultry, egg, meat and dairy products are the most common food vehicles of the infection of *salmonella* [7]. Human *salmonellosis* can also be associated with fresh fruits and vegetables. Several large outbreaks of *salmonellosis* have been linked to fresh fruits and vegetables. In the United Kingdom, 143 cases were reported

after consumption of bean sprouts contaminated with *Salmonella* [8]. Therefore, *Salmonella typhimurium* is considered to be one of the great threats to food safety.

***Escherichia coli* (*E. coli*):** *E. coli* are gram negative rod-shaped bacteria that were first identified in the intestinal flora of infants in 1885 [9]. *E. coli* are serotyped based on the O (somatic), H (flagellar), and K (capsular) surface antigen profiles [10]. A specific combination of O and H antigens defines a serotype of *E. coli*. The *E. coli* strain is inagglutinable and has an O antiserum; after heating it becomes agglutinable and has a K antigen [10].

Though most *E. coli* strains are not harmful, a predominant serotype *E. coli O157:H7* is able to cause a range of food-borne diseases such as hemolytic colitis, diarrhea, hemolytic uremic syndrome, and thrombotic thrombocytopenic purpurea by producing one or more related potent toxins , called Shiga toxin [11]. Ground beef, lettuce, salami, and unpasteurized milk and fruit juice are the potential sources for a food-borne outbreak of *E. coli O157:H7* [12]. According to a CDC report, a recent food-borne disease outbreak of *E. coli O157:H7* in Rocky Mountain Natural Meats bison meat related products caused six illnesses in Colorado and New York with about 66,776 pounds of bison meat recalled [13].

***Staphylococcus aureus* (*S. aureus*):** The *Staphylococcus* genus can be categorized further as *S. aureus* and *S. epidermidis*. *Staphylococcus epidermidis* is much less harmful than *Staphylococcus aureus* (*S. aureus*). They both are able to stand a temperature up to 60 ºC for a half hour and remain alive when refrigerated for several months [14]. *S. aureus* are facultative anaerobic, gram-positive bacteria that were discovered in the 1880s [15]. *S. aureus* are able to live in food, on environmental surfaces, in humans, and in animals and

therefore can cause a variety of human disease infections, ranging from minor infections of the skin to post-operative wound infections [16]. Meat and meat products, poultry and egg products, salads, and milk and dairy products are all potential sources of food-borne diseases caused by *S. aureus* [16]. The typical symptoms are vomiting, diarrhea, prostration, abdominal cramps, retching, and weakness which usually last a couple of hours after consumption of foods containing staphylococcal toxins [17]. A recent multistate food-borne outbreak of *S. aureus* associated with pizza, fish sandwiches, BBQ pork, fried chicken, and roasted turkey caused more than 100 illnesses [18].

***Listeria monocytogenes* (*L. monocytogenes*):** The bacterium *L. monocytogene* was first recognized in 1924 [19]. *L. monocytogene* is a gram-positive, rod shape pathogen that is widely distributed in nature and in the intestinal tracts of animals and humans [20]. *Listeriosis* caused by bacteria of the genus *Listeria* may result in severe illness, fetal death and miscarriage. The genus *Listeria* includes six species: *L. monocytogenes*, *L. innocua*, *L. welshimeri*, *L. seeligeri*, *L. ivanovii and L. grayi*. Among these, *L. monocytogenes* is the major pathogenic species in both animals and man [21]. Human *Listeriosis* is usually associated with contaminated food such as soft cheese [22], cooked meat products [23] and even in frozen foods due to the ability to survive in refrigeration temperatures [24]. In the United States, about 2,500 cases of persons with serious illness and 500 cases of death involving with *Listeriosis* were reported to the CDC (Centers for Disease Control and Prevention) each year.

Numerous food-borne outbreaks of *L. monocytogenes* have been documented worldwide [25, 26]. In the 1950s, a large outbreak of *Listeriosis* in East Germany occurred which appears to be one of the first documented reports of *Listeriosis* due to

food consumption. In 1985, another outbreak of *Listeriosis* occurred in California due to the consumption of a Mexican-style soft cheese produced by a company in California. It was discovered that some raw milk at the manufacturing plant was not pasteurized [27]. An outbreak associated with raw milk soft cheese was also reported in France in 1995 [28]. In 2002, the multi-state outbreak of *L. monocytogenes* that occurred in United States caused 46 culture-confirmed cases including seven deaths and three fetal deaths due to consumption of contaminated turkey deli meat [29]. Although food-borne *Listeriosis* is rare, the associated mortality rate is high among those who are most at-risk.

1.1.2 Infectious dose and detection of bacteria

Humans and animals are subjected to the food-borne infections usually by ingestion of the pathogen in contaminated food or water. After the pathogenic cells move to the intestine, they colonize and cross the intestinal barrier causing local tissue damage and inflammation and possibly spreading to other sites. The infectious dose and incubation periods may vary depending on the immunological ability of the host and the infectivity of the pathogens, as listed in **Table 1-2** [31, 32].

Table 1-2. Infectious dose and incubation periods of the four most common food-borne pathogens.

Pathogens	**Infectious dose**	**Incubation period**
S.typhimurium	$>10^5$cfu	6-24 hrs
E.coli	50-100 cfu	3-9 days
S.aureus	10^5-10^8 cfu	0.5-8 hrs
L.monocytogenes	10^2-10^3 cfu	7-14 days or longer

Since food-borne disease caused by bacterial infection is always an important concern, inexpensive devices/tools need to be developed for the rapid detection of bacterial contamination of food, industrial waste water, and clinical samples. An effective bacterial detection technique should meet a number of criteria, such as fast response time and high

sensitivity and specificity [7-9]. In addition, a technique capable of on-site detection is also highly desirable for food security control. As shown in **Table 1-2**, the infectious dose changes over a great range. Therefore, different sensitivities and detection limits may be needed for sensors designed to detect different bacteria.

Over the last few decades, a large number of detection techniques have been developed. In general, these detection techniques can be divided into two categories: conventional detection techniques and biosensors. The conventional detection techniques are widely used in current biological laboratories and many of these techniques are considered to be the gold-standard techniques for the detection of the bacteria. Biosensors are new and are considered to be the next generation technology since they have many advantages over conventional techniques. The development of high-performance biosensors has been a hot topic in the last two decades.

1.2 Conventional bacterial detection methods

The most widely used conventional detection techniques are plate counting methods, enzyme-linked immunosorbent assay (ELISA), and polymerase chain reaction (PCR). These techniques are described below.

1.2.1 Plate counting methods

In this method, the sample suspension is incubated on a plate of agar-based media that contains essential nutrients and thus forms a number of colonies. By counting the number of colonies on the plate, the total number of bacteria is calculated. Plate counting techniques can be divided into spread plate method, pour plate method, and drop plate method as shown in **Figure 1-1**.

For the spread plate method, serial dilutions of sample suspension are used and an

inoculum of each dilution is spread rapidly over each individual agar surface using a flame-sterilized nichrome wire. These plates are then incubated at a suitable temperature (typically 25-37^{o}C) for one to two days [34]. After incubation, plates inoculated with sample dilutions yielding a number of colonies are ready for counting. The pour plate method is very similar to the spread method except that each dilution is mixed thoroughly with the sterile agar media, then a certain amount of sterile water is poured on them [34]. For the drop plate method, each plate is divided into several sectors, and 1 drop of sample dilution is delivered to each sector with a calibrated Pasteur pipette [35].

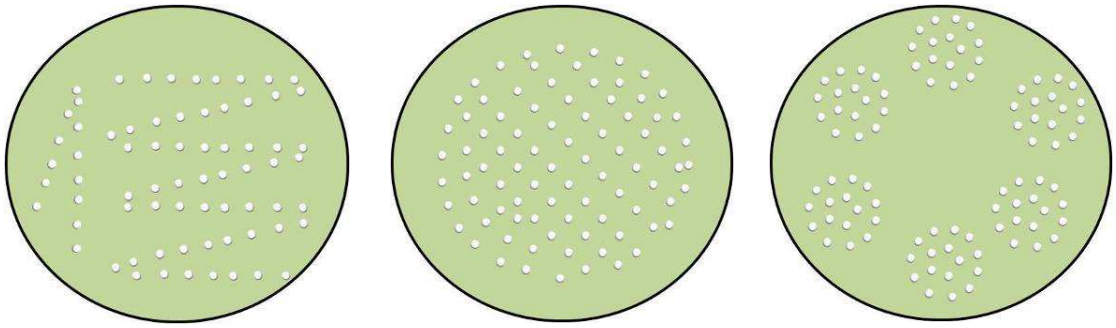

Figure 1-1. Schematic of different colony counting techniques where the white dots represent the bacteria colonies and the green circles represent the agar plate. (a) spread plate method, (b) pour plate method, and (c) drop plate method [33].

Among the three methods, the drop plate method is the most preferable because more counts can be obtained on one plate since the division of one plate could be equivalent to producing several spread or pour plates [36]. Also, different dilutions could be placed on one plate. Even though these methods are time consuming and need well trained personnel, they are still frequently used for the purpose of obtaining isolated cultures [36]. Various commercial instruments are currently available to facilitate

counting the colonies, such as Celigo™ Cytometer from Cyntellect Inc; aCOLyte; ProtoCOL 2 from Synoptics Ltd; and ColonyDoc-It Imaging Station from UVP, LLC.

1.2.2 Enzyme-linked immunosorbent assay (ELISA)

Since ELISA was invented by Peter Perlmann and Eva Engvall at Stockholm University in 1971, it has become one of the most widely used techniques for detecting antibodies and a wide variety of antigens [37, 38] in worldwide. ELISA was developed based on the use of enzyme markers to visualize the antibody-antigen binding reaction. There are three main types of ELISA: (1) Direct ELISA, (2) Indirect ELISA, and (3) Sandwich ELISA. The procedures of the three types of ELISA are shown in **Figure 1-2** (a), (b), and (c), respectively.

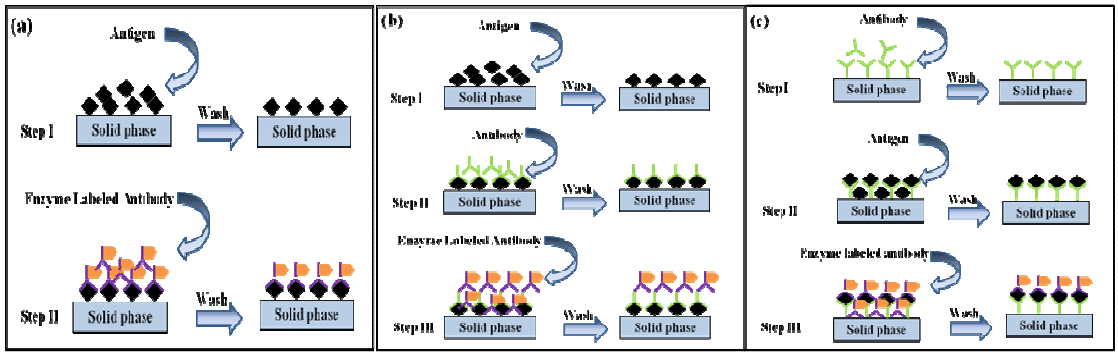

Figure 1-2. Illustration of enzyme labeled antibody ELISA (a) Direct ELISA (b) Indirect ELISA, and (c) Sandwich ELISA [39].

Direct ELISA is the simplest form of ELISA. In this method, the target antigens are first purified and added to the surface of a solid phase, typically a plate well. After the unbound antigens are washed away, enzymes-labeled antibodies are added and react with the bound antigens. After removing the unbound antibodies by washing, a colorless substrate solution such as pnitrophenylphosphate (pNPP), which can be catalyzed by the enzyme, is added and results in a colored product [40]. Finally, the antigen population/concentration is determined by the product color using a spectrophotometer.

In indirect ELISA, two types of antibodies are required. The first type antibodies (also called capture antibodies) are specific to the antigens while the second type is specific to the first type. The antigens are first purified and added to the surface of a solid phase, typically a plate well. After the unbound antigens are washed away, the first type antibodies which are unlabeled by enzymes are added and react with the antigens. Then, after the unbound first type antibodies are washed away, the enzyme labeled second type antibodies, which are specific to the first type antibodies, are added and react with the first type antibodies. After the unbound second type antibodies are washed away, a colorless substrate solution which can be catalyzed by the enzyme is then added and results in a colored product [40]. Lastly, the antigen population is determined by the product color using a spectrophotometer.

In sandwich ELISA, two types of antibodies, which are both specific to the target antigens are required. Firstly, the first type antibody is immobilized to the surface of the solid phase which is followed with a washing step. After the unbound antibodies are washed away, the target antigens are then added. After removing the unbound antigens by washing, enzymes labeled second type of antibodies are added and react with the antigens, forming a “sandwich”. Finally, after adding the colorless substrate solution, the antigen population is determined by the product color using a spectrophotometer.

In order to increase the precision of the experimental results, blocking agents, such as casein or bovine serum albumin, are usually used to prevent the non-specific binding of antibodies or antigens by filling up the vacant sites that are not covered by the antibodies or antigens. ELISA is considered sensitive and specific, but this technique is relatively time consuming due to the requirement of several washing and incubation steps

and requires well-trained personnel [41].

1.2.3 Polymerase chain reaction (PCR)

Since it first appeared in 1985 as a method for the diagnosis of sickle cell anemia, a lot of research efforts have been focused on the polymerase chain reaction (PCR) method for microbial detection [42, 43].

The PCR method is based on exponential amplification of a specific DNA sequence of interest. There are three steps in one cycle: (1) thermal denaturation, (2) primer annealing, and (3) Primer extension as shown in **Figure 1-3** [44]. In the first step, the double-stranded DNA of the target is denatured and separated into two single DNA strands by heating to a temperature above 90°C (typically 94^{o}C) as shown in **Figure 1-2A**. In the second step, two single-stranded primers, usually ranging from 15 to 30 nucleotides, are used for the complementary building blocks of the target sequence. A primer for each target sequence on the end of the sequence is needed so that the DNA can be copied simultaneously in both directions as shown in **Figure 1-3B**. In order to prevent the two strands from binding back to each other, excess primers are added so that they will bind to the target DNA. The annealing temperature and time depends on the base composition, length, and concentration of primers. The annealing temperature is usually above 50^{o}C (typically 55^{o}C). In the third step, DNA primers are incubated at a higher temperature above 70^{o}C (typically 72^{o}C) with DNA polymerase and this forms a new copy of the target DNA as shown in **Figure 1-3C** [45]. By repeating the above process, the target DNA can be further duplicated as shown in **Figure 1-3D**. Usually, after 30-40 rounds of amplification, several hundred million fold amplification of the specific target sequences can be achieved [46].

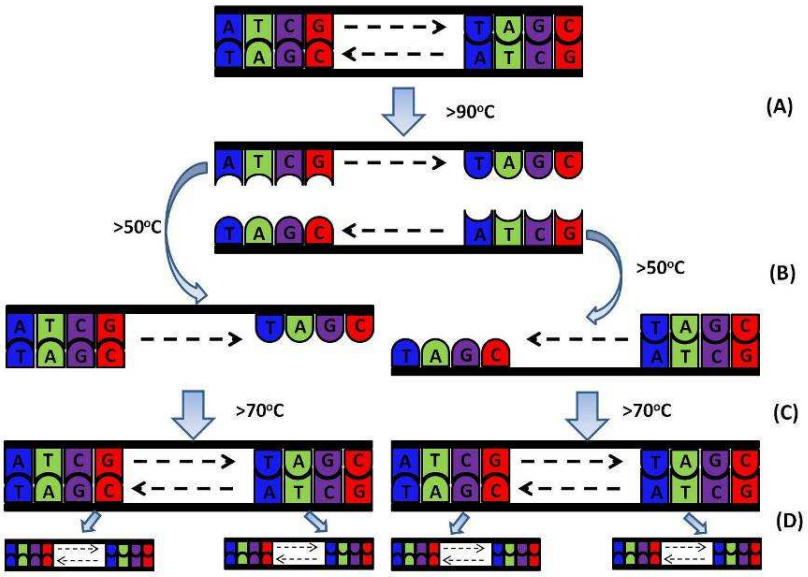

Figure 1-3. An illustration of the Polymerase chain reaction (PCR): (A) Thermal denaturation, (B) Thermal annealing, (C) Primer extension, and (D) New cycles [44, 45].

PCR could be a very fast technique once the target DNA is obtained, however, it has some limitations. Usually, the sample bacterial cells are obtained by using a toothpick to scrape under the fingernails, swabbing the inside of the mouth or from the roots of plucked hair and so on. Then the DNA is released from the cells and then obtained when the bacterial cell walls are broken by using vigorous shaking or vortexing. This technique is also sensitive with its ability to detect as little as 10 pg of the target DNA in the presence of 1.25 µg of genomic DNA [46]. However, a false result may occur if there is an insufficient or unspecific amplification or if the primers are homologous to other sequences than the target genes. In addition, the targets cannot be directly detected by using PCR since it is only used to amplify the targets. Therefore, PCR has to be combined with other techniques to visualize the detection. Conventional techniques such as agarose gel electrophoresis and Sounthern blot work very well but do not readily give a qualitative result [46].

Recently, real-time PCR, which is able to give a fast quantitative result, has been developed. It is a kinetic approach and can finish the measurement when the reaction is still in the early stages. Currently, many commercial real-time PCR instruments are available such as the ICycler® from BioRad [47].

1.3 Biosensors

In recent decades, biosensors have become increasingly important bioanalytical tools in the pharmaceutical, biotechnology, food, and other industries. A lot of research has been devoted to the development of biosensors that are sensitive, cost effective, and easy to operate for the rapid detection of interested target species in the analytes.

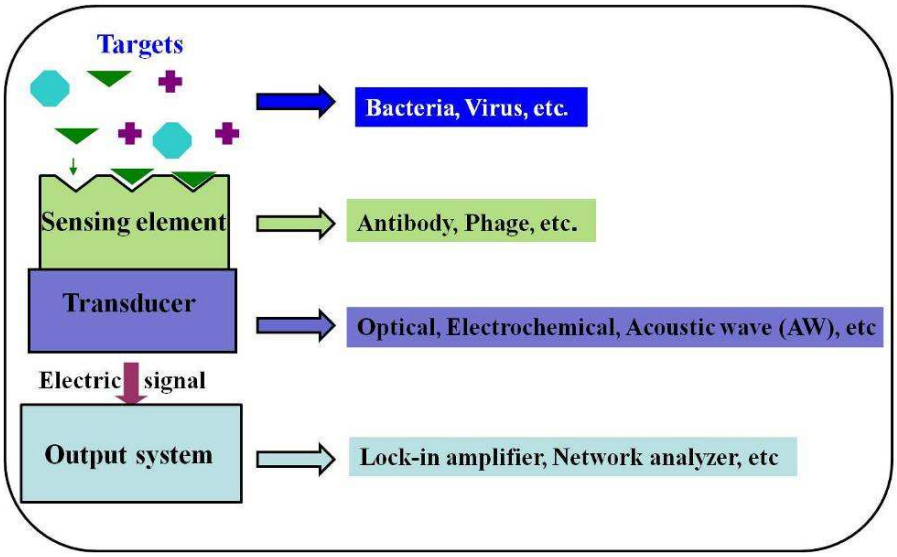

Figure 1-4. Schematic illustration of a typical biosensor system.

A biosensor is an analytical device that can convert a biological stimulus into an engineering measurable signal. In general, it consists of three parts: a sensing element (or biomolecular recognition unit), a transducer (or sensor platform), and an output system (or interrogation system) as shown in **Figure 1-4**. The sensing element (such as antibodies and phages) can react with specific targets (such as antigens and viruses),

while this reaction can be converted to an engineering measurable signal by the transducer [48]. The transducers can be classified based on the principle of the transducers, such as optical, electrochemical, or acoustic wave (AW)-based biosensors.

1.3.1 Optical biosensors

Optical biosensors detect targets by measuring the changes in the light behavior, which are caused by an interaction between electromagnetic wave and biological molecules such as proteins, cells, and DNA. Different measuring techniques have been applied including absorbance, fluorescence, luminescence, and reflectance. The measuring principles are listed in **Table 1-3**.

Absorbance technique: The absorbance technique is the simplest method of optical biosensing. When using a given light at a specific wavelength, the absorbance of the analyte changes with the population of the analyte. The extent of adsorption depends on many factors including the adsorption cross-section of the transducing molecule, the optical path length and the illumination wavelength [49, 50].

Fluorescence technique: In the fluorescence technique, when molecule species are excited by light at a specific wavelength, they will re-emit light with a longer wavelength called fluorescence. For biosensing applications, the targets can be detected by measuring the change in fluorescent intensity, wavelengths, and lifetime [49, 51]. However, there are limited types of naturally occurring biological molecules with intrinsic fluorescence. Therefore, fluorescent tags are usually used for providing fluorescent light.

Table 1-3. Working principle of optical detection [49].

Optical parameter	Relationship	Notes
Absorbance	Lambert-Beer's law $A = \log {I_o}/{I} = \varepsilon c l$	l, optical path length ε, molar absorptivity I_o, intensity of the incident light I, intensity of the transmitted light c, concentration of the absorbing species
Luminescence	Stern-Volmer equation ${I_o}/{I} = 1 + k_{SV}[Q] = {\tau_o}/{\tau}$	$[Q]$, quencher concentration k_{SV}, Stern-Volmer constant τ_o, luminescence lifetime without quencher τ, luminescence lifetime with quencher
Fluorescence	$I_f = (I_o(1 - 10^{-\varepsilon l c}))\varphi$	I_f, intensity of the fluorescent light φ, quantum yield ε, molar absorptivity l, optical path length
Reflectance	${2(1-R)}/{2R} = f(R) = \varepsilon c / S$	R, reflectance $f_{(R)}$, Kubelka-Munk function S, Scattering coefficient

Luminescence technique: In the luminescence technique, the target population is determined by detecting change in luminescence intensity, phase, or lifetime [49]. The construction of luminescence-based biosensors is similar to that of absorbance-based transducers. Excitation light is guided to the recognition element which is exposed to the target analyte. The fluorescence is then collected by the detection system [50].

Surface plasmon resonance (SPR): Currently, the most-often used optical biosensor transducer is based on the SPR technique [52, 53]. It is an optical phenomenon that is sensitive to changes in the optical properties of the medium close to a metal surface. If a monochromatic and polarized light passes through the interface between two media, such as a metal and other dielectric, charge-density oscillation may occur [54]. This

phenomenon is known as surface plasmon resonance (SPR). There are four basic methods to excite the SPR: prism coupling, waveguide coupling, fiber optic coupling, and grating coupling, among which, prism coupling is the most convenient SPR configuration [55].

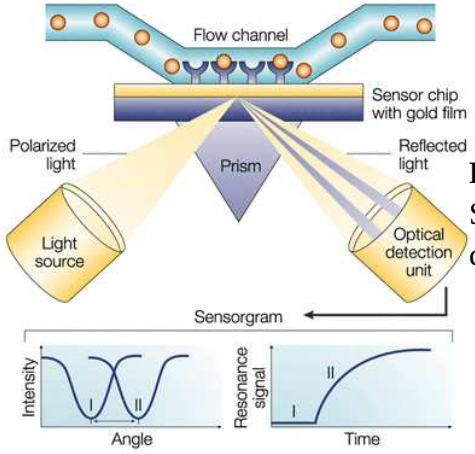

Figure 1-5. A typical prism-based Surface plasmon resonance biosensor configuration [56].

A typical prism-based SPR biosensor consists of a monochromatic polarized light source, a glass prism coated with a thin layer of gold and a photodetector as shown in **Figure 1-5**. If the angle of the incident light on the base of the prism is larger than the critical angle, an evanescent field is formed and penetrates through the prism base onto the metal layer. This evanescent field can couple to the Surface Plasmon which is an electromagnetic wave at the metal-liquid interface at the specific angle, called the SPR angle. The SPR angle position is sensitive to changes in the refractive index of the thin layer adjacent to the metal surface that is sensed by the evanescent wave so that when sensing elements are immobilized onto the metal surface, an increase in the optical density occurs, resulting in a shift of the SPR angle to larger values [57].

SPR has been widely studied in the last two decades. Many commercial products are available now. However, the detection limit of SPR technology still needs to be improved to meet today's needs [58].

1.3.2 Electrochemical biosensors

Since the first enzyme electrode for the detection of glucose was developed in the 1960s, electrochemical biosensors have received considerable attention because of their capability of rapid on-line analysis and high sensitivity. An electrochemical biosensor is a device that converts a chemical reaction into electric potential or current during a biorecognition process. Based on the output signals of detection, the electrochemical biosensor can be classified into conductometric, potentiometric, and amperometric biosensors [59].

Conductometric biosensor: A conductometric biosensor is established based on the principle of conductivity change of medium due to generation of the products of an enzyme-catalysed reaction. For example, enzyme urease can catalyze urea to produce ammonium, bicarbonate, and hydroxide ions in the hydrolysis of urea as [60]

$$NH_2CONH_2 + 3H_2O \xrightarrow{urease} 2NH_4^+ + HCO_3^- + OH^- \qquad (1\text{-}1)$$

To form a biosensor, the enzyme is usually immobilized on an electrode surface that is specific to the target analyte and produces the products with different conductance of the enzyme layer. This change in conductivity can be measured by ion conductometric devices using interdigitated microelectrodes. However, conductometric biosensors are rarely used due to low specificity and a poor signal/noise ratio [59].

Potentiometric biosensor: for a potentiometric biosensor, the target analyte is detected by converting the biorecognition process into a potential signal. Biological active material such as enzymes and antibodies are immobilized on a surface of a transducer as ion-selective electrodes (ISE), and they generate a potential difference at the membrane/solution interface which is a logarithm proportional to the population of the

target medium.

The response of an ISE to an ion, i with activity a_i and charge z, can be expressed by the Nickolski - Eisenman Equation [61]

$$E = C + \frac{2.303RT}{z_i F} \log\left[a_i + k_{ij} (a_j)^{z_i / z_j} \right] \qquad (1\text{-}2)$$

where E is the measured potential, C is a constant, R is the gas constant, T is the absolute temperature, F is the Faraday constant, k_{ij} is the selectivity coefficient, a_i and a_j are the activity of major and interfering ion, i and j, and z_i and z_j are the charge of ion i and j, respectively.

Because ISE is the simplest platform of a potentiometric biosensor, today, transistors as electric signal amplifiers are usually coupled to ISE, and are called ion-sensitive field effect transistors (ISFET). In an ISFET biosensor, the amount of the current flow is related to the charges of biomolecule interaction, pH, different ions, and products of enzyme reactions, etc [62].

Amperometric biosensor: For an amperometric biosensor, the target analyte is detected by applying a constant potential and monitoring the current associated with the reduction or oxidation of an electroactive species. An amperometric biosensor typically consists of three electrodes: reference, auxiliary and working electrodes. Enzymes are usually immobilized on the working electrode as the biorecognition elements. When voltage is applied between the reference and the working electrodes, current flows between the working and the auxiliary electrodes due to the oxidation/reduction reaction of the target analytes. This current change is proportional to the amount of electro-oxidized/reduced analytes, which is proportional to the analyte population [63]. The working principle of

an amperometric biosensor can be expressed by the Cottrell Equation

$$I = \frac{1}{2} zFAC_o\left[\frac{D}{(\pi t)}\right] \quad (1\text{-}3)$$

where I is the current to be measured, z is the number of electrons transferred, F is the Faraday constant, A is the area of electrode, C_o is the population of the target analyte, D is the diffusion constant, and t is the time elapsed since the potential was applied.

Several commercial amperometric biosensors have been developed such as the well-known glucose biosensors SIRE P201 (Chemel AB, Lund, Sweden), and GlucoWatch Biographer (Cygnus, Redwood City, CA, USA).

1.3.3 Acoustic wave (AW) biosensors

When an AW device is used as a transducer, its resonance frequency, which changes with a mass loading on the device surface, is usually used as measuring signal. Based on that principle, an AW biosensor is established by immobilizing a layer of a sensing element on its surface to react with the target species [64, 65]. The reaction usually results in a mass load on the device. Therefore, the presence of target species can be detected by monitoring the shift in device's resonance frequency due to the mass change as shown in **Figure 1-6**. The capability of an AW device is usually characterized by two critical parameters: mass sensitivity (S_m) and quality merit factor (Q value).

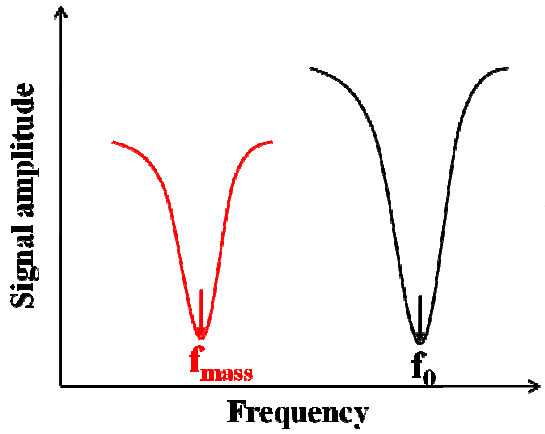

Figure 1-6. Scheme of frequency vs. signal amplitude of an AW sensor, where f_0 and f_{mass} are the resonance frequency of the sensor without mass load and with mass load, respectively.

Mass sensitivity (S_m) is defined as the shift in resonance frequency due to a unit mass load as [66]

$$S_m = \frac{\Delta f_0}{\Delta m} \qquad (n = 1, 2, 3, \ldots) \qquad (1\text{-}4)$$

where Δf_0 is the shift in the resonance frequency due to the attachment of a mass load (Δm).

The Q value describes the sharpness of the resonance peak and can be expressed as [67]

$$Q = \frac{f_0}{\Delta f} \qquad (1\text{-}5)$$

where f_0 is the resonance frequency and Δf is the width of the resonance peak at its half peak height as shown in **Figure 1-7**.

A higher Q value means a sharper resonance peak which would give a higher accuracy in determining resonance frequency and a smaller minimum detectable frequency change. Therefore, for the development of high-performance sensors, AW devices with a high S_m and a high Q value are highly desirable.

Based on the propagation of acoustic waves, AW devices are classified as: thickness

shear mode (TSM) devices, surface acoustic wave (SAW) devices, acoustic wave plate mode (APM) devices, and flexural plate wave (FPW) devices. Recently, MEMS based AW devices have attracted a great deal of attention due to their high mass sensitivity (S_m).

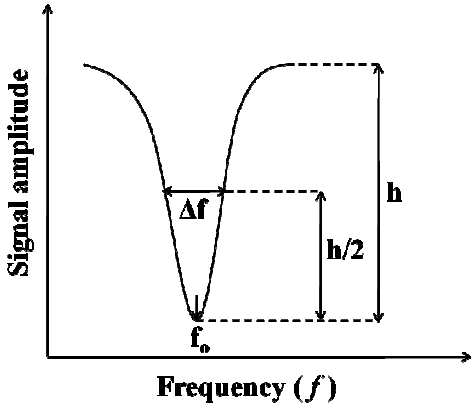

Figure 1-7. Schematic definition of Q value. The resonance peak is at frequency f_0 with a height of h.

Thickness shear microbalance (TSM): TSM devices, also known as quartz crystal microbalance (QCM), are widely used commercial products. A TSM device consists of a piezoelectric substrate, usually a thin disk of single crystal AT-cut quartz (a disk cut from a quartz mineral at a 35.25^o orientation to its optical axis), with metal electrodes deposited on each side of the disk. Due to the piezoelectric properties and crystalline orientation of the quartz, application of a voltage to the electrodes will cause a shear deformation of the crystal and thereby generate acoustic waves propagating through the crystal [68]. At the crystal surfaces, the displacement is maximized which makes the device sensitive to surface interactions [69]. A change in resonance frequency due to a mass loading can be expressed by the Sauerbrey Equation [70]

$$\Delta f_o = -\frac{2}{\sqrt{E\rho}} f_o^2 \frac{\Delta M}{A} \qquad (1\text{-}6)$$

where f_0 is the fundamental resonance frequency, E is Young's modulus, ρ is the density of the crystal material, ΔM is the change in mass, and A is the area. When operated in air,

the *Q* value of a QCM can be as high as 10^6. The high sensitivity and high *Q* value obtained in the QCM make the QCM a great device for the measurement of mass. For example, a surface density as small as 0.1 μg/cm^2 can be measured using a QCM. However, in order for the QCM to work properly, the size of the electrode area has to be relatively big. This makes it difficult for the QCM to be used to measure a small mass. For example, for a QCM with an electrode of about 0.6 cm^2, the minimal mass that can be measured using the QCM mentioned above is about 60 ng.

Surface acoustic wave (SAW) device: A SAW device consists of two interdigital transducers (IDTs) that are usually lithographically deposited on two ends of the surface of a piezoelectric crystal plate as shown in **Figure 1-8**. When an alternating electric field is imposed on the input transducer, a periodic strain field is generated in the piezoelectric crystal that produces a SAW known as a Rayleigh wave in which the energy is confined on the surface of the crystal [72]. The excited AW associated with a wave potential, φ is then received by the output transducer on the other end and converted back to electric signal [73]. When operated in air, the *Q* value of a SAW device can exceed 10^4.

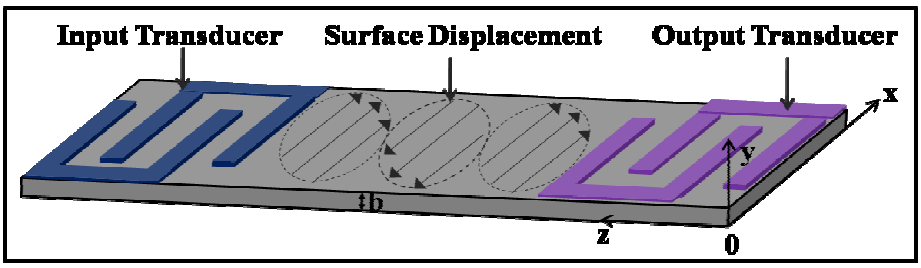

Figure 1-8. Schematic illustration of an Acoustic Plate Mode (APM) device [71].

Any surface perturbation such as a mass loading on the device surface will affect the wave propagation characteristics such as wave velocity and attenuation due to the interactions between the SAW and the surface layer. Therefore, the SAW biosensor can

be established based on the principle. However, in a fluid environment, the presence of surface-normal displacement components may generate waves in the adjacent fluid causing part of the acoustic energy to go into the fluid and resulting in severe attenuation making the SAW is a poor candidate for fluid-based biosensors.

Acoustic wave plate (APM) device: An APM device is very similar with the SAW device but the IDT design and substrate parameters such as the periodicity of the electrodes within the IDTs, the thickness of the plate, and the frequency of the applied electrical signal are different. The APM displacements may be either along the propagation direction (longitudinal APM) or perpendicular to the direction of propagation (shear-horizontal (SH-APM)); the latter is mostly used. Both ST cut and AT cut thin single-crystalline quartz plates can be used in SH-APMs devices as acoustic waveguides while the latter has better temperature stability without allowing excitation of the SAW.

A mass loading on the surface causes a decrease in propagation velocity which is expressed as [71]

$$\frac{\Delta v}{v_o} = -\frac{J_n \rho_s}{b \rho_q} \tag{1-7}$$

where v_o is the surface particle velocity, $J_0 = 1/2$, and $J_n = 1$ for $n \geq 1$, b is the thickness of the plate, and ρ_s is the surface mass density of mass load.

Assuming the quartz plate is an isotropic medium, the resonance frequency for the n^{th} order mode is expressed as [71]

$$f_n = \frac{v_o}{d}\left[1+\left(\frac{nd}{2b}\right)^2\right]^{1/2} \tag{1-8}$$

where v_0 is the surface particle velocity, n is the transverse mode (n = 0, 1, 2, …), d is the

periodicity, and *b* is the thickness of the plate.

Because both faces of the crystal undergo displacement, the detection can occur on the opposite surface of the IDTs and therefore eliminate any potential interactions between the biochemical solution and the IDTs. In addition, absence of surface-normal components of displacement allows the acoustic waves to propagate in contact with a liquid without losing excessive amounts of acoustic energy into the liquid making it a good candidate in biosensing applications.

Flexural plate wave (FPW) device: In an FPW device, acoustic waves known as Lamb waves are excited in a thin elastic plate whose thickness is less than one acoustic wavelength. A Lamb wave can be considered as superimposition of two Rayleigh waves on the two opposite side of the plate. There are two modes of Lamb waves: symmetric and antisymmetric modes as shown in **Figure 1-9**.

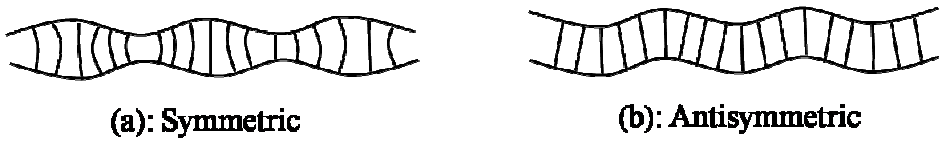

Figure 1-9. Diagram of Lamb wave modes [73].

For symmetric modes, displacements are symmetric about the neutral plane of the plate, and antisymmetric waves are those whose displacements are odd symmetric about the neutral plane of the plate. Which mode dominates depends on the thickness of the plate [71].

Similar to other acoustic wave devices, a mass load on the device surface will cause the change in phase velocity v_p. The phase velocity of an FPW is lower than that of most liquids. When the FPW device contacts or immerses in the liquid, a slow mode of propagation exists in which there is no radiation from the plate. Therefore, the FPW can

work well since most biosensing measurements are done in a liquid environment. The comparison of specifications of the four acoustic wave sensors is listed in **Table 1-4**.

Even though some of these AW devices are widely used in current commercial products, S_m is limited by the size of the AW device. Based on the principles of these devices, one can find that an AW device with a small size would have a high S_m. Therefore, MEMS-based AW devices have been extensively investigated for the development of high-performance AW devices due to the fact that these devices are small and exhibit ultra-high sensitivity.

Table 1-4. Comparison of different AW sensors [71, 74].

Sensor type	TSM	SAW	APM	FPW
Sensitivity	Low	High	Low-Medium	High
Factors Determining Sensitivity	Plate Thickness	IDT Finger Spacing	Plate Thickness, IDT Finger Spacing	Plate Thickness
Motion at Device Surface	Transverse	Normal and Transverse	Transverse	Normal and Transverse
Immersible?	Yes	No	Yes	Yes
Operating Frequency	Low (5-30MHz)	High (30-500MHz)	Medium-High (25-200MHz)	Low (1-10MHz)
Mechanical Strength	Med	High	Med	Low

1.3.4 Micro-cantilever (MC) based biosensors

Besides the high S_m, the MC based sensors have many other advantages, such as ease of integration with an analysis circuit [75, 76]. A typical MC consists of a long and thin micro-beam fixed at one end with support. An AW can be operated using two different principles: dynamic mode and static mode [77].

In dynamic mode, MCs work as resonators. The resonance frequency of the cantilever is used as the measurement signal. The working principle of a dynamic MC is

exactly the same as other AW devices. That is, it is based on the change in the resonance frequency of the MC due to the attachment of a mass load on the surface or stress induced by the interaction between the sensing element and the target of interest. In static mode, the deflection or the displacement of the free end of an MC is used as the measurement signal [78]. Surface stress caused by the binding of target biological molecules on one side of a cantilever or a mass load on the surface of an MC would result in a deflection of the free end [79, 80]. That is, the MC is actually used as a force sensor. Therefore, the direction of the force or the orientation of the MC is important.

Both dynamic and static modes have been extensively studied and widely investigated for bio/chemical detection. However, the dynamic mode exhibits some critical advantages over the static mode. For example, the performance of static mode MC is strongly dependent on the orientation of the cantilever beam while dynamic mode MC is independent of it. In a medium, MCs would undergo a slight vibration caused by the mechanical thermal noise (so-called Brownian motion) that affects a static mode MC's performance [81] while an MC in dynamic mode will be barely affected since it is excited at the resonance frequency. In addition, only one surface can be used for static mode while both surfaces can be used for dynamic mode for biosensors.

For a dynamic MC, the resonance frequency of its bending oscillation is [82]

$$f_n = \frac{\lambda_n^2}{2\pi\sqrt{12}}\frac{t}{L^2}v \qquad (n = 0, 1, 2 \ldots) \qquad (1\text{-}9)$$

where λ_n is the nth mode eigenvalue, L is the length of cantilever beam, t is the thickness of the beam, and v is the acoustic velocity which is dependent on the density and the elastic properties of the cantilever beam.

To form a biosensor, the surfaces of a cantilever need to be immobilized with a

layer of sensing element. When an MC immobilized with a sensing element on its surface is exposed in the analyte, the reaction between the sensing element and target species results in a mass load on the surface, which causes a change in the resonance frequency. If a small mass (Δm) is uniformly loaded on the MC surface, the resonance frequency shift (Δf) can be expressed as [83]

$$\Delta f = -\frac{f_0}{2}\frac{\Delta m}{M} \tag{1-10}$$

where f_0 and M are the resonance frequency and mass of the MC without the mass load, respectively. Based on Equation (1-10), one can find that the S_m of an MC increases with reduction of the mass of the MC and/or an increasing resonance frequency. As indicated by Equation (1-9), the resonance frequency increases with reducing size. Combining Equations (1-9) and (1-10), one can find that the S_m increases with reducing size and that the S_m is the properties of the beam materials. It has been demonstrated that an MC sensor can detect a mass as small as ~10^{-18} g when the MC is operated in vacuum.

Based on the driving/sensing mechanism, dynamic MCs can be further divided into three types in terms of the driving/sensing mechanism: silicon-based MCs, piezoelectric MCs, and magnetostrictive MCs.

Silicon-based MCs: The silicon-based cantilevers are driven using a mechanical force/impact. They are typically made of silicon/silicon nitride, with dimensions usually ranging from nano to micro scales and these MCs can be easily fabricated. Usually, an external piezoelectric material is mounted near the cantilever, and the MC is actuated by mechanically shaking as an alternating electric field is applied on the driving piezoelectric material [76]. The vibration of the MC is usually detected using optical methods. In this method, the displacement of the free end of the cantilever is measured

using the optical deflection of an incident laser beam on a position-sensitive photodetector, which allows the absolute value of the cantilever displacement to be calculated as shown in **Figure 1-10**.

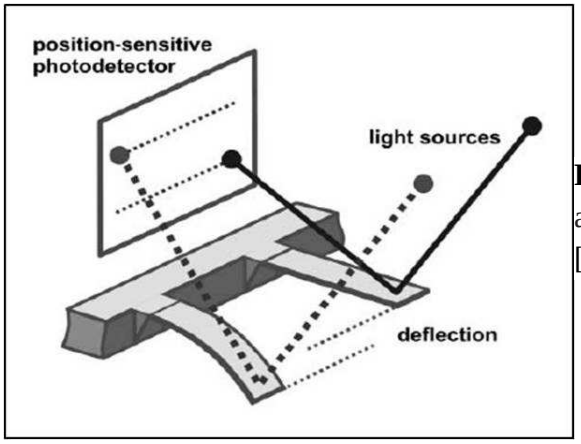

Figure 1-10. Illustration of cantilever array readout by optical beam deflection [76].

This method is very sensitive with a sub-angstrom resolution and can be implemented easily. However, there are some drawbacks: the optical measurement equipment is bulky, and the measurement is time-consuming due to the need for a continuous alignment. The in-situ detection is limited due to the transparecy of the sample. In addition, due to the dispersion of the laser beam in the medium, it is a challenge to do the measurement when the sensor is in liquid [76].

Piezoelectric cantilevers: The piezoelectric cantilevers are made of piezoelectric materials and work based on the piezoelectric effect: when an electric field is applied on the materials, a mechanical deformation (shrink or expand) occurs. It is usually a multi-layered structure that contains a piezoelectric layer such as PZT and several non-piezoelectric layers, such as piezo-resistive layers [84].

Compared with silicon-based cantilevers, piezoelectric cantilevers are much easier to actuate and sense due to the piezoelectric effect. When there is an alternating current

(AC) electric field along the thickness of the piezoelectric material, the piezoelectric beam will oscillate. The resonance frequency of the piezoelectric cantilever can be simply determined by an impedance analyzer. That is, the impedance changes with frequency and a maximum change occurs at the resonance frequency. However, due to the requirement of the electric/signal wire connection and also the damping issue, it is a challenge to detect the targets in conductive/viscous liquids.

In general, MCs in viscous media exhibit a low *Q* value. For example, although the *Q* value can be as high as 10^4 when the MC is operated in a vacuum, the *Q* value of MCs in the air is more likely hundreds, and it is rare to obtain a *Q* value of more than 10 for the MCs operated in liquid [83]. Therefore, a great deal of effort has been devoted to research designed to improve the *Q* value of the MCs. Different approaches have been investigated. **Figure 1-11** presents a new approach to improve the *Q* value of MCs [85]. Here, to obtain a *Q* value, the MC was operated in vacuum. To conduct the measurement in a liquid analyte, microfluidic channels were built in the MC beam.

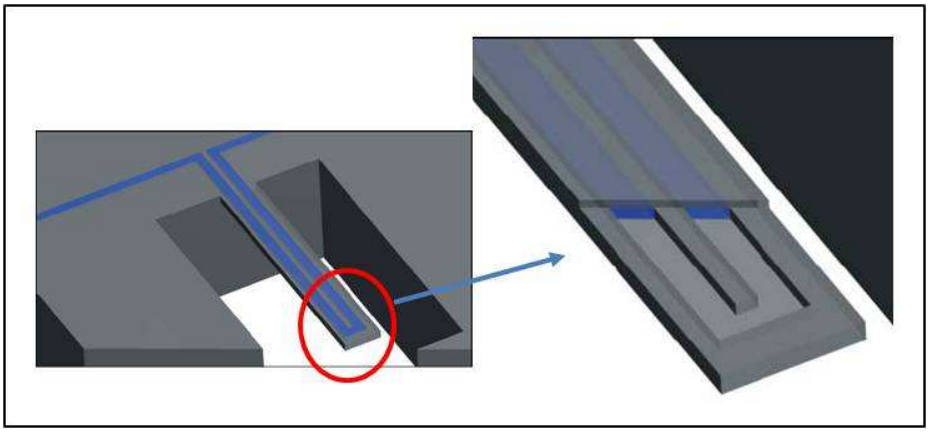

Figure 1-11. Illustration of a fluid filled micro-cantilever [85].

It is well known that the damping effect is not only dependent on the acoustic mode but also on the materials. Therefore, MCs made of different materials have been

investigated. For example, magnetostrictive MCs (MSMCs) have been recently introduced and it is found that the MSMC in the liquid, such as water, can exhibit a *Q* value as high as 30 [83].

1.3.5 Magnetostrictive micro-cantilever (MSMC)-based biosensors

The advantages of the MSMCs originate from the materials properties of magnetostrictive materials and their magnetic nature. A magnetostrictive material is a material whose shape/dimension changes with an applied magnetic field. An MSMC consists of two layers: one is made of a magnetostrictive material and the other is made of a non-magnetostrictive material as shown in **Figure 1-12**. Therefore, if an ac magnetic field is applied onto an MSMC, a bending vibration will be introduced due to the magnetostriction of the magnetostrictive (active) layer [86, 87].

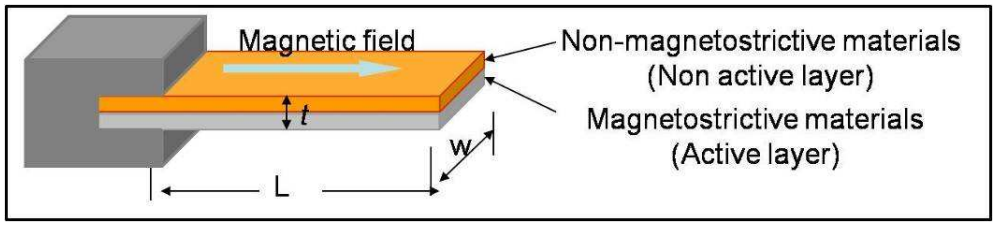

Figure 1-12. Configuration of a magnetostrictive micro-cantilever [88].

Besides the high *Q* value, the MSMCs exhibit the following advantages over others: they are wireless, cost efficient, and are easily employed in different environments [86-90]. The MSMCs have been used for in-situ detection of bacterial/spores in water, such as such as *S. typhimurium* [88], *E. coli* [91], and *B. anthracis spores* [92].

1.4 Magnetostrictive particle (MSP) based biosensors

Besides the MSMCs, the magnetostrictive materials have been used to build other types of acoustic resonators, which have been used as a sensor platform for the development of high-performance physical, chemical, and biological sensors [93-97].

One of these resonators is the magnetostrictive particle (MSP) which is a truly freestanding resonator. An MSP is a piece of rectangle-shaped magnetostrictive material that has a length much bigger than its width and thickness. Compared with the MSMCs, MSPs exhibit a much higher *Q* value and a better sensitivity. For example, the *Q* value of an MSP in air is about 1000, while it is about 100 in water. For a strip-like MSP, the mass sensitivity is about 10 times better than that of an MC with the same size [83].

1.4.1 Resonance behavior of MSP

In the design, longitudinal oscillation (i.e. the oscillation along the length direction) of the MSP is used. The nth harmonic resonance frequency (f_n) of the longitudinal oscillation is [99]

$$f_n = \frac{n}{2l}\nu \qquad \text{(n=1, 2, 3…)} \qquad \text{(1-11)}$$

where l is the length of the MSP, and ν is the acoustic velocity of the magnetostrictive material and is treated so far as a constant. The acoustic velocity is dependent on the elastic properties, such as Young's modulus (E) and the Poisson's ratio, and the density (ρ) of the material as

$$\nu = \sqrt{\frac{E}{\rho\left(1-\sigma^m\right)}} \qquad (m = 1 \text{ or } 2) \qquad \text{(1-12)}$$

The value of m is reported to be either one or two, depending on the geometry of the MSP, in the literature [98, 99].

To be developed as a biosensor, an MSP is usually immobilized with a layer of sensing element on its surface. The reaction between the sensing element and the target species usually causes a change in the properties of the recognition layer, such as the mass and elasticity. This change results in a change in the resonance frequency. Therefore,

the presence of target species can be detected by monitoring the shift in the device's resonance frequency due to mass loading caused by the attachment of bacteria cells on the sensor surface as shown in **Figure 1-13**.

An MSP is actuated using a magnetic field to the oscillation due to the magnetostrictive effect. The oscillation of the MSP is monitored based on the change in the magnetic field around the MSP. Therefore, the resonance behavior of an MSP can be characterized using magnetic field/signal. That is, the biosensors based on MSP are wireless, which is the principal advantage of the MSP over other sensors.

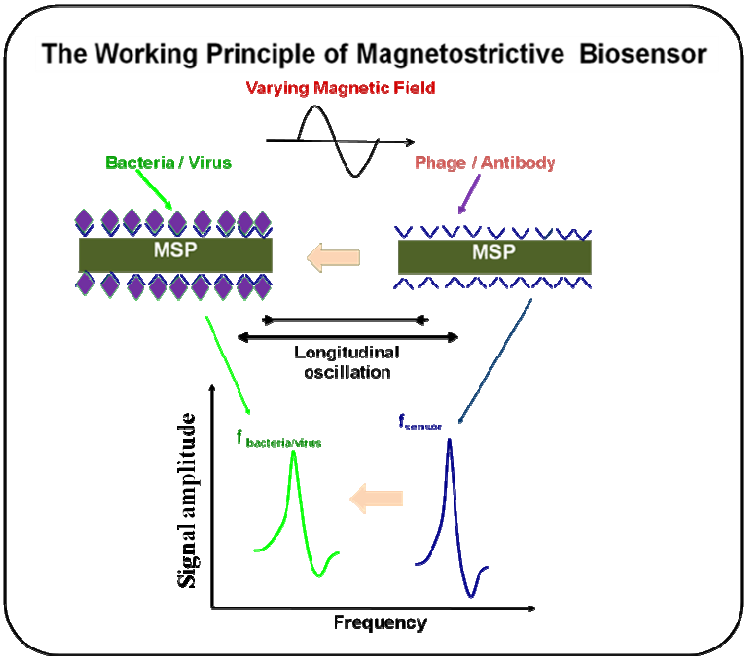

Figure 1-13. Schematic of working principle of a magnetostrictive biosensor.

The theoretical sensitivity S_m of an MSP sensor with a uniform mass load Δm is [83]

$$S_m = -\frac{\Delta f}{\Delta m} \cong \frac{f_n}{2M} \qquad (1\text{-}13)$$

where M is the mass of the MSP sensor without mass load and f_n is the nth (n = 1, 2, 3…) order harmonic resonance. It has been clearly found that as the MSP size decreases, the sensitivity increases. Therefore, it is of great interest to develop biosensors using small-

sized MSPs.

1.4.2 Resonance behavior of MSP in viscous media

It is well known that an acoustic resonator experiences a damping effect when it is operated in a viscous media. The damping effect makes the resonance frequency and the *Q* value of the resonator lower. The damping effect is dependent on the physical properties of the media, such as density and viscosity. If the surface of the MSP is ideally smooth and there is only the friction force due to the viscosity of the media, the change in the resonance frequency of an MSP can be expressed as [100]

$$\Delta f = f_{n,l} - f_n = -\frac{\sqrt{\pi f_n}}{2\pi\rho d}(\eta\rho_l)^{1/2} \qquad (1\text{-}14)$$

where f_n is the intrinsic resonance frequency of the nth mode as described by Equation (1-11), $f_{n,l}$ is the nth resonance frequency of the MSP in viscous media, η is the viscosity and ρ_l is the density of the media, ρ is the density of the MSP, and d is the thickness of the MSP. This Equation is obtained based on the following assumptions: 1) the viscosity is small and the media is treated as a Newtonian liquid; 2) the surface displacement of an MSP is independent of the location which is certainly is not the case; and 3) the edge effect is ignored.

Regarding the influence of the media on the *Q* value of an acoustic resonator, it is well known that

$$\frac{1}{Q_{n,l}} = \frac{1}{Q_n} + \frac{1}{Q_l} \qquad (1\text{-}15)$$

where $Q_{n,l}$ is the *Q* value of the resonator in viscous media and the Q_n is the intrinsic *Q* value of the resonator, which is dependent on the elastic loss of materials, and Q_l is the *Q*

value contributed by the media or the effect of media. By using the assumptions used for Equation (1-15), it was obtained that [100,101]

$$\frac{1}{Q_{n,l}} = \frac{1}{Q_n} + \frac{1}{\rho d\sqrt{\pi f_n}}(\eta\rho_l)^{1/2} \qquad (1\text{-}16)$$

When the surface of an MSP is not ideally smooth, another force acts on the MSP. That is the media trapped on the surface of the MSP as shown in **Figure 1-14**. That is, the influence of the surface roughness on the resonance behavior can be treated as a thin layer (thickness of R_{ave}) of the media rigidly attached on the surface as a mass load. Based on this, there is a change in the resonance frequency due to the surface roughness. This change can be expressed as [100]

$$\Delta f_n = -f_n \frac{\rho_l R_{ave}}{\rho d} \qquad (1\text{-}17)$$

That is, the reduction in the resonance frequency due to the surface roughness is related to the density of the media. If both surface roughness and the damping effect are accounted for, the total change in the resonance frequency of an MSP would be

$$\Delta f_n = -\frac{\sqrt{\pi f_n}}{2\pi\rho d}(\eta\rho_l)^{1/2} - f_n \frac{\rho_l R_{ave}}{\rho d} \qquad (1\text{-}18)$$

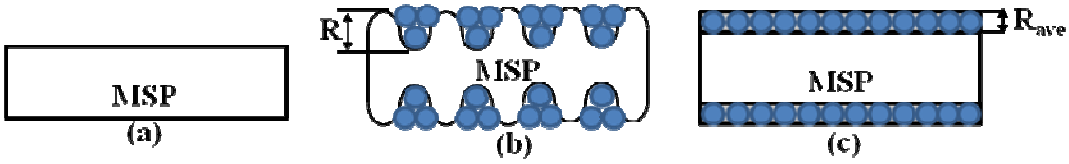

Figure 1-14. (a) Smooth surface; (b) Rough surface with trapped liquid particles; (c) Equivalent attached liquid layer on the smooth surface. The blue solid circles represent liquid particles. R denotes the variation of the mountains and valleys where the mountains and valleys were assumed to be evenly and uniformly distributed on the MSP surface. R_{ave} denotes the average surface roughness (i.e. average thickness of the trapped liquid layer) [102].

1.4.3 Magnetostrictive effect and materials

As shown in **Figure 1-15**, where the mechanical strain response of the material as the function of the magnetic field applied on the material is given, the magnetostrictive effect, the mechanical strain ~ magnetic field, is not a linear effect [103]. Actually, the λ~H relationship is more like a quadratic function with a saturated value. Therefore, when there is only a pure alternating current (ac) magnetic field applied, the strain response of the material to *H* is of a frequency doubling the frequency of the applied ac field. However, if a direct current (dc) bias is imposed on the ac magnetic field, the strain response has a constant strain and ac strain components. The ac strain response has the same frequency as the ac magnetic field and the strain response is proportional to the ac driving field. If the strength of the ac magnetic field is fixed and the strength of the dc field changes, as shown in **Figure 1-15**, the amplitude of the ac strain changes. There is a dc field at which the ac strain has the largest amplitude.

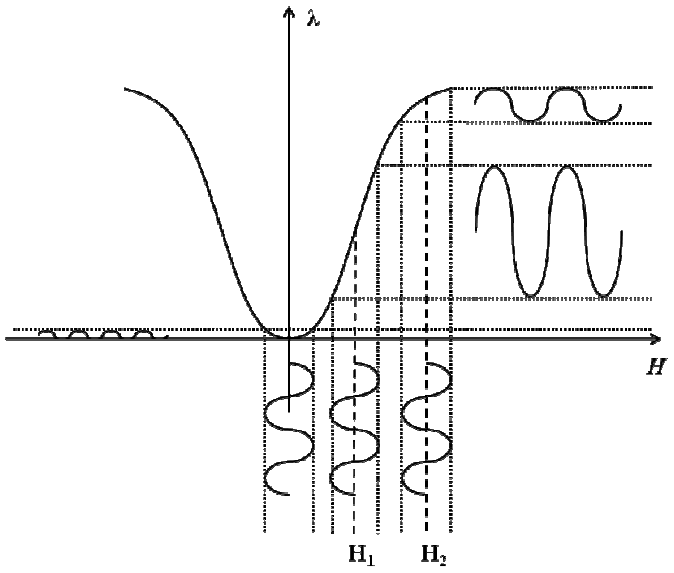

Figure 1-15. Magnetostriction response of a magnetostrictive material: Mechanical strain (λ) in relation to external magnetic field (H) [103].

There are many available magnetostrictive materials with different magnetostriction coefficients and other materials properties. Because ofthe sensor requirements for the development of AW sensors which are a higher S_m and a higher Q, the most currently used magnetostrictive materials in the development of biosensors based on MSP is a commercially available alloy, Metglas^{TM} 2826MB ($Fe_{40}Ni_{40}P_{14}B_6$). This material is cast by a liquid-quenching technique. That is, the melt alloy is solidified onto a fast rotating cooled wheel with a minimum cooling rate of 10^6 degree/s [104]. By employing this technique, amorphous alloy ribbons, typically with a width of 10 ~ 100 mm and a thickness of 20 ~ 30 μm, are produced [104].

Some general information about the material properties of Metglas ^{TM} 2826 are listed in **Table 1-5**.

Table 1-5. Material properties for Metglas™ 2826 [105, 106] and $Fe_{80}B_{20}$ [82,107,108].

Property	**Metglas™ 2826**	**$Fe_{80}B_{20}$**
Density (10^3 kg/m^3)	7.9	7.39
Young's modulus (GPa)	100-110	166
Crystallization temperature (^{o}C)	448	448
Saturated magnetostrictive strain, λ_s (10^{-6})	12	31
Electric resistivity (μΩ·m)	1.38	1.5
Poisson ratio	0.33	0.3
Magnetoelastic coupling coefficient	0.98	N.A.

In recent years, another type of amorphous MSP made of $Fe_{80}B_{20}$ has also been studied for the development of biosensor platforms [107]. This material can be easily fabricated using a microelectronic process and an electrochemical method. Therefore, it is easy to fabricate the MSPs in a smaller size using this alloy. For example, the MSP in size of 50 μm × 6 μm × 3 μm has been fabricated using this alloy [109]. Magnetostrictive nanowires have also been prepared using this alloy [108]. Some general information about the properties of bulk $Fe_{80}B_{20}$ is listed in **Table 1-5**.

1.4.4 Current status of biosensors based on MSPs

Due to the high performance obtained in MSP, a great deal of research has been done on the development of MSP biosensors. To date, MSP biosensors using phages as sensing elements have been successfully developed for the detection of pathogens, such as *S. typhimurium* [94], and *B. anthracis* [96]. The detection limits range from 10^3 cfu/ml to 10^5 cfu/ml depending on the size of the sensor. A can be seen in **Table 1-2**, these detection limits do not meet the current needs. Therefore, it is of interest to have MSPs in smaller sizes to develop sensors with a better sensitivity or detection limit. Therefore, much research is focused on minimizing the sensor size in order to increase the sensitivity of the MSP sensors. As for the sensing element, most of current MSP biosensors utilize phage due to the fact that phage can be easily immobilized onto the

surfaces of MSPs.

1.5 Sensing element for biosensors – antibodies vs. phages

Filamentous bacteriophages (phages in short) have been considered to have a great potential as antibody substitutes due to their robust structures, resistant to heat and many organic solvents such as urea, acid, and alkali [110]. A phage is a virus that infects bacteria. It consists of five types of proteins: pVIII, pVII, pIII, pVI, and pIX as shown in **Figure 1-16**. The phage consists mainly of a tube-like filament that is composed of 2700 copies of proteins, pVIII covalently linked with a circular single-stranded DNA (ss-DNA) genome. The so-called coat proteins pVII and pIX are at one end where assembly initiates, while proteins pIII and pVI are at the other end of the filament where assembly terminates. A typical filamentous bacteriophage is about 6 to 7 nm in diameter and 800 to 900 nm in length depending on the strain [113].

Purified phages can be stored at moderate temperatures for very long time without losing their probe-binding activity [114]. Phages can be reproduced and cloned simply by infecting the phages into fresh bacterial host cells and can be selected for binding to a particular target antigen. However, phage selections on some proteins and especially on peptides are not always successful due to immobilization-associated features and so far only limited affinity selected phages have been developed.

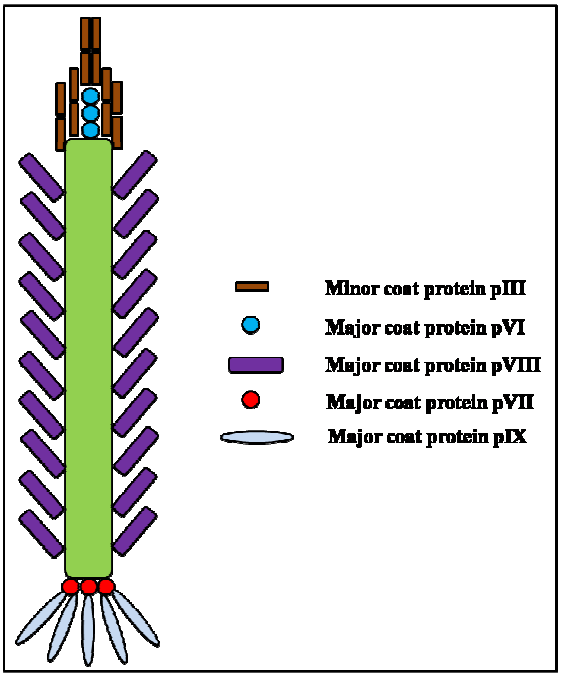

Figure 1-16. Schematic structure of a filamentous phage [111, 112].

Antibodies, also known as immunoglobulins, have been proven to be extremely adaptable and effective biomaterials in various biomedical and technical applications [115]. They are composed of heavy chains and light chains, linked by disulphide bonds. Each heavy chain has two regions: a constant region that is the same for all antibodies in the same class but differs between each class of antibodies and a variable region that is the same for all antibodies produced by the same immune cell but differs between different immune cells [116]. Depending on the difference of heavy chain constant region, antibodies can be divided into five main classes: IgG, IgA, IgM, IgD, and IgE and a typical structure of antibody IgG is shown in **Figure 1-17**.

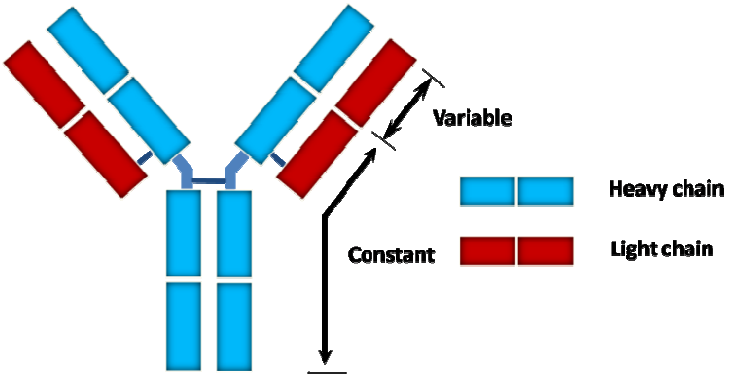

Figure 1-17. Configuration of a typical antibody structure [116].

Antibodies can also be classified into polycolonal antibodies (PAbs) and monoclonal antibodies (MAbs) based on the production process. MAbs are produced from the same type of immune cells and are all clones of a single parent cell while PAbs come from different immune cells so that PAbs are less specific since they recognize all antigens to which the animal has been exposed [117]. Therefore, to be developed as a sensing element, PAbs should be affinity purified which greatly increases the cost. In contrast, MAbs are more specific since they can only recognize and bind a single epitope of target bacteria [118].

In conclusion, phages have higher stability and are easier to immobilize. However, the commercial availability of phage is limited which limits their use in biosensor applications. On the other hand, even though antibodies are difficult to be immobilized, they are more specific and are technically mature in production and have been developed to identify almost any pathogen. Therefore, in order to develop the MSP technology for the detection of a wide variety of pathogens, it is highly desirable to explore antibody-based MSP biosensors.

1.6 Research objectives

Based on above discussion, the following objectives have been designed for this

study in order to fully develop the MSP technology for the detection of pathogens:

1) Develop antibody immobilized MSP biosensors: the successful development of antibody-based MSP biosensors would enable MSP technology to be used for the detection of a wide variety of pathogens.

2) Create an MSP with a smaller size: in order to fabricate MSP biosensors with a higher sensitivity, the MSPs need to be a smaller size. However, it is difficult to fabricate the MSPs with a very small size using the commercially available Metglas. Therefore, an electrochemical method is used to prepare other magnetostrictive materials.

3) Characterize the resonance behavior of the MSP: the performance of an MSP sensor is dependent on its resonance behavior. For most biological detection, it would be advantageous to characterize the sensor performance in the analyte which is usually a liquid. In this study, the resonance behavior of the MSPs with different geometry was systemically investigated.

4) Build a handheld interrogation device: the MSP technology provides an opportunity for the development of inexpensive and rapid response biosensors for in-situ and in-field detection. To fully use this advantage, the interrogation system/unit of MSP resonance has to be small, inexpensive, and easy to operate. Therefore, the development of a handheld device for the interrogation of the MSP is explored. Both frequency-domain and time-domain technologies are studied.

References:

1. "http://www.fda.gov/Food/FoodSafety/RetailFoodProtection/FoodCode/FoodCode2001/ucm089078.htm."

2. P.S. Mead, L. Slutsker, V. Dietz, L.F. McCaig, J.S. Bresee, C. Shapiro, P.M. Griffin, R.V. Tauxe, Food-Related Illness and Death in the United States, Emerging Infectious Diseases 5 (1999) 607-625.
3. E.O. Michael, I.M. Samuel, SALMONELLA: A Model for Bacterial Pathogenesis. Annual Review of Medicine 52 (2001) 259-274.
4. "http://www.cdc.gov/salmonella/saintpaul/faq.html."
5. N. Swanger, D.G. Rutherford, Hospitality Management Food-borne illness: the riskenvironment for chain restaurants in the United States 23 (2004) 71–85.
6. "http://www.cdc.gov/salmonella/typhimurium/update.html."
7. D.C. Rodrigue, R.V. Tauxe, B. Rowe, International increase in *Salmonella enteritidis*: A new pandemic? , Epidemiology and Infection 105 (1990) 21–27.
8. M. O'Mahony, J. Cowden, B. Smyth, D. Lynch, M. Hall, B. Rowe, E.L. Teare, R.E. Tettmar, A.M. Coles, R.J. Gilbert, E., Kingcott, C.L.R. Bartlett, An outbreak of *Salmonella* saintpaul infection associated with bean sprouts, Epidemiology and Infection 104 (1990) 229–235.
9. H.C. Berg, *E. coli* in motion (Biological and Medical Physics, Biomedical Engineering), Springer, 2003.
10. J. P. Nataro, J. B. Kaper, Diarrheagenic Escherichia coli, Clinical Microbiology Reviews 11 (1998) 403-403.
11. F. Villani, F. Russo, G. Blaiotta, G. Moschetti, D. Ercolini, Presence and characterization of verotoxin producing *E. coli* in fresh Italian pork sausages, and preparation and use of an antibioticresistant strain for challenge studies, Meat Science 70 (2005) 181–188.

12. Institute of Medicine, Escherichia coli O157:H7 in ground beef: review of a draft risk assessment, National Academies, 2002.
13. “http://www.foodpoisonjournal.com/2010/07/articles/foodborne-illness outbreaks/bison-meat-recall-due-to-e-coli-o157h7-product-list-from-the-source/”
14. S.S. Deshpande, Handbook of Food Toxicology (Food Science and Technology), CRC, 2002.
15. A. Ogston, Classics in Infectious Diseases: “On Abscesses”, Reviews of Infectious Diseases 6 (1984) 122–28.
16. R.H. Deurenberg, E.E. Stobberingh, The evolution of *Staphylococcus aureus*, Infection Genetics Evolution 8 (2008) 747–763.
17. U.S. Food & Drug Administration Center for Food Safety & Applied Nutrition, Bad Bug Book: Foodborne Pathogenic Microorganisms and Natural Toxins Handbook, International Medical, 2004.
18. “http://wwwn.cdc.gov/food-borneoutbreaks/Default.aspx.”
19. E.G.D. Murray, R.A. Webb, M.B.R. Swann, A disease of rabbits characterized by a large mononuclear leukocytosis, caused by a hitherto undescribed bacillus Bacterium *monocytogenes*, Journal of pathology and bacteriology 29 (1926) 407-39.
20. J. Rocourt, P. Cossart, *Listeria monocytogenes*, in "Food microbiology -- fundamentals and frontiers", ASM, 1997.
21. J. McLauchlin, D. Jones, *Erysipelothrix* and *Listeria* In: Borriello, S.P., Duerden, B.I. (Eds.), Topley and Wilson’s Microbiology and Microbial Infections, Systematic Bacteriology, CDRom, 1999.

22. M.J. Linnan, L. Mascola, X.D. Lou, V. Goulet, S. May, C. Salminen, D.W. Hird, M.L. Yonekura, P. Hayes, R. Weaver, A. Audurier, B.D. Plikaytis, S.L. Flannin, K.A. Broome, and C.V., N. Epidemic *listeriosis* associated with Mexican-style cheese, The New England Journal of Medicine 319 (1988) 823– 828.
23. J. McLauchlin, Epidemiology of *listeriosis* in Britain. Proceedings of the International Conference on *Listeria* and food safety (1991) 38– 47.
24. M.S. Mahmood, A.N. Ahmed, I. Hussain, Prevalence of *Listeria monocytogenes* in Poultry Meat, Poultry Meat Products and Other Related Inanimates at Faisalabad. Pakistan Journal of Nutrition 2 (2003) 346-349.
25. J.M. Farber, P.I. Peterkin, *Listeria monocytogenes*, a food-borne pathogen. Microbiological Reviews 55 (1991) 476–511.
26. J. Denny, J. McLauchlin, Human *Listeria monocytogenes* infections in Europe — an opportunity for improved European surveillance, Eurosurveillance (2008)13.
27. J.M. Farber, J.Z. Losos, *Listeria monocytogenes*: a food-borne pathogen, Canadian Medical Association Journal 138 (1988) 413-418.
28. J. Rocourt, J. Bille, Food-borne *listeriosis*, World Health Statistics Quarterly 50 (1997) 67-73.
29. Anonymous, Outbreak of *listeriosis*—northeastern United States, Morbidity and Mortality weekly report 51 (2002) 950–951.
30. J.D. Greig, A. Ravel, Analysis of food-borne outbreak data reported internationally for source attribution International, Journal of Food Microbiology 130 (2009) 77–87.
31. A.K. Bhunia, Foodborne microbial pathogens: mechanisms and pathogenesis, Springer, 2007.

32. *Staphylococcus aureus* Infection and Disease, A. Honeyman, H. Friedman, M. Bendinelli, Springer, 2010.
33. A.H. El-Shaarawi, W.W. Piegorsch, Encyclopedia of Environmetrics, Wiley, 2002.
34. P. Quinn, and M.E. Carter, Clinical Veterinary Microbiology, Mosby, 1993.
35. P. Downes, and K. Ito, Compendium of Methods for the Microbiological Examination of Foods by Frances, American Public Health Association, 2001.
36. N.S. Hobson, I. Tothill, A.P.F. Turner, Microbial detection, Biosensors & Bioelectronics 11 (1996) 455-477.
37. E. Engvall, P. Perlmann, Enzyme-linked immunosorbent assay (ELISA). Quantitative assay of immunoglobulin G. Immunochemistry 8 (1971) 871-874.
38. H.E. Carlsson, A.A. Lindberg, S. Hammarstrom, Titration of antibodies to salmonella antigens by enzyme-linked immunosorbent assay, Infection and Immunity 6 (1972) 703-708.
39. J.R. Crowther, ELISA theory and practice, Humana, 1995.
40. "http://www.genoprice.com/DATA%20SHEET/pNPP%20ELISA%20Substrate%20System%20(ELPN-500).pdf."
41. N.S. Hobson, I. Tothill, A.P.F. Turner, Review Article Microbial detection, Biosensors & Bioelectronics 11 (1996) 455-477.
42. R.K. Saiki, S. Scharf, F. Faloona, K.B. Mullis, Enzymatic amplification of β-globin genomic sequences and restriction site analysis for diagnosis of sickle cell anemia, Science 230 (1985) 1350-1354.
43. U. Candrian, Polymerase Chain Reaction in food microbiology, Journal of Microbiological Methods 23 (1995) 89-103.

44. S.B. Primrose, R.M. Twyman, Genomics: Applications in Human Biology, Blackwell, 2003.
45. Y. Kim, T.R. Flynn, R.B. Donoff, D.W. Wong, R. Todd, The gene: The polymerase chain reaction and its clinical application, Journal of Oral and Maxillofacial Surgery 60 (2002) 808-815.
46. S. J. Meltzer, PCR in bioanalysis, Humana, 1998.
47. http://www.cgenetool.com/products/icycler.shtml.
48. P. Leonard, S. Hearty, J. Brennan, L. Dunne, J. Quinn, T. Chakraborty, R. Kennedy, Advances in biosensors for detection of pathogens in food and water, Enzyme and Microbial Technology 32 (2003) 3-13.
49. R.G. Freitag, Biosensors in analytical biotechnology, R G Landes, (1996).
50. M.F. Martin, Progress in Enzyme-Based Biosensors Using Optical Transducers, Microchimica Acta 148 (2004) 107–132.
51. S.Z. Yin, T.S. Yu, and P.B. Ruffin, Fiber Optic Sensors, CRC, 2008.
52. B. Liedberg, C. Nylander, I. Lundstrom, Surface plasmon resonance for gas detection and biosensing, Sensors and Actuators 4 (1983) 299-304.
53. S. Lofas, M. Malmqvist, I. Ronnberg, E. Stenberg, B. Liedberg, I. Lundstrom, Bioanalysis with surface plasmon resonance, Sensors and Actuators B 5 (1991) 79-84.
54. R.M. Sutherland, C. Dahne, biosensors: Fundamentals and applications, Oxford, 1987.
55. X. Fan, I.M. White, S.I. Shopova, H. Zhu, J.D. Suter, Y. Sun, Sensitive optical biosensors for unlabeled targets: A review, Analytica Chimica Acta 620 (2008) 8–26.
56. M.A. Cooper, Optical biosensors in drug discovery, Nature Reviews Drug Discovery 1 (2002) 515-528.

57. M.A. Cooper, Lable-free biosensors techniques and applications, Cambridge, 2009.
58. J. Homola, Present and future of surface plasmon resonance biosensors, Analytical and Bioanalytical Chemistry 377 (2003) 528–539.
59. L.D. Mello, L.T. Kubota, Review of the use of biosensors as analytical tools in the food and drink industries, Food Chemistry 77 **(**2002) 237–256.
60. A.M. Gallardo Soto, S.A. Jaffari, S. Bone, Characterization and optimization of AC conductimetric biosensors, Biosensors & Bioelectronics 16 (2001) 23–29.
61. D.G. Buerk, Biosensors: Theory and Applications, Technomic, (1993).
62. C.S. Lee, S.K. Kim, M. Kim, Ion-Sensitive Field-Effect Transistor for Biological Sensing, Sensors, 9 (2009) 7111-7131.
63. M.S. Belluzo, M.É. Ribone, C.M. Lagier, Assembling Amperometric Biosensors for Clinical Diagnostics, Sensors 8 (2008)1366-1399.
64. V.A. Petrenko, V.J. Vodyanoy, Phage Display for Detection of Biological Threat Agents, Journal of Microbiological Methods 53 (2003) 243-252.
65. R. Raiteri, M. Grattarola, H.J. Butt, P. Skladal, Micromechanical cantilever based biosensors, Sensors and Actuators B 79 (2001) 115-126.
66. M.D. Ward and D.A. Buttry, Insitu Interfacial Mass Detection with Piezoelectric Transducers, Science, 249 (1990)1000-1007.
67. G.C. King, Vibrations and Waves (Manchester Physics Series), Wiley, 2009.
68. N.M. Guilherme, A.C.S. Ferreira, and T. Brigitte, Acoustic wave biosensors: physical models and biological applications of quartz crystal microbalance, Trends in Biotechnology 27 (2009) 689-697.

69. F. Li, H.C. Wang, Q.M. Wang, Thickness shear mode acoustic wave sensors for characterizing the viscoelastic properties of cell monolayer, Sensors and Actuators B 128 (2008) 399–406.
70. G.Z. Sauerbrey, Use of quartz vibrator for weighing thin films on a microbalance, Zeitschrift fuer Physik 155 (1959) 206–212.
71. D.S. Ballantine, R.M. White, Acoustic wave sensors; Theory, Design, and Physic-chemical applications, Academic, 1997.
72. L. Rayleigh, On Waves Propagated along the Plane Surface of an Elastic Solid, Proceedings of the London Mathematical Society 4 (1885) s1-17.
73. R.G. María-Isabel, M.I. Carmen, M.B. Angel, A.V. Antonio, Surface Generated Acoustic Wave Biosensors for the Detection of Pathogens: A Review, Sensors 9 (2009) 5740-5769.
74. B. Drafts, Acoustic Wave Technology Sensors, IEEE Transactions on Microwave Theory and Techniques 49 (2001) 795-802.
75. N.V. Lavrik, M.J. Sepaniak, P.G. Datskos, Cantilever transducers as a platform for chemical and biological sensors, Review of Scientific Instruments 75 (2004) 2229-2253.
76. C. Ziegler, Cantilever-based biosensors, Analytical and Bioanalytical Chemistry 379 (2004) 946-959.
77. L.G. Carrascosa, M. Moreno, M.A. lvarez, L.M. Lechuga, Nanomechanical biosensors: a new sensing tool, Trends in Analytical Chemistry 25 (2006) 196-206.
78. R. Raiteri, M. Grattarola, H.J. Butt, P. Skladal, *Micromechanical* cantilever based biosensors, Sensors and Actuators B 79 (2001) 115-126.

79. M. Su, S. Li, V.P Dravid, Microcantilever resonance-based DNA detection with nanoparticle probes, Applied Physics Letters 82 **(**2003) 3562-3564.
80. B.H. Kim, M. Maute, E. Prins, D.P. Kern, M. Croitoru, S. Raible, U. Weimar, W. Gopel, Microelectronic Engineering 53 (2000) 229-232.
81. A. Mehta, S. Cherian, D. Hedden, T. Thundat, Manipulation and controlled amplification of Brownian motion of microcantilever sensors, Applied Physics Letters 78 (2001) 1637-1639.
82. L.D. Landaum , E.M., Lifshitz, Theory of Elasticity, Pergamon, 1986.
83. S.Q. Li and Z.-Y. Cheng, Nonuniform mass detection using magnetostrictive biosensors operating under multiple harmonic resonance modes, Journal of Applied Physics 107 (2010) 114514/1-114514/6.
84. T. Kobayashi, J. Tsaur, M. Ichiki, R. Maeda, Fabrication and performance of a flat piezoelectric cantilever obtained using a sol–gel derived PZT thick film deposited on a SOI wafer, Smart Material Structure 15 (2006) S137–S140.
85. T.P. Burg, M. Godin, S.M. Knudsen, W. Shen, G. Carlson, J.S. Foster, K. Babcock, S.R., Manalis, Weighing of biomolecules, single cells and single nanoparticles in fluid, Nature 446 (2007) 1066–1069.
86. L.L. Fu, S.Q. Li, K.W. Zhang, I.H. Chen, V.A. Petrenko, Z.-Y. Cheng, Magnetostrictive microcantilever as an advanced transducer for biosensor, Sensors 7 (2007) 2929-2941.
87. R. Guntupalli, J. Hu, R.S. Lakshmanan, T.S. Huang, J.M. Barbaree, B.A. Chin, Rapid and sensitive magnetoelastic biosensors for the detection of *Salmonella typhimurium* in a mixed microbial population, Biosensors and Bioelectronics 22 (2007) 1474–1479.

88. S.Q. Li, L.L. Fu, J.M. Barbaree, Z.-Y. Cheng, Resonance behavior of magnetostrictive micro/milli-cantilever and its application as a biosensor, Sensors and Actuator B 137 (2009) 692-699.

89. R.S. Lakshmanan, R. Guntupalli, J. Hu, V.A. Petrenko, J.M. Barbaree, B.A. Chin, Detection of *Salmonella typhimurium* in fat free milk using a phage immobilized magnetoelastic sensor, Sensors and Actuator B 126 (2007) 544-550.

90. C.H. Yang, Y.M. Wen, P. Li, L.X. Bian, Influence of bias magnetic field on magnetoelectric effect of magnetostrictive/elastic/piezoelectric laminated composite, Acta Physica Sinica 57 (2008) 7292-7297.

91. L.L. Fu, K.W. Zhang, S.Q. Li, Y.H. Wang, T.S. Huang, A.X. Zhang, Z.-Y. Cheng, In situ real-time detection of E. coli in water using antibody-coatedmagnetostrictive microcantilever, Sensors and Actuators B (2010) 220-225.

92. L.L. Fu, S.Q. Li, K.W. Zhang, Z.-Y. Cheng, Detection of Bacillus Anthracis Spores Using Magnetostrictive Microcantilever-based Biosensor, Proceedings of MRS, 2006.

93. C.A. Grimes, K.G. Ong, K. Loiselle, P.G. Stoyanov, D. Kouzoudis, Y. Liu, C. Tong and F. Tefiku, Magnetoelastic sensors for remotequery environmental monitoring, Smart Matererials and Structures 8 (1999) 639–646.

94. R.S. Lakshmanan, R. Guntupallia, J. Hu, D.J. Kim, V.A. Petrenko, J.M. Barbaree and B.A. Chin, Phage immobilized magnetoelastic sensor for the detection of *Salmonella typhimurium*, Journal of Microbiological Methods 71(2007) 55-60.

95. S.J. Huang, P.F. Pang, X.L. Xiao, L.W. He, Q.Y. Cai and C.A. Grimes, A wireless remote-query sensor for real-time detection of *Escherichia coli* O157:H7 concentrations, Sensors and Actuators B 131 (2008) 489–495.

96. W. Shen, R.S. Lakshmanan, L.C. Mathison, V.A. Petrenko, B.A. Chin, Phage coated magnetoelastic micro-biosensors for real-time detection of *Bacillus anthracis* spores Sensors and Actuators B 137 (2009) 501–506.

97. S.J. Huang, Y.J Wang, Q.Y. Cai, J.D. Fang, Detection of *Staphylococcus Aureus* in Different Liquid Mediums Using Wireless Magnetoelastic Sensor, Chinese Journal of Analytical Chemistry, 38 (2010) 105–108.

98. C.A. Grimes, C.S. Mungle, K.F. Zeng, M.K. Jain, W.R. Dreschel, M. Paulose, K.G. Ong, Wireless Magnetoelastic Resonance Sensors: A Critical Review, Sensors 2 (2002) 294-313.

99. C. Liang, S. Morshed, B.C. Prorok, Correction for longitudinal mode vibration in thin slender beams, Applied Physics Letters, 90 (2007) 221912-221914.

100. P.G. Stoyanov, C.A. Grimes, A remote query magnetostrictive viscosity sensor, Sensors and Actuators A 80 (2000) 8–14.

101. M.K. Jain, and C.A. Grimes, Effect of surface roughness on liquid property measurments using mechanically oscillating sensors, Sensors and Actuators A, 100 (2002), 63-69.

102. R. Schumacher, G. Borges, K.K. Kanazawa, the quartz microbalance: a sensitive tool to probe surface reconstruction’s on gold electrodes in liquid, Surface Science, 163 (1985) L621-L626.

103. E. Lacheisserie, Magnetostriction - Theory and Applications of Magnetoelasticity: CRC, 1993.

104. E.T. Lacheisserie, D. Gignoux, M. Schlenker, Magnetism - Materials and Applications, Springer, 2004.

105. Metglas, “http://www.metglas.com/PRODUCTS/page5_1_2_7_1.htm.”

106. C. Liang, S. Morshed, B.C. Prorok, Correction for longitudinal mode vibration in thin slender beams, Applied Physics Letters, 90 (2007) 221912-221914.

107. M.L. Johnson, J.H. Wan, S.C. Huang, Z.-Y. Cheng, V.A. Petrenko, D.J. Kim, I.H. Chen, J.M. Barbaree, J.W. Hong, B.A. Chin, A wireless biosensor using microfabricated phage-interfaced magnetoelastic particles, Sensors and Actuators A 144 (2008) 38–47.

108. S.Q. Li, Development of novel acoustic wave biosensor platforms based on magnetostriction and fabrication of magnetostrictive nanowires, Dissertation, Auburn University, 2007.

109. M.L. Johnson, J.H. Wan, S.C. Huang, Z.-Y. Cheng, V.A. Petrenko,D.J. Kim, I.H. Chen, J.M. Barbaree, J.W. Hong, B.A. Chin, wireless biosensor using microfabricated phage-interfacedmagnetoelastic particles, Sensors and Actuators A 144 (2008) 38–47A.

110. L. Olofsson, J. Ankarloo, P.O. Andersson, I.A. Nicholls, Filamentous bacteriophage stability in non-aqueous media, Chemistry & Biology 8 (2001) 661-671.

111. J. Lopez, R.E. Webster, Morphogenesis of filamentous bacteriophage f1: orientation of extrusion and production of polyphage, Virology 127 (1983) 177-193.

112. B. Vidova, A. Godany, E. Sturdik, Phage Display- A Tool For Detection And Prevention Against Pathogens A Review, Nova Biotechnologica 8 (2008) 23-33.

113. P. Model, M. Russel, Filamentous bacteriophage, Plenum, 1988.

114. V.A. Petrenko, G.P. Smith, Phages from landscape libraries as substitute antibodies, Protein Engineering 13 (2000) 589-592.

115. J. Maynard, G. Georgiou, antibody engineering, Annual Review of Biomedical Engineering 2 (2000) 339-376.

116. J.M. Woof, D.R. Burton, Human antibody–Fc receptor interactions illuminated by crystal structures, Nature Reviews Immunology 4 (2004) 89-99.

117. V.A., Petrenko, and V.J. Vodyanoy, Phage display for detection of biological threat agents, Journal of Microbiological Methods 53 (2003) 253– 262.

118. N.S. Lipman, L.R. Jackson, L.J. Trudel, F. Weis-Garcia, Monoclonal versus polyclonal antibodies: distinguishing characteristics, applications, and information resources, International League of Associations for Rheumatology 46 (2005) 258-68.

CHAPTER 2

RESONANCE BEHAVIOR OF MSP AND INFLUENCE OF SURROUNDING MEDIA

2.1 Introduction

The resonance behavior of an MSP is used as discussed in Chapter 1 as a biosensor platform. The resonance behavior of an acoustic resonator depends on many factors, such as the materials' properties, media around the resonator, and the surface roughness of the resonator. Regarding the application of the biosensors, most of analytes are liquid. Therefore, it is of interest to understand the resonance behavior of an MSP in liquid or other viscous media. Although some formulas have been introduced to describe the influence of the media on the resonance behavior, it is still desirable to experimentally study the influence of the media on the resonance behavior since there are too many assumptions used in the derivation of these formulas. The resonance behavior of an acoustic resonator is characterized by two important parameters: resonance frequency and *Q* value. In this chapter, both the resonance frequency and the *Q* value of MSPs with different sizes/dimensions will be studied in different media.

2.2 Characterization of the resonance behavior of an MSP

The resonance frequency of an MSP can be directly determined using its oscillation amplitude at different frequencies since the oscillation amplitude reaches its maximum at the resonance frequency. The resonance frequency can also be indirectly determined by using the electrical properties of an MSP. For example, if the impedances of a coil with an MSP inside are determined at frequencies over a broad range which covers the

resonance frequency of the MSP, the impedance versus frequency curve (impedance spectrum) can be used to determine the resonance frequency and the *Q* value of the MSP. In this study, the so-called S_{11} signal rather the real impedance is used to determine the resonance behavior. Actually, the S_{11} signal is directly related to the impedance (*Z*) as [1]

$$Z = 50\frac{1+S_{11}}{1-S_{11}} \qquad (2\text{-}1)$$

where S_{11} and *Z* are complex numbers.

The S_{11} signal of an MSP in a coil is determined by using the HP network analyzer (8751A) with an S-parameter test set (87511A). The scheme of the measurement setup is shown in **Figure 2-1**, where the magnet is used to generate a dc magnetic field on the MSP and an ac magnetic field is generated by the coil with a current controlled by the S-parameter unit.

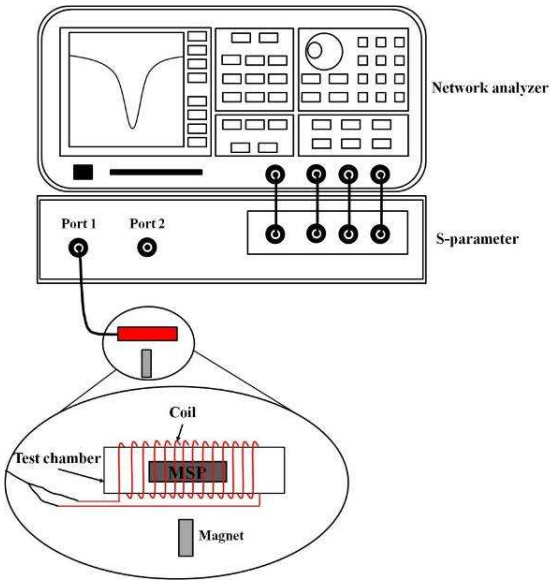

Figure 2-1 Configuration of a network analyzer with an S-parameter test set [2].

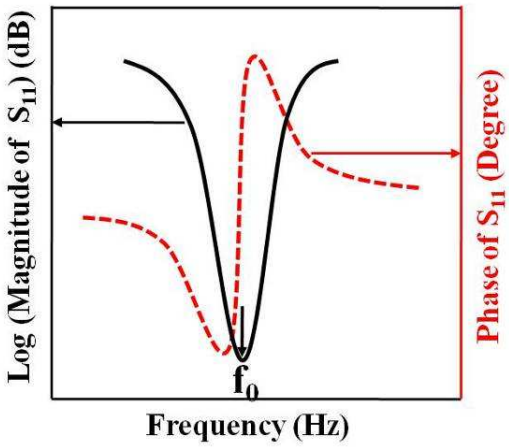

Figure 2-2. A typical magnitude and phase curve of S_{11} parameter changing with the frequency of an MSP.

A set of typical results is shown in **Figure 2-2**, where both the phase and amplitude of the S_{11} signal are plotted versus frequency. It is known that the resonance frequency of

the MSP is the frequency (f_0) at which the amplitude of the S_{11} signal reaches its minimum [2]. The Q value of the MSP is also determined by the amplitude of the S_{11} signal as

$$Q = \frac{f_0}{\Delta f} \qquad \text{(1-5)/(2-2)}$$

where Δf is the width of the amplitude at its half height as described in Chapter 1.

2.3 Materials and methods

The MSPs used in this study were fabricated from a commercially available magnetostrictive alloy – Metglas™ 2826MB (iron nickel-based alloy). The Metglas™ 2826MB in a ribbon form was obtained from Honeywell International (Conway, SC). To fabricate the MSPs, a sheet of Metglas™ ribbon was cut into rectangular pieces using a micro wafer dicing saw Model 1110 (From Micro Automation). After dicing, these MSPs were cleaned in methanol using an ultrasonic cleaner (Cole Parmer 8891) for 30 minutes and dried using nitrogen gas. Finally, these MSPs were then used to study the resonance behavior. The real dimension of each MSP used in the experiment was measured using EDMUND optics' 6X pocket comparator within an accuracy of 0.1 mm.

Table 2-1. Designed dimensions of MSPs used in the experiments.

L(mm) / W(mm)	1	2	4	6	8	10	15	L/W
		1	2		4		7.5	2
	0.33	0.67	1.33	2		3.33		3
		0.5	1		2		3.75	4
				1		1.67		6
					1		1.88	8
						1		10
							1	15

Table 2-1 gives the designed dimensions of the MSPs used in the experiments.

These MSPs cover a range of the length from 1 mm to 15 mm, which correspond to the resonance frequency ranging from 150 kHz to more than 2 MHz, and the length/width ratio from 2 to 15.

To study the media influences on the resonance behavior of MSPs, air and a total of six liquids including water as listed in **Table 2-2** were used in the experiments.

Table 2-2. The densities and dynamic viscosities of air and the selected liquids at 20°C.

Media	Density (g/cm^3)	Viscosity(cP)
Air	1.205×10^{-3} [3]	1.8×10^{-2} [4]
Hexane	0.6594 [5]	0.31 [5]
Ethanol	0.7893 [5]	1.22 [5]
Water	0.9982 [6]	1.0 [5]
2-propanol	0.7863 [5]	2.27 [5]
4-methy1-2-pentanol	0.8079 [5]	5.2 [5]
Ethylene glycol	1.1132 [5]	21 [5]

2.4 Results and discussion

2.4.1 Resonance frequency of MSPs

In this study, the resonance frequency of an MSP in air is treated as the intrinsic frequency. That is, the resonance frequency of an MSP can be expressed as [7]

$$f_n = \frac{n}{2L}\nu \qquad (n = 1, 2, 3,\ldots) \qquad \text{(1-11)/(2-3)}$$

where f_n is the resonance frequency of the nth harmonic mode, L is the length of the MSP, ν is the acoustic velocity of the magnetostrictive material and usually treated as a constant.

Figure 2-3(a) shows the experimental results for all the MSPs studied here, where the symbols are the experimental results and the solid line is the linear fitting results. Clearly, the experimental results fit Equation (2-3) well. That is, the resonance frequency is linearly dependent on the inverse length.

Equation (2-3) can be rewritten as

$$2 \cdot L \cdot f_n = n \cdot v = n \cdot \sqrt{\frac{E}{\rho(1-\sigma^m)}} \qquad (n = 1, 2, 3,\ldots) \qquad (2\text{-}4)$$

The results shown in **Figure 2-3(a)** are re-plotted in **Figure 2-3(b)**, where "$2Lf_1$" is plotted versus the L. Based on Equation (2-4), one would expect the "$2Lf_1$" have a constant value.

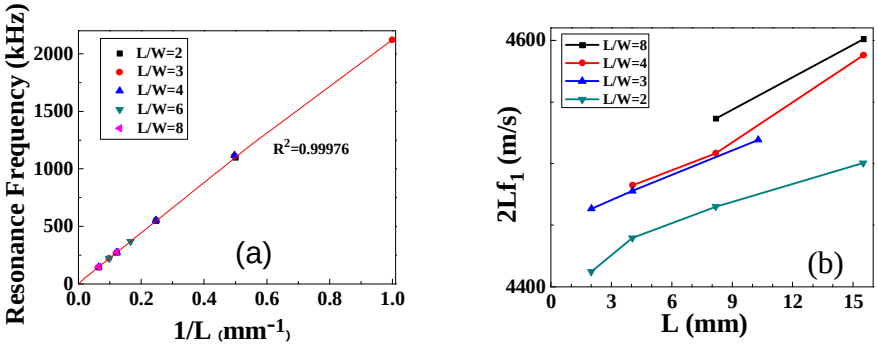

Figure 2-3. Resonance frequency (f_1) of the 1st harmonic mode (n = 1) of MSPs (a) the resonance frequency (f_1) in relation to $1/L$, (b) the $2 \cdot L \cdot f_1$ in relation to L. Here f_1 and L are experimental results.

From the results shown in **Figure 2-3(b)**, one can clearly find that, first of all, the "$2Lf_1$" increases with increasing L for a constant L/W ratio. In other words, the apparent "acoustic velocity" increases with increasing L or the apparent "acoustic velocity" increases with decreasing frequency. It is expected that the value of m is the same for the MSP with the same L/W ratio. Therefore, the results here indicate that the elastic properties (i.e. E and σ) of the materials change with the frequency. The increasing apparent "acoustic velocity" means an increasing E or σ. That is, as the frequency increases, both E and σ or either E or σ decreases. If the Poisson's ratio is a constant, this means that the E increases with decreasing frequency, which is beyond the current knowledge. If one assumes the E is independent of the frequency, one would expect that

the Poisson's ratio increases with decreasing frequency.

The results shown in **Figure 2-3(b)** also indicate that the *L/W* ratio has a clear influence on the "$2Lf_1$" value or apparent "acoustic velocity." This can be more clearly shown in **Figure 2-4**. Clearly, for the MSPs with the same length, the apparent "acoustic velocity" increases with the *L/W* ratio. Since the resonance frequency for the MSPs with the same length is almost the same as shown in **Figure 2-3(a)**, one would not expect the changes in the elastic properties of the materials. Therefore, the results shown in **Figure 2-4** indicate that the *m* value continuously changes with the *L/W* ratio. As the *L/W* ratio increases, the value of *m* decreases. Therefore, the reported value of *m* may present two extreme cases: 1) the *L/W* is much big than 1, *m* = 1 or 2) the *L/W* is very close to one, *m* = 2. In reality, the value of *m* for a real MSP is somewhere in between.

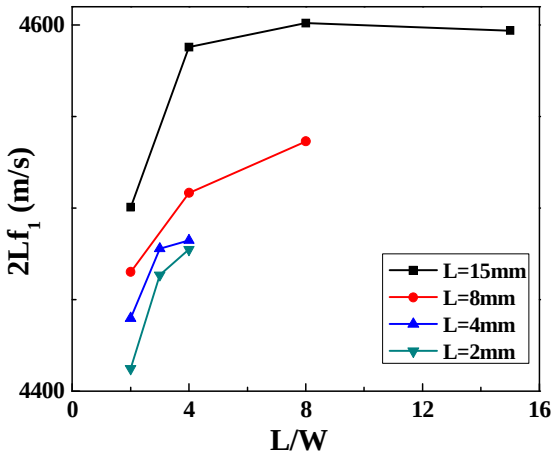

Figure 2-4. $2Lf_1$ in relation to *L* for the MSPs with different *L/W*

2.4.2 The *Q* value of MSPs

To further study the resonance behavior of the MSPs, the *Q* values of the MSPs studied above were determined using the experimental results. First of all, it was found that the *Q* value of the MSPs was about 1000 depending on the size of the MSP. This *Q*

value is certainly higher than the *Q* value of the MCs. This is one of the advantages of the MSPs over the MCs. However, it has to be pointed that the *Q* value reported here is much smaller than the *Q* value of the QCM. For a free standing MSP, the intrinsic *Q* value reflects the mechanical loss of the magnetostrictive alloy. A *Q* value of 1000 means that the magnetostrictive alloy used here has a considerable mechanical loss. For a material with considerable mechanical loss, the loss should be dependent on the frequency.

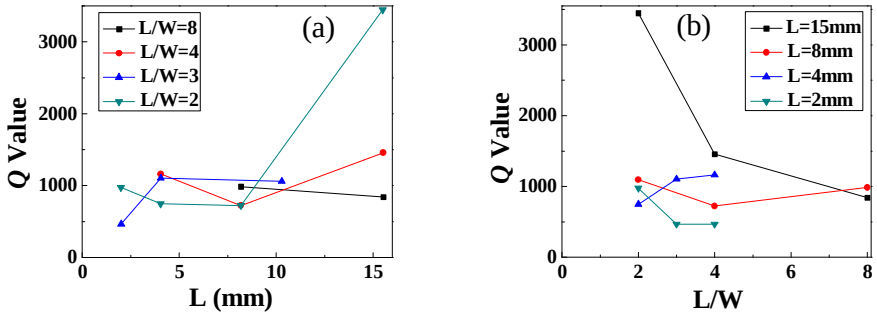

Figure 2-5. The *Q* value of MSPs with different sizes and geometries: (a) the *Q* value in relation to L, (b) the *Q* value in relation to *L/W* ratio.

Figure 2-5 shows the dependence of the *Q* value on the length and *L/W* ratio of the MSPs. It has to be mentioned that in the experiments the dc magnetic field was not fixed. For the MSPs with the same *L/W* ratio, the dc magnetic field increased with decreasing *L*. It is known that for a single MSP the *Q* value increases with the dc magnetic field [8]. However, the results shown in **Figure 2-5(a)** indicate that the *Q* determined experimentally may increase with the length. These means that the smaller the *L* (i.e. the higher the resonance frequency), the lower the *Q* value. Since these *Q* values are the intrinsic values, the results show that the mechanical loss of the magnetostrictive alloy used increases with the frequency over the frequency range studied here. For the MSPs with the same length, the dependence of the *Q* value on the *L/W* ratio is given in **Figure**

2-5(b). It seems there is no clear trend here. One of the reasons may be related to the dc magnetic field. As mentioned above, the dc magnetic field used in the experiments was not fixed.

1.4.3 Resonance frequency of MSP in liquid

Figure 2-6 shows the experimental results about the resonance frequency as the function of inverse length for different MSPs in all six liquids. Although these liquids have different properties, a linear relation between the resonance frequency and the inverse length is found for each liquid.

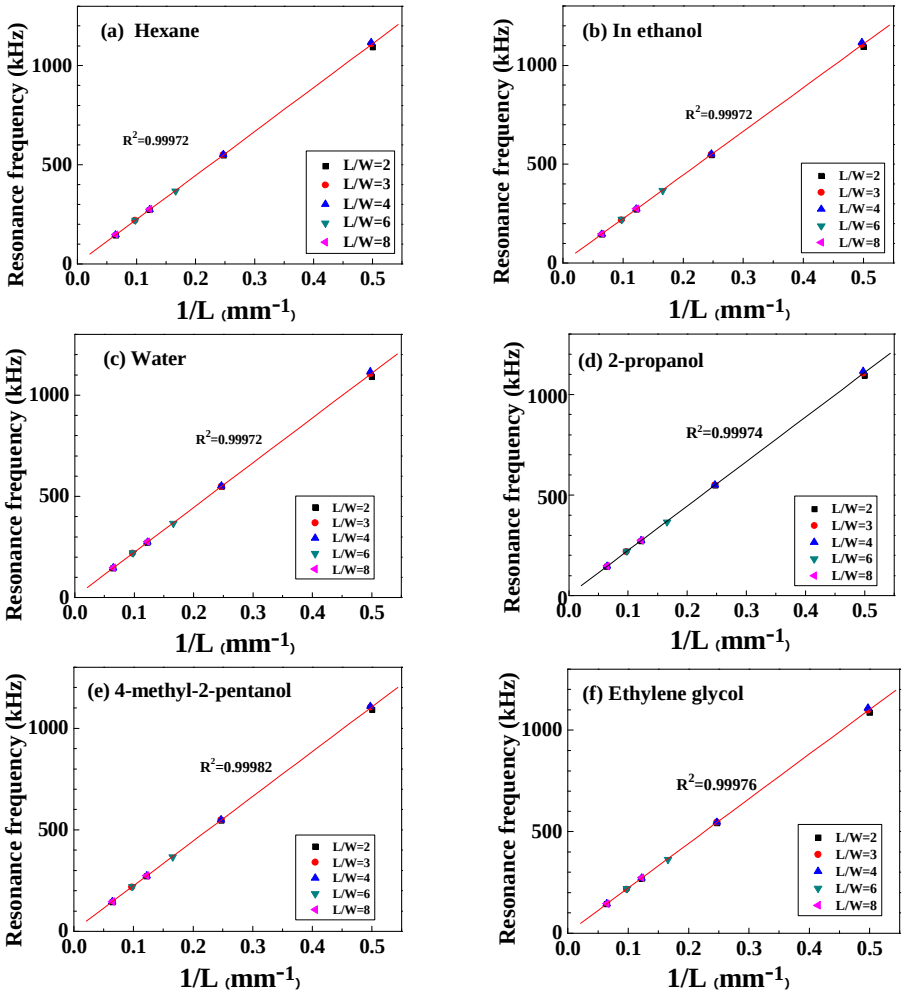

Figure 2-6. The length dependence of the resonance frequency ($f_{1,l}$) of first harmonic mode for MSPs in different liquids: (a) hexane, (b) ethanol, (c) water, (d) 2-propanol, (e) 4-methyl-2-pentanol, and (f) ethylene glycol, respectively.

To further study it, the apparent "acoustic velocity" or "$2 \cdot L \cdot f_{1,l}$" of the MSPs in each liquid was plotted as the function of length for MSPs in different liquids is shown in **Figure 2-7**. Again, it was found that in each liquid the apparent "acoustic velocity" increased with increasing length of the MSP.

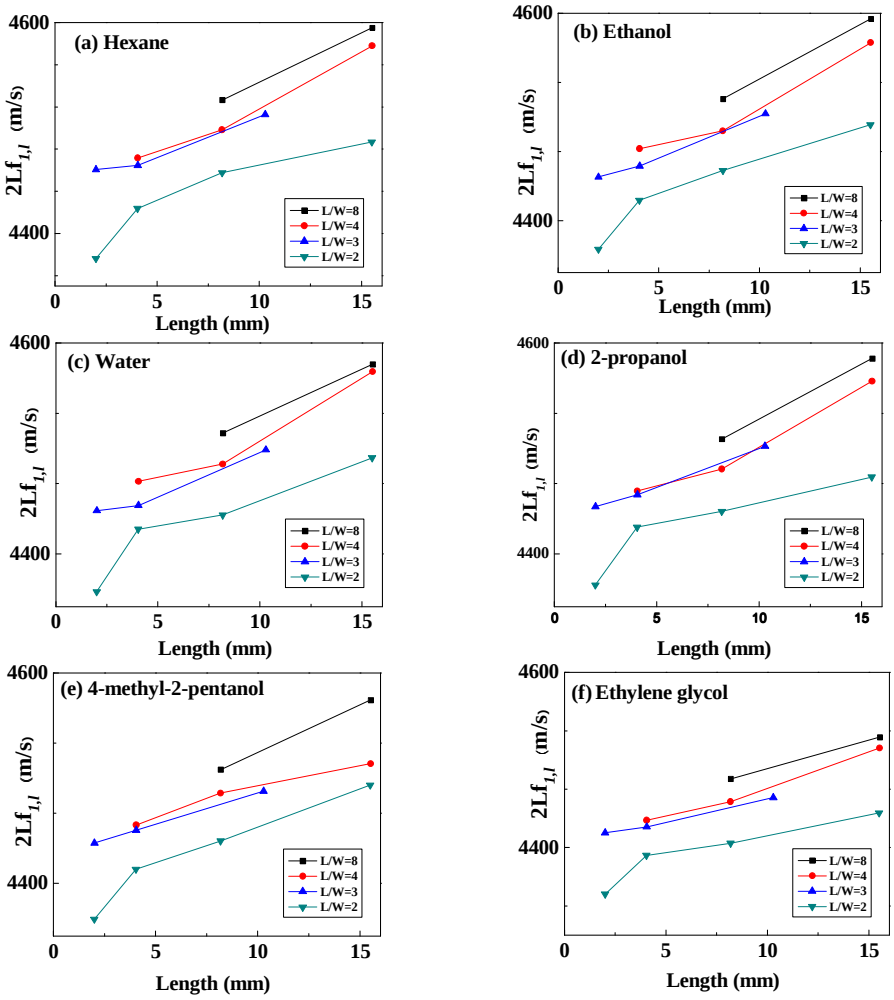

Figure 2-7. The "$2 \cdot L \cdot f_{1,l}$" in relation to the L for the MSPs with different L/W ratio, where the $f_{1,l}$ is the resonance frequency of the first harmonic mode of MSPs in liquids: (a) hexane, (b) ethanol, (c) water, (d) 2-propanol, (e) 4-methyl-2-pentanol, and (f) ethylene glycol.

To study the influence of the L/W ratio on the resonance behavior, the apparent "acoustic velocity" was plotted as the function of the L/W ratio for the MSPs with the same length as shown in **Figure 2-8**. Again, the apparent "acoustic velocity" of the MSP in each liquid increases with increasing L/W ratio.

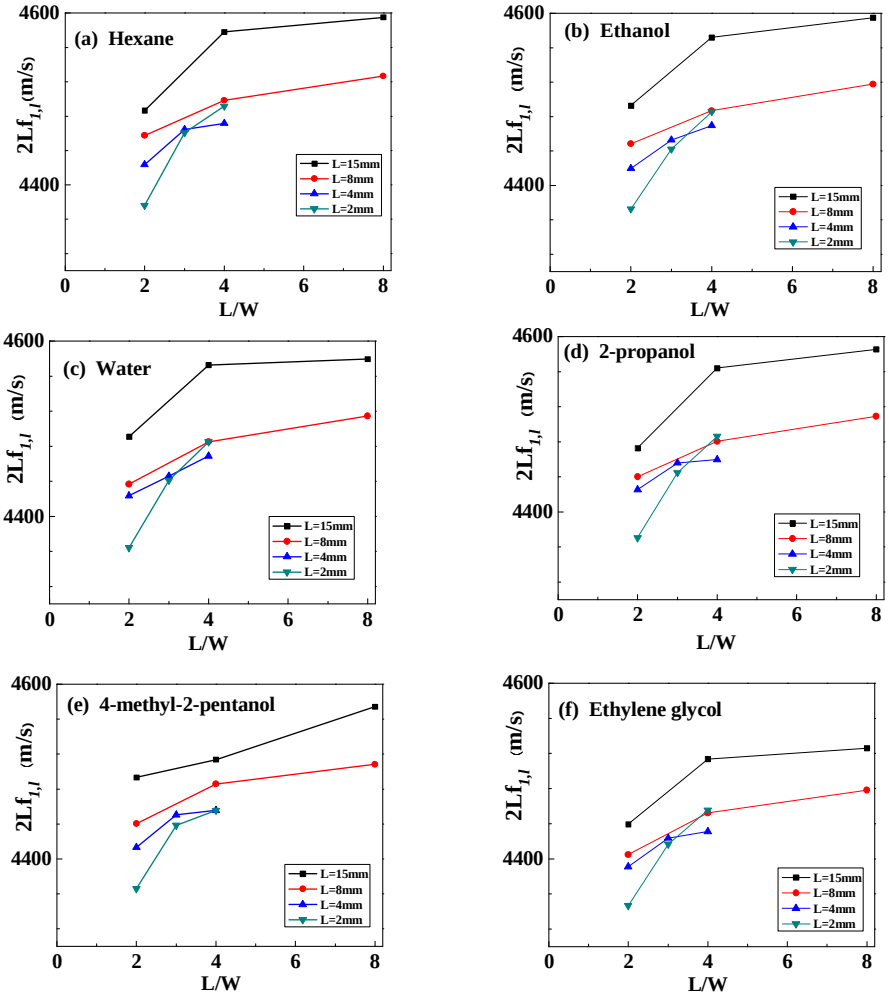

Figure 2-8. The "$2 \cdot L \cdot f_{1,l}$" in relation to the *L/W* ratio for the MSPs with different lengths, where the $f_{1,l}$ is the resonance frequency of the first harmonic mode of MSPs in liquids: (a) hexane, (b) ethanol, (c) water, (d) 2-propanol, (e) 4-methyl-2-pentanol, and (f) ethylene glycol.

2.4.3 Determination of surface roughness R_{ave}

As discussed above, surface roughness affects the resonance behavior and lowers the resonance frequency of an MSP. Therefore, it is of interest to determine the surface roughness of MSP sensors and its influence on the resonance frequency. In the current literature, the surface roughness of an MSP resonator is determined using the resonance frequency of an MSP in different liquids. The principle used here is based on the

Equation (1-18). That is, the change in resonance frequency can be written as:

$$\Delta f_n = -\frac{\sqrt{\pi f_n}}{2\pi\rho d}(\eta\rho_l)^{1/2} - f_n\frac{\rho_l R_{ave}}{\rho d} \qquad \text{(1-18)/(2-5)}$$

where Δf_n (= $f_{n,l} - f_n$) is the difference in the resonance frequency of an MSP observed in liquid and air; f_n is the nth intrinsic resonance frequency of the MSP (in air here) and $f_{n,l}$ is the resonance frequency of the MSP in liquid; ρ, d, and R_{ave} are the density, thickness, and the average surface roughness of the MSP, respectively, and η, ρ_l are the viscosity and density of the liquid, respectively.

If an MSP is tested in different media, f_n, d, ρ, and R_{ave} are constants. Therefore, Equation (2-5) can be rewritten as

$$\Delta f_n / \rho_l = A \cdot (\eta / \rho_l)^{1/2} + B \qquad \text{(2-6)}$$

where $A = -\frac{\sqrt{\pi f_n}}{2\pi\rho_S d}$ and $B = -f_n\frac{R_{ave}}{\rho_S d}$. That is, for an MPS, the A and B are two constants. If the value of the B is determined, the R_{ave} can be obtained.

The results shown in **Figure 2-9** are the resonance frequencies of two similar sizes of MSPs in different liquids when the first harmonic mode was used. Likely, a linear relationship was observed for both. By fitting the relationship using Equation (2-6), the values of A and B were determined and the surface roughness could be calculated using the B. The results are given in **Table 2-3 and Table 2-4**. These two MSPs' results with the same surface roughness for the MSPs, which is very encouraging. This is the current method from the literature to determine the surface roughness of an MSP [8].

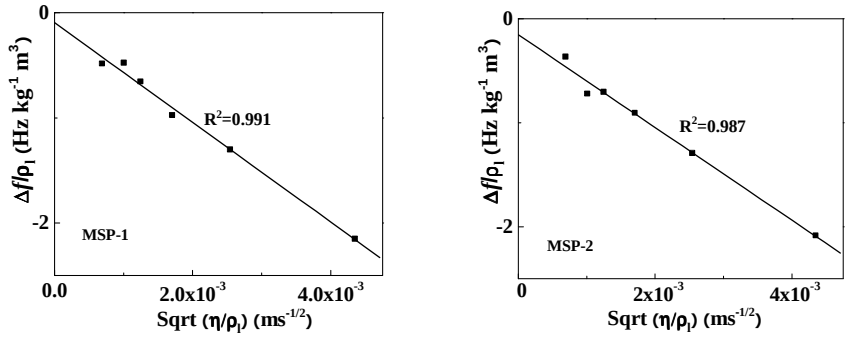

Figure 2-9. $\Delta f_n/\rho_l$ *vs.* $\sqrt{\eta/\rho_l}$ for two similar MSPs in different liquids: (a) MSP-1 with a size of 15.52 mm x 3.78 mm x 30 µm, (b) MSP-2 with a size of 15.58 mm x 3.76 mm x 30 µm. Here the MSPs were operated at first harmonic mode.

Table 2-3. *A* and *B* values for the MSP-1 operated at different harmonic modes.

Harmonic mode (MSP-1)	f_n *(Hz)*	*A* ($Hz^{-1/2}kg^{-1}m^2$)	*B* ($Hzkg^{-1}m^3$)	R_{ave} (µm)
1st	147815	-475	-0.09319	0.15
3rd	430971	-864	-0.47241	0.26
5th	633835	-922	-1.79911	0.67

Table 2-4. *A* and *B* values for the MSP-2 operated at different harmonic modes.

Harmonic mode (MSP-2)	f_n *(Hz)*	*A* ($Hz^{-1/2}kg^{-1}m^2$)	*B* ($Hzkg^{-1}m^3$)	R_{ave} (µm)
1st	146409	-446	-0.15402	0.25
3rd	418203	-835	-0.55000	0.31
5th	620899	-852	-2.1657	0.83

To further confirm/verify the results, two higher orders of harmonic mode are used as shown in **Figure 2-10**, where the results obtained using 3rd and 5th harmonic modes are presented. Clearly, the linearity of the relationship between $\Delta f_n/\rho_l$ and $\sqrt{\eta/\rho_l}$ is not good as was observed for the first harmonic mode. By comparing the results shown in **Figures 2-9** and **2-10**, one can find that the higher the order of harmonic mode, the worse the linear relationship observed.

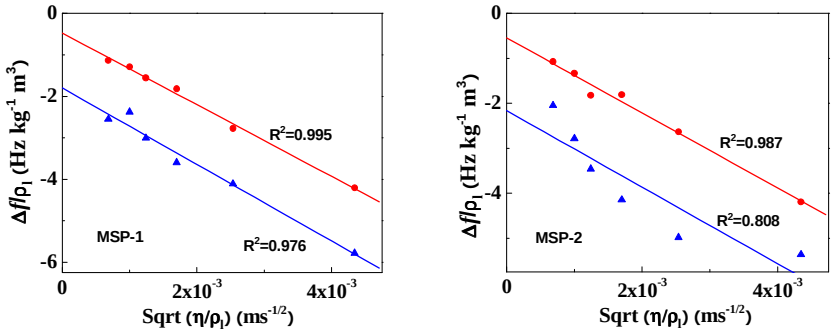

Figure 2-10. $\Delta f_n / \rho_l$ *vs.* $\sqrt{\eta / \rho_l}$ for two similar MSPs in different liquids: (a) MSP-1 with a size of 15.52 mm x 3.78 mm x 30 µm, (b) MSP-2 with a size of 15.58 mm x 3.76 mm x 30 µm. Here the MSPs were operated at 3rd and 5th harmonic modes.

When the approach used above was employed to analyze the 3rd and 5th harmonic results, the surface roughness was determined as shown in **Tables 2-3** and **2-4**. The surface roughness of the MSP was calculated based on the *B* values for the three harmonic modes as shown in **Tables 2-3** and **2-4**. Although the surface roughness obtained for two MSPs is the same by using the same order of harmonic mode, the surface roughness determined from the results of different orders of harmonic modes is different. This is not reasonable since the surface roughness as a property of an MSP should be independent on the operating frequency or harmonic mode.

2.4.4 Factors that affect the measured surface roughness R_{ave}

To experimentally provide more information for the simulation of the influence of the friction force from surrounding viscous media on the resonance behavior of MSPs, MSPs with different sizes and geometries were studied.

a) MSPs with the same width but different lengths

The results shown in **Figure 2-12** are the resonance frequencies of the MSPs of the same width but different lengths in different liquids, where the first harmonic mode was

used. Likely, a linear relationship is also observed for the three different lengths of MSPs. However, it seems that the linearity of this relationship is related to the length of the MSP. The smaller the length-to-width ratio, the closer the linear relationship. If the results are fitted using Equation (2-6), the values of *A* and *B* are obtained and the surface roughness is then calculated using the *B* value and other information about the MSP. The fitting results and the calculated surface roughness are given in **Table 2-6**, where the results from two MSPs used above (i.e. **Tables 2-3** and **2-4**) are also presented.

For all these MSPs, the same surface roughness is expected. However, the results given in **Table 2-6** indicate clearly difference. Considering the geometry and the final surface roughness, it seems that the length of the MSPs plays some role on the fine surface roughness.

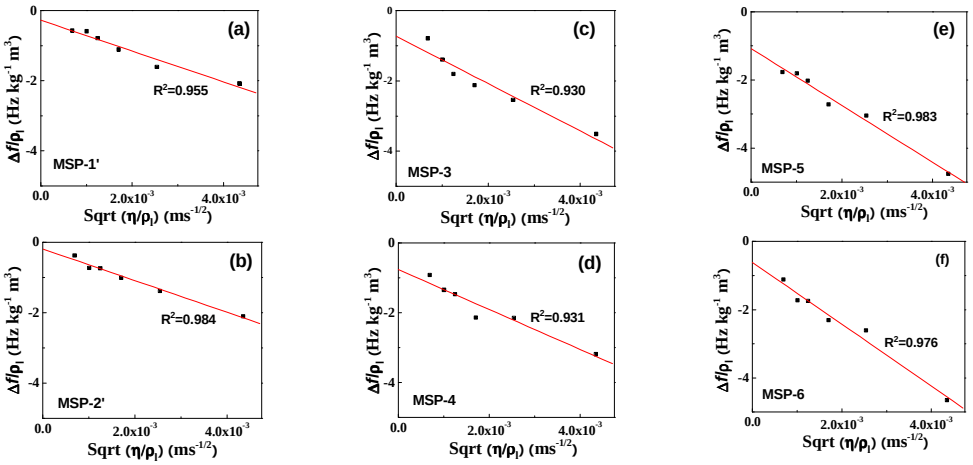

Figure 2-11. $\Delta f_n / \rho_l$ *vs.* $\sqrt{\eta / \rho_l}$ for MSPs with the same width but different lengths in different liquids, where the MSPs were operated at first harmonic mode. (a) MSP-1' (15.40 mm x 1.00 mm x 30 µm), (b) MSP-2' (15.65 mm x 1.00 mm x 30 µm), (c) MSP-3 (7.98 mm x 1.00 mm x 30 µm), (d) MSP-4 (8.18 mm x 1.00 mm x 30 µm), (e) MSP-5 (4.00 mm x 1.00 mm x 30 µm), and (f) MSP-6 (4.07 mm x 1.00 mm x 30 µm).

Table 2-5. *A* and *B* values for the MSP-1 operated at 1st harmonic mode.

MSP		f_1 *(Hz)*	*A* ($Hz^{-1/2}kg^{-1}m^2$)	*B* ($Hz \cdot kg^{-1}m^3$)	R_{ave} (μm)
MSPs used above	15.52mm x 3.78mm x 30 μm	147815	-475	-0.09319	0.15
	15.58mm x 3.76mm x 30 μm	146409	-446	-0.15402	0.25
15.40mm x 1.00mm x 30μm		148196	-440	-0.27472	0.44
15.65mm x 1.00mm x 30μm		146340	-450	-0.18635	0.30
7.98mm x 1.00mm x 30μm		282386	-674	-0.72870	0.61
8.18mm x1.00mm x 30μm		276951	-573	-0.75989	0.65
4.00mm x 1.00mm x 30μm		560044	-834	-1.08027	0.46
4.07mm x 1.00mm x 30μm		542320	-905	-0.61579	0.27

b) MSPs with the same length but different widths

The results obtained from MSP-1 and MSP-2 (i.e. **Figure 2-9** and **Table 2-4**) are compared with the results obtained from MSP-1' and MSP-2' (i.e. **Figure 2-12** and **Table 2-6**) to find the influence of the width on the results.

The results shown in **Figure 2-10 and 2-12(a)-(b)** are the resonance frequencies of the MSPs in the same length but different widths in different liquids, where the first harmonic mode was used. Again, a linear relationship is observed for the two different widths of MSPs. However, it seems that the linearity of this relationship is related to the width of the MSP. The fitting results and the calculated surface roughness are given in **Table 2-6**. The results given in **Table 2-6** clearly indicate some difference. It seems that the width of the MSPs plays some role in the determination of surface roughness based on the current method.

New Method: In the method used above, in order to determine the surface roughness of an MSP, multiple liquids are needed. Therefore, both the complexity of the liquid influence on the resonance frequency and the influence of different harmonic modes on

the resonance frequency are included in the process. To limit the number of the factors that may influence the results, the results from each individual liquid were used independently. In order to do so, Equation (2-5) is re-arranged as

$$\Delta f_n = C \cdot \sqrt{f_n} + D \cdot f_n \qquad (2\text{-}7)$$

where C and D are constant for a single MSP in one liquid and the D is related to the surface roughness, that is $D = -\frac{\rho_l R_{ave}}{\rho_s d}$. Therefore, if the value of D is determined, the surface roughness can be determined. In this case, in order to determine the surface roughness of an MSP, multiple harmonic resonance frequencies and single liquid are needed.

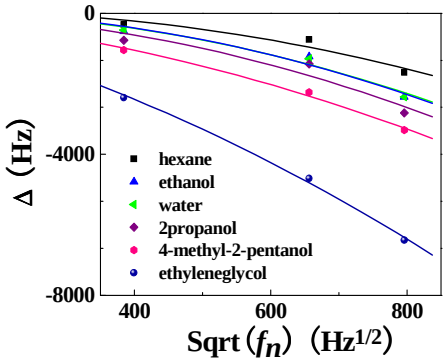

Figure 2-12. Δf_n in relation to $(f_n)^{0.5}$ for an MSP in different media. The size of the MSP is 15.52 mm x 3.78 mm x 30 μm and three harmonic modes (1^{st}, 3^{rd}, 5^{th}) are

The results obtained from one MSP (in the size of 15.52 mm x 3.78 mm x 30 μm) in different liquids are shown in **Figure 2-11**, where the difference (Δf_n) in the resonance frequencies of the MSP in liquid and air are plotted as the function of the square root of the resonance frequency of the MSP in air for all the three harmonic modes (1^{st}, 3^{rd}, and 5^{th} order harmonic modes). The values of C & D were determined by fitting the results

obtained in each liquid using Equation (2-7), as shown in **Table 2-5**. The surface roughness was then calculated from the value of *D* and the density of the corresponding liquid and the properties/parameters of the MSP. The calculated surface roughness is also given in **Table 2-5**. From the results, one can find that the surface roughness obtained from different liquids is very close to each other. Considering the surface roughness calculated from the value of *D* is obtained from the same experiment results used in above to determine the surface roughness using the value of *B*, one would conclude that this new approach is better than the one currently used in the literature in terms of determination of the surface roughness.

Table 2-6. *C* and *D* values for one MSP operated at different harmonic modes.

Media	f_n and $f_{n,l}$(Hz)			*C* ($Hz^{-1/2}$)	*D* ($x10^{-3}$)	R_{ave} (μm)
	1st	3rd	5th			
Air	147815	430971	633835			
Hexane	147498	430223	632156	0.86331	-3.54879	1.28
Ethanol	147301	429742	631463	0.70022	-4.31646	1.33
Water	147342	429685	631461	0.79780	-4.59932	1.09
2-propanol	147052	429540	631007	0.24834	-4.48307	1.35
4-methyl-2-pentanol	146767	428728	630518	-1.14178	-3.70885	1.00
Ethylene glycol	145424	426288	627401	-4.19029	-4.77831	1.02

From the results shown in **Table 2-5**, one can find that the value of *C* obtained in different liquids may have different signs, which contradict Equation (2-7). Considering this contradiction and the inconsistency in the surface roughness obtained using Equation (2-7), it is highly possible that the model used to simulate the influence of the viscous media on the resonance frequency has to be modified. It seems that it is true that the influence of a viscous media on the resonance frequency is linearly dependent on the square root of the intrinsic resonance frequency, while the contribution of the viscosity

and density of the liquid can be different. That is, the viscous media would result in a change in the resonance frequency (Δf_n) as

$$\Delta f_n = G(\eta, \rho_l, MSP) \cdot \sqrt{f_n} \qquad (2\text{-}8)$$

where the constant G is a function of both the liquid's properties (i.e. ρ and η_l) and the properties of the MSP (i.e. the materials properties and geometry). Further study on this is needed.

2.4.5 Effect of liquid on *Q* value

By rearranging Equation (1-16) to (2-9), it is found that $1/Q_n$ value is a linear function of $\sqrt{\rho_l \eta}$.

$$\frac{1}{Q_{n,l}} = J \cdot (\eta \rho_l)^{1/2} + \frac{1}{Q_n} \qquad (2\text{-}9)$$

$$J = \frac{1}{\rho_s d \sqrt{\pi f_n}} \qquad (2\text{-}10)$$

where Q_n and $Q_{n,l}$ are the Q value of nth harmonic mode of an MSP in air and liquid, respectively. The ρ_s, d and f_n are the same as above.

Figures 2-13(a) and 2-13(b) show the experimental results about the $1/Q$ as the function of $\sqrt{\rho_l \eta}$ for two MSPs in different media (MSP-1: 15.52 mm x 3.78 mm x 30 µm and MSP-2: 15.58 mm x 3.76 mm x 30 µm) operated using first harmonic orders. For the same MSPs, the results obtained from the MSPs operated under 3rd and 5th harmonic modes are shown in **Figures 2-13(c)** and **2-13(d)**.

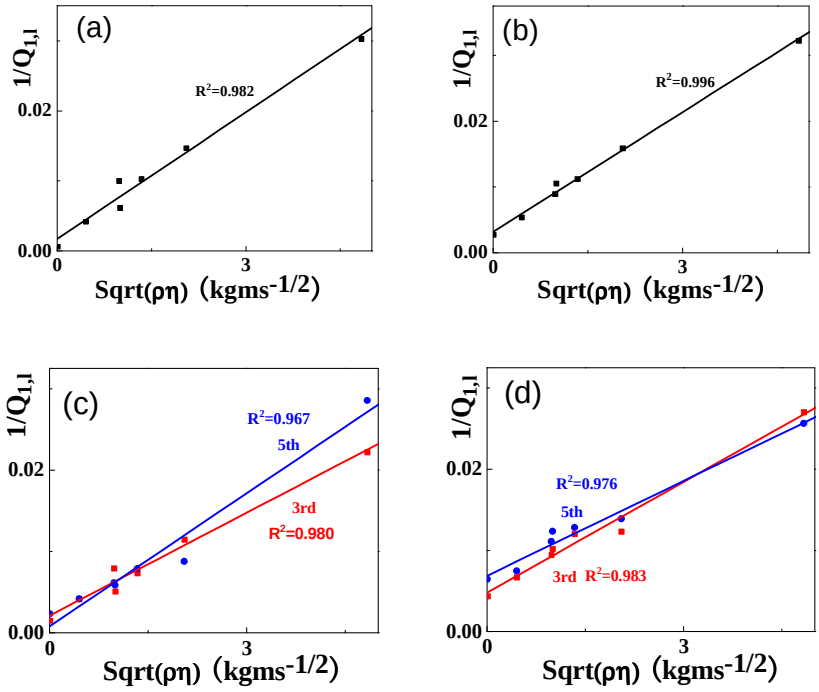

Figure 2-13. The $1/Q$ *vs.* $\sqrt{\rho_l \eta}$ for two similar sizes of MSPs (MSP-1: 15.52mm x 3.78 mm x 30μm and MSP-2: 15.58 mm x 3.76 mm x 30 μm) in different liquids: (a) MSP-1 at 1st harmonic mode, (b) MSP-2 at 1st harmonic mode, (c) MSP-1 at 3rd and 5th modes, (d) MSP-2 at 3rd and 5th modes.

When the results shown in **Figure 2-13** are fitted using Equation (2-9), the values of the *J* are obtained, as shown in **Table 2-7**. The values of the *J* can also be calculated using Equation (2-10).

Table 2-7. The *J* values determined from experimental results through fitting using Equation (2-9) and directly calculated from Equation (2-10).

Harmonic mode	J ($kg^{-1}m^3Hz^{1/2}$) x 10^{-3} **(fitted)**		J ($kg^{-1}m^3Hz^{1/2}$) x 10^{-3} **(calculated)**	
	MSP-1	MSP-2	MSP-1	MSP-2
1st	6.06	6.02	6.19	6.22
3rd	4.22	4.54	3.63	3.68
5th	5.66	3.90	2.99	3.02

To further study the influence of the media on the *Q* value, the MSPs with different sizes were tested. Some of the experimental results are shown in **Figure 2-14**, where the

$1/Q_{1,l}$ is plotted as the function of $\sqrt{\rho_l \eta}$ for the MSPs at 1st harmonic mode.

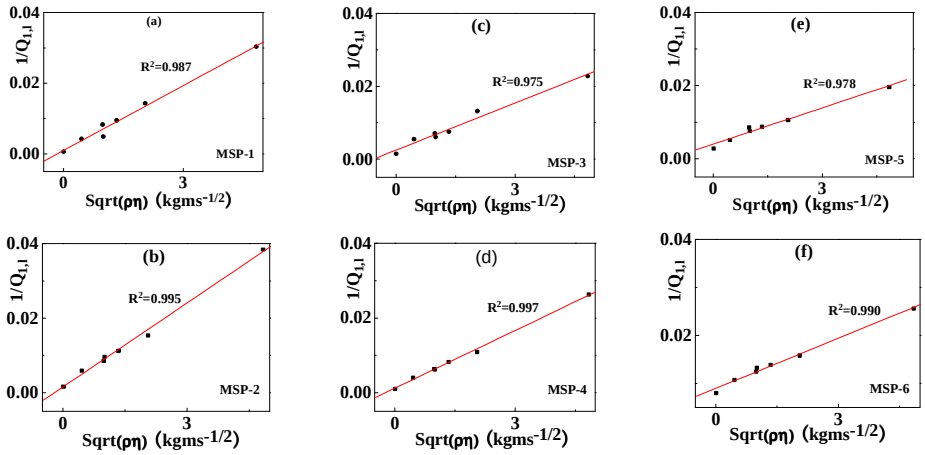

Figure 2-14. $\Delta f_n / \rho_l$ *vs.* $\sqrt{\eta / \rho_l}$ for MSPs with the same width but different lengths in different liquids, where the MSPs were operated at first harmonic mode. (a) MSP-1' (15.40 mm x 1.00 mm x 30 µm), (b) MSP-2' (15.65 mm x 1.00 mm x 30 µm), (c) MSP-3 (7.98 mm x 1.00 mm x 30 µm), (d) MSP-4 (8.18 mm x 1.00 mm x 30 µm), (e) MSP-5 (4.00 mm x 1.00 mm x 30 µm), and (f) MSP-6 (4.07 mm x 1.00 mm x 30 µm).

When the results shown in **Figure 2-14** are fitted using Equation (2-9), the values of *J* are obtained, as shown in **Table 2-8**, column labeled fitted. The value of the *J* is also calculated using Equation (2-10) as shown in **Table 2-8**, column labeled calculated.

Table 2-8. The *J* values determined from experimental results through fitting using Equation (2-9) and directly calculated from Equation (2-10) for MSPs at 1st harmonic mode.

MSP		J ($kg^{-1}m^3Hz^{1/2}$) x 10^{-3} (fitted)	J ($kg^{-1}m^3Hz^{1/2}$) x 10^{-3} (calculated)
MSPs used above	15.52mm x 3.78mm x 30 μm	6.06	6.19
	15.58mm x 3.76mm x 30 μm	6.02	6.22
15.40 mm x 1.00 mm x 30 μm		6.12	6.18
15.65 mm x 1.00 mm x 30 μm		7.51	6.22
7.98 mm x 1.00 mm x 30 μm		4.30	4.48
8.18 mm x1.00 mm x 30 μm		5.15	4.52
4.00 mm x 1.00 mm x 30 μm		3.30	3.18
4.07 mm x 1.00 mm x 30 μm		3.48	3.23

By comparing the results shown in **Tables 2-7** and **2-8**, it seems that Equation (2-9) can be used to present the media influence on the *Q* value well only for the first harmonic mode. For the higher orders of harmonic mode, the relationship is more complicated.

2.5 Conclusions

The resonance behavior including the resonance frequency and the *Q* value of the MSP was systemically examined. First of all, based on the results obtained from the MSP in air, it was found that the apparent acoustic velocity is dependent on the length and the *L/W* ratio rather than a constant. For example, it increases with increasing length for the MSP with the same *L/W* ratio, while it increases with increasing *L/W* for the MSPs with the same length. It is believed that the change in the apparent "acoustic velocity" with the length is related to the frequency dependence of the mechanical properties of the material due to the relative high mechanical loss. Regarding the change in the apparent "acoustic velocity" with the *L/W* ratio, it is believed that the acoustic velocity is dependent on Poisson's ratio with an order that may change continuously. Although the viscous media has a very complicated influence on resonance behavior, it has been experimentally found

that the resonance frequency of the MSP in any one of tested media is still dependent on the invasive length of the MSP with an apparent “acoustic velocity” changes with the length and *L/W* ratio following the same trend as in air.

The methodology to determine the surface roughness of the MSP was explored. It was found that the currently used method, which is dependent on the resonance frequency of an MSP in many different media, has some drawbacks due to the complexity of the influence of the liquid media. A new method, which is based on the resonance frequency of an MSP in one liquid but operated at different harmonic modes, was introduced. A relatively consistent result was obtained, indicating the advantages of this new method in the determination of the sensor surface roughness.

References

1. “Agilent 4395A Network/Spectrum/Impedance Analyzer Operation Manual,” Agilent Technologies.
2. S.Q. Li, Development of Novel Acoustic Wave Biosensor Platforms Based on Magnetostriction and Fabrication of Magnetostrictive Nanowires, Dissertation, Auburn University, 2007.
3. “http://www.engineeringtoolbox.com/air-properties-d_156.html.”
4. “http://www.scenta.co.uk/tcaep/nonxml/science/constant/details/Air,%20Viscosity%20of%20(20%C2%B0C).html.”
5. C. Marsden, S. Mann, Solvents guide, Interscience, 1963.
6. S.K. George, Density, Thermal Expansivity, and Compressibility of Liquid Water from 0 to 150C, Journal of Chemical and Engineering Data, 20 (1975) 97-105.

7. S.Q. Li and Z.-Y. Cheng, Nonuniform mass detection using magnetostrictive biosensors operating under multiple harmonic resonance modes, Journal of Applied Physics 107 (2010) 114514/1-114514/6.
8. M.K. Jain, and C.A. Grimes, Effect of surface roughness on liquid property measurments using mechanically oscillating sensors, Sensors and Actuators A, 100 2002, 63-69.

CHAPTER 3

PHAGE/ANTIBODY IMMOBILIZED MAGNETOSTRICTIVE BIOSENSOR FOR BACTERIAL DETECTION

3.1 Introduction

As a biosensor platform, an MSP exhibits many unique advantages, such as being wireless, high sensitivity, easy operation, and working well in liquid. MSP based biosensors for the detection of different pathogens such as *S. typhimurium* and *B. anthrics spores* have been developed and studied [1-4]. However, due to the small size and the truly freestanding nature, the immobilization of the sensing element onto the surface of the MSP is a challenge and the physical adsorption is usually used to immobilize the sensing element onto the MSP surface to form a biosensor. For pathogen detection, both phages and antibodies are available as sensing elements. It is very fortunate that phages can be easily immobilized onto an MSP surface by physical adsorption. Although antibodies can also be immobilized onto an MSP surface by physical adsorption, the resulting binding force of antibodies onto the MSP surface is weak. Furthermore, it is well known that an antibody binds the target species at specific location(s). Therefore, the orientation of the immobilized antibody is very critical to the performance of the MSP-based biosensor. Unfortunately, the physical adsorption results in an immobilization of antibody in a random orientation. More importantly, as a new alternative to the antibody, the availability of the phage is very limited. Therefore, it is of great interest to find a way to immobilize antibodies onto the MSP surface with strong binding and good orientation.

In this chapter, the development of antibody-immobilized MSP biosensors is presented. MSP based biosensors for the detection of *E. coli*, *S. aureus*, and *L. monocytogenes* are developed and characterized. As a comparison, the phage specific to *S. typhimurium* is also studied. To prevent or reduce nonspecific binding, the employment of the blocking agent is also studied.

3.2 MSP preparation

A commercially available magnetostrictive alloy, the Metglas™ 2826MB ribbon, was used to fabricate the MSPs. First, a sheet of Metglas™ 2826MB thin film was polished down to 15 μm in thickness using 2400# polish paper. Then, the polished thin film was cut into rectangular MSPs in the size of 1.0 mm x 0.3 mm using a micro-dicing saw Model 1110 (From Micro Automation). After being diced, these MSPs were cleaned in methanol using an ultrasonic cleaner (Cole Parmer 8891) for 30 minutes and then dried by nitrogen gas. Then, a chromium (Cr) layer with a thickness of 100 nm and a gold (Au) layer in thickness of 125 nm were serially deposited on the both sides of the particles by using the Denton sputtering system. The chromium layer was used to enhance the adhesion force between the gold layer and the particle, and the gold layer was used to promote the immobilization of the sensing elements and also to protect the MSPs from corrosion. Finally, these MSPs were ready for phage/antibody immobilization.

3.3 Phage and antibody immobilization

To form a biosensor, a sensing element has to be immobilized onto the surface of an MSP. Both phages and antibodies were used in this study to detect pathogenic bacteria. Physical adsorption was utilized to immobilize the phage, while antibodies were immobilized in a more controllable manner.

3.3.1 Phage immobilization

A phage suspended in water with a population of 1.05 x 10^{12} virions/ml was used for the immobilization. The phage was immobilized using physical adsorption. That is, one Au/Cr coated MSP was immersed into 200µl phage culture (in TBS buffer) for 1 hour. During the immobilization, the container of the MSP and phage solution was continuously rotated using Labquake Tube Shaker/Rotators (from Barnstead/Thermolyne Corporation). Then, the phage immobilized MSPs were taken out and rinsed with sterile distilled water for 3 times. Finally, these sensors were ready for detection.

3.3.2 Antibody immobilization

The antibody was immobilized using covalent binding. To form covalent bonds between the MSP and the antibody, the antibody was modified first to form a –SH group onto the antibody using a Traut's Reagent (2-iminothiolane • HCl, Pierce, Product Number 26101) as shown in **Figure 3-1 (top)**. The introduced sulfhydryl group can form covalent bond with gold thin film on the MSP through a process similar with the formation of a self-assembling monolayer (SMA) [5] as shown in **Figure 3-1(bottom)**.

During the experiments, the antibodies were first diluted using phosphate buffered saline (PBS) buffer with 3mM ethylenediaminetetraacetic acid (EDTA) into a 0.01M, pH=8.0 suspension. Secondly, a 20-fold molar excess of 2-iminothiolane prepared in ultra-pure water was added into the antibody suspension prepared in the first step and then incubated for 1 hour at room temperature. Thirdly, the free 2-iminothiolane and the 2-iminothiolane attached/bond with antibody were separated immediately using a centrifuge (Centricon YM-30) and the suspension of the antibody was concentrated to 50 µg/ml. To determine/monitor the results of antibody modification, Ellman's reagent ((5,

5’-Dithio-bis-(2-nitrobenzoic acid, Pierce, 22582) was added into the antibody suspension to visualize the introduced sulfhydryl groups in the antibody suspension [6], which was quantified using a optical spectrometer (UV/VIS UV-1650PC Spectrophotometer). The 2-iminothiolane modified antibody was immobilized onto the gold coated MSP through the thiolation by adding MSP immediately into the modified-antibody suspension for 2 hours at room temperature. Finally, the MSP sensors were rinsed by DI water 3 times and were then ready for detection.

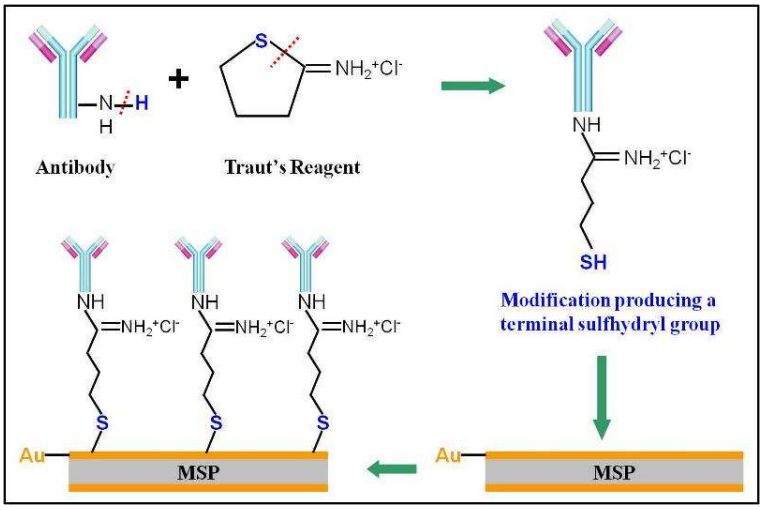

Figure 3-1. Schematic illustration of modification of antibodies (top) and the immobilization of the modified antibody onto gold coated MSP (bottom) [6].

3.4 Blocking agents

Non-specific binding (NSB) on the sensor surface rather than the capture of target species is one of the most important issues in biological detection because NSB would lower the specificity and reliability of a biosensor. In reality, there is always a concern about NSB since in the real sample/analyte a very complete biological matrix (or background) may exist. A blocking agent is usually utilized to eliminate or reduce the NSB. The blocking agents occupy the surface that was not covered by the sensing

element, which results in the vacant sites of the sensor surface becoming saturated so that NSB will not occur. Since different types of bacteria have different ability of NSB and each analyte has a different background, there is a concern about whether a blocking agent is needed. If needed, which blocking agent would be the best for each biosensor? There are many blocking agents available, such as casein, bovine serum albumin (BSA), gelatin, nonfat dry milk, and tween 20 [6] among which, casein and BSA have been intensively used in ELISA and other experiments for preventing NSB of bacteria/antibodies due to the advantages of stability, inertness to many biochemical reactions, and low cost [7-9]. In addition, casein and BSA both have low molecular weight which theoretically would have a greater opportunity to fill in small area vacancy sites between the phages/antibodies. Therefore, in this research, both casein and BSA as blocking agents were studied for the purpose of preventing NSB of bacterial cells on the MSP-based biosensor surface. To form a blocking agent suspension, the casein and BSA powder was diluted in phosphate buffered saline (PBS) buffer to 5%wt and 3%wt, respectively.

3.5 Preparation of bacterial culture

The bacterial cultures used in the experiments were prepared in either the Department of Microbiological Sciences or the Department of Poultry Science at Auburn University. First, a bacterial suspension with an initial population of 5×10^8 cfu/ml was prepared. Then, the suspension was serially diluted by using sterile distilled water to form the bacteria suspension with different populations ranging from 5×10^1 to 5×10^8 cfu/ml with a dilution factor of 10 for each dilution. The bacterial suspensions were used in the same day they were prepared.

3.6 Experimental setup

The experimental setup for characterizing the response of an MSP biosensor is shown in **Figure 3-2**. Two reservoirs were used: one was for analyte and the other one was for waste. The analyte (bacterial suspension here) was forced to flow with a constant low rate through a tube in which the MSP biosensor was placed. The coil was wound outside of the tube for the measurement, and a magnet is placed outside of the tube to provide a dc magnetic field. The measurement was done using a network analyzer (HP 87511) which was controlled using a personal computer (PC).

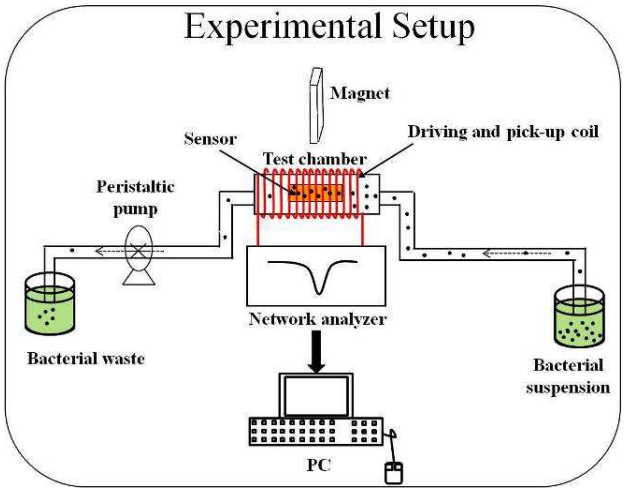

Figure 3-2. Schematic configuration of the experimental setup for the characterization of the response of MSP biosensor in liquid analyte.

Before detection, the phage/antibody immobilized sensor was first put into the test chamber (tube) and then the peristaltic pump was used to have a flow rate of 30 µl/min in the tube. During the measurement, the sterile distilled water was used first to flow through the tube until the sensor reached its stable response. The response (i.e. resonance frequency f_0) of the sensor in water was used as a background as shown **Figure 3-3(b)**. Then, the response of the sensor in each bacterial suspension was tested by forcing the

analyte (bacteria suspension) to flow through the test chamber. The sequence of the bacteria culture during the experiment is from low to high population (i.e. from 5 x 10^1 cfu/ml, 5 x 10^2 cfu/ml … to 5 x 10^8 cfu/ml) as shown in **Figure 3-3(a)**. The test duration for each population was 20 minutes. That is, for each bacterial suspension, only 0.6 ml of the analyte was used.

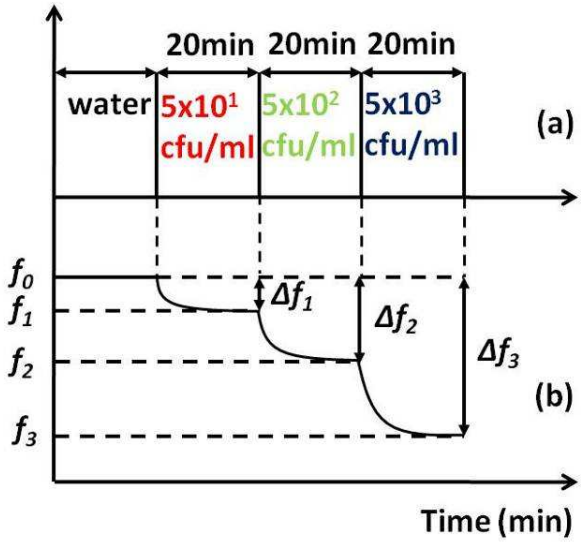

Figure 3-3. Scheme of (a) The sequences of the analytes through the test chamber (tube), (b) the typical sensor response.

The resonance frequency of the sensor was continuously monitored/measured. The results were recorded during the whole detection period with an interval of 30 seconds. Therefore, the experimental result was the change in the resonance frequency of the MSP sensor as the function of time as shown in **Figure 3-3(b).** As shown in **Figure 3-3(b)**, when the bacterial population was changed, the resonance frequency of the sensor changes immediately and reached its saturated state eventually. The initial change in the resonance frequency with the time reflects the response time of the sensor, while the saturated resonance frequency presents the response of the sensor in a certain analyte.

After the final test using analyte with the highest population, the sensor was rinsed

using deionized (DI) water 3 times and then dried in air. The sensor was then used to verify that the change in the resonance frequency of the sensor was due to the binding of target species, using scanning electron microscopy (SEM) to directly observe the bacterial cells bonding on the sensor surface.

3.7 SEM observation

SEM was used in this study to verify the binding of target species onto the sensor. In the experiments, the sensor dried in air was then exposed to osmium tetroxide (OsO_4) vapor at room temperature for one hour. Osmium tetroxide is used to keep the shape of bacterial cells in high vacuum. The SEM observation was performed on a field emission scanning electron microscope JEOL 7000 F at 20 keV.

3.8 Hill plot and kinetics of binding

Based on the experimental results (as schematically shown in **Figure 3-3(b)**), the so-called "dose response" of the sensor was obtained as shown in **Figure 3-4(a)**, where the symbols of the stable/saturated resonance frequency of the sensor in each analyte (i.e. each population of the culture) are plotted against the population of the bacteria. The dose response was then fitted using a sigmoid function as shown in **Figure 3-4(a)**, where the solid line represents the fitting results. The sigmoid function is expressed as:

$$\Delta f = \Delta f_{\max} + \frac{\Delta f_S - \Delta f_{\max}}{1 + \left(\frac{C}{C_0} \right)^{\alpha}} \tag{3-1}$$

where C is the population of the analyte (i.e. bacteria culture here) and Δf (= $f - f_0$), where f and f_0 are the stable/saturated resonance frequency of the sensor in the analyte with population C and the water, respectively. C_0 is a fitting constant that represents the analyte population which is the infection point of the dose response curve. α (>0) is a

fitting constant. Δf_{max} and Δf_S are two fitting constants: Δf_S is the value of Δf when the C is zero and Δf_{max} is the saturated value of Δf or the value of Δf corresponding to a population of infinite high. Therefore, in this study, Δf_S is zero. Here, we introduce a new parameter Y as:

$$Y = \frac{\Delta f}{\Delta f_{\max}} \qquad (3\text{-}2)$$

Then

$$\frac{Y}{1-Y} = \frac{\Delta f}{\Delta f_{\max} - \Delta f} = \left(\frac{C}{C_0}\right)^{\alpha} \qquad \text{or} \qquad \log\left(\frac{Y}{1-Y}\right) = \alpha \log\left(\frac{C}{C_0}\right) \qquad (3\text{-}3)$$

Based on the fitting constant Δf_{max}, the dose response curve can be converted into a so-called Hill plot as shown in **Figure 3-4(b)**, where log[*Y/(1-Y)*] is plotted as the log population.

Equation (3-3) indicates that the Hill plot is a straight line with a slope of α, which is an important parameter (i.e. Hill coefficient n).

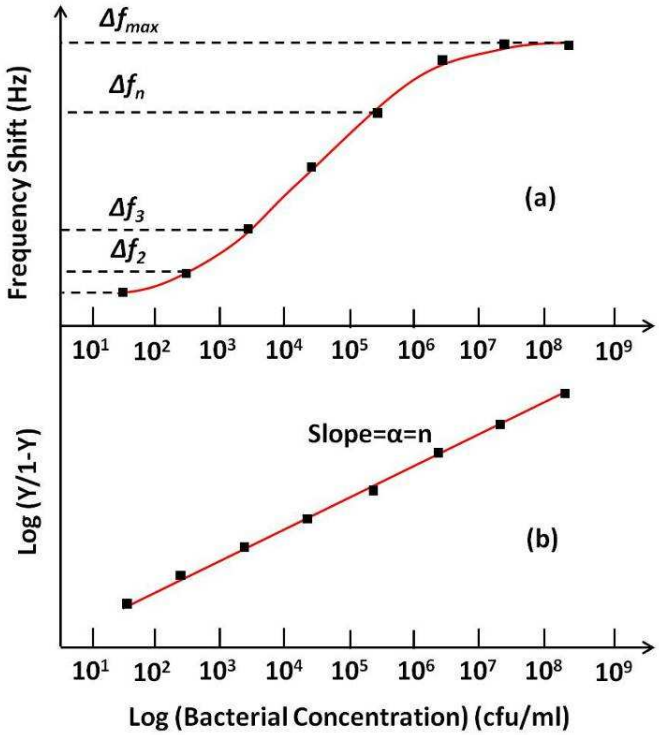

Figure 3-4. (a) Stable/saturated shift in the resonance frequency shift of an MSP sensor in relation to the population of the analyte. (b) A typical Hill plot obtained from the data shown in Figure (a).

In a biosensor, the response originates from the reaction between the sensing element and the ligands (target species). This reaction can be treated as a normal chemical reaction as [10]:

$$n[L]+[A]\underset{K_d}{\overset{K_a}{\rightleftharpoons}}[AL_n] \qquad (3\text{-}4)$$

where A and L are the (macro)molecule of the sensing element (i.e. protein such as phage or antibody in this study) and the ligand (the bacterial cell in this study), respectively. This reaction is chemically characterized using two reaction constants: K_a and K_d ($=1/K_a$). A higher value of K_a indicates a higher binding ability of the sensing element. In biochemistry, K_a and K_d are also named as the association binding constant and the dissociation binding constant, respectively. The n is the number of ligand molecules

bound onto a sensing element molecule (i.e. a single antibody or phage). Therefore, the value of *n* is an important parameter for the biochemical reaction since it presents the affinity of the sensing element. The K_a can be defined as [11]:

$$K_a = \frac{[AL_n]}{[A]\cdot[L]^n} \tag{3-4'}$$

If the nonspecific binding is ignored, the total number C_A (for a sensor the C_A is a constant) of the binding sites of the sensing elements on the sensor can be written as

$$C_A = [A] + [AL_n] \tag{3-5}$$

where the first term presents the free binding site of the sensing element and the second term presents the binding site of the sensing element bound with the ligand. By substituting Equation (3-5) into (3-4'), the fraction (Y', $0 \le Y' \le 1$) of the occupied/bound binding sites of the sensing element of the sensor is obtained as:

$$Y' = \frac{[AL_n]}{C_A} = \frac{K_a[L]^n}{1 + K_a[L]^n} \tag{3-6}$$

Then,

$$\frac{Y'}{1-Y'} = K_a[L]^n \quad \text{or} \quad \log\left(\frac{Y'}{1-Y'}\right) = \log K_a + n\log[L] \tag{3-7}$$

This equation provides an easy way to determine the value of *n* for a biochemical reaction occurring on the sensor surface. The value of *n* reflects the nature of the sensing element. The *n* is named as Hill coefficient, which describes the cooperativity of the sensing element.

Assuming that all the target species (i.e. target bacterial cell) are the same in terms of mass, the population of the phage/antibody–bacteria reaction products (i.e. $[AL_n]$) is

proportional to the change in the mass load (Δm) of the sensor. Based on the principle of the sensor, the change in the resonance frequency of the sensor is proportional to the mass load (Δm) as expressed by Equation (1-10). Therefore, the change in the resonance frequency of the sensor is proportional to the population of the product produced by the reaction between analyte and sensing element. That is, $\Delta f \propto [AL_n]$, which can be written as

$$\Delta f = K'\left[AB_n\right] = K' \cdot C_A \cdot Y' \qquad (3\text{-}9)$$

where *K'* is a constant and in second step Equation (3-5) was used. By the definition of the *Y'*, $\Delta f = 0$ when $Y' = 0$ (this corresponds to no binding site being occupied), and $\Delta f = \Delta f_{max}$ when $Y' = 1$ (this corresponds to all binding sites being bound with ligand). Therefore, Equation (3-9) can be written as

$$\Delta f = \Delta f_{\max} \cdot Y' \qquad \text{or} \qquad \frac{\Delta f}{\Delta f_{\max}} = Y' \qquad (3\text{-}10)$$

Therefore, the *Y* defined by Equation (3-2) is the same as *Y'* defined here. That is, the slop of the Hill plot shown in **Figure 3-4(b)** is the *n* in the chemical reaction in Equation (3-4).

In Equation (3-4), a value of *n* less than one means each ligand (bacterial cell in this study) binding with *1/n* sensing molecules (i.e. *1/n* antibodies).

3.9 Results and discussion

3.9.1 Detection of *S. typhimurium*

In this part of the research, the sensing element is phage E2, which has been developed recently at Auburn University [13], and the *S. typhimurium* culture used to test the sensor performance were prepared/provided by the Department of Microbiological

Sciences at Auburn University.

A typical set of experimental results for the MSP sensor is shown in **Figure 3-5**, where the recorded resonance frequency of the sensor during experiment is plotted against time. As mentioned in section 3.6, the population of culture changed from low to high as indicated in the figure. First of all, it was observed from the results that the sensor has a fast response. For example, in the culture the sensor reaches its saturated resonance frequency of a few minutes. Secondly, it is found that the sensor had a high sensitivity. For example, when exposed into the culture with a population of only 50 cfu/ml, the sensor exhibited a clear change in its resonance frequency. This indicates that the sensor had a detection limit better than 10^2 cfu/ml. The total change in the resonance frequency reached 6,320 Hz.

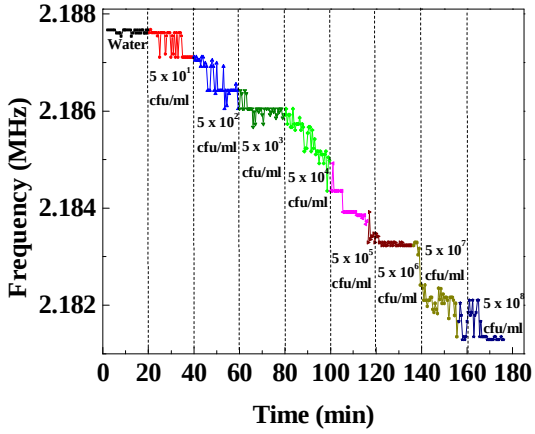

Figure 3-5. A typical dynamic dose response of a phage E2 immobilized magnetostrictive biosensor in the size of 1.0 mm x 0.3 mm x 15 µm to increasing population of *S. typhimurium*.

The dose response curve of the sensors is given in **Figure 3-6**, where the results from a reference sensor are also presented. The reference sensor was exactly the same as the sensor but without being coated with the E2 phage. Clearly, the response (i.e. the

change in the resonance frequency) of the sensor was much higher than that observed from the reference sensor. As can be seen from the results shown in **Figure 3-6**, a linear dose response was observed for the sensor in a population range from 5 x 10^3 cfu/ ml to 5 x 10^5 cfu ml. The sensitivity (the slope of the linear range on the dose response curve) of the sensor in suspensions was 730 Hz decade^{-1} (R^2=0.99972).

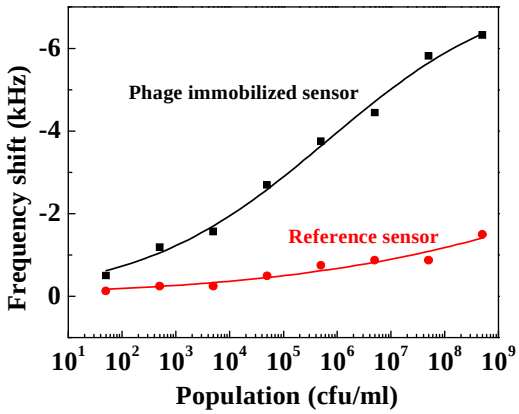

Figure 3-6. Resonance frequency shifts (Hz) change with the increasing population of the *S. typhimurium*.

The Hill plot for the sensor is shown in **Figure 3-7**. A Hill coefficient of n=0.25783 was obtained. This indicates that one *S. typhimurium* cell was bound onto the sensor through about 4 binding sites.

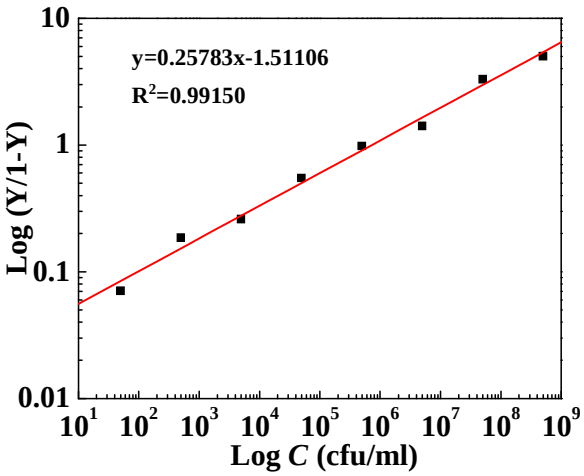

Figure 3-7. Hill plot from the dose response curve.

3.9.2 Detection of *E. coli*

In this part of the research, the sensing element was polyclonal antibody anti-*E. coli* rabbit IgG which was obtained from GeneTex, Inc (GTX13626). The *E. coli* cultures were prepared at the Department of Biological Sciences of Auburn University.

A typical set of raw experimental results for a MSP sensor is shown in **Figure 3-8**, where the recorded resonance frequency of the sensor during experiment is plotted against time. Again, it can be observed from the results that the sensor had a fast response. It was also found that the sensor had a detection limit better than 10^2 cfu/ml. The total change in the resonance frequency reached 4,380Hz.

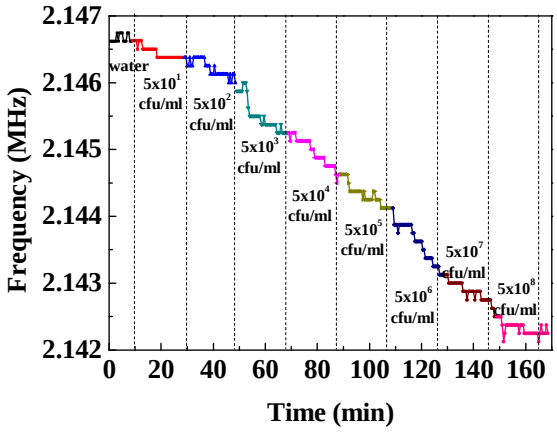

Figure 3-8. The dynamic dose response of an antibody immobilized sensor to the increasing population of *E. coli*.

The dose response curve of the sensors is given in **Figure 3-9**, where the results from a reference sensor are also presented. The reference sensor was exactly the same as the sensor but without coated with the anti-*E. Coli* antibodies. Clearly, the response of the sensor was much higher than that observed from the reference sensor. As can be seen in the results shown in **Figure 3-8**, a linear dose response was observed for the sensor in a population range from 5 x 10^2 cfu/ml to 5 x 10^7 cfu/ml. The sensitivity of the sensor in suspensions was 700 Hz decade^{-1} (R^2=0.99339).

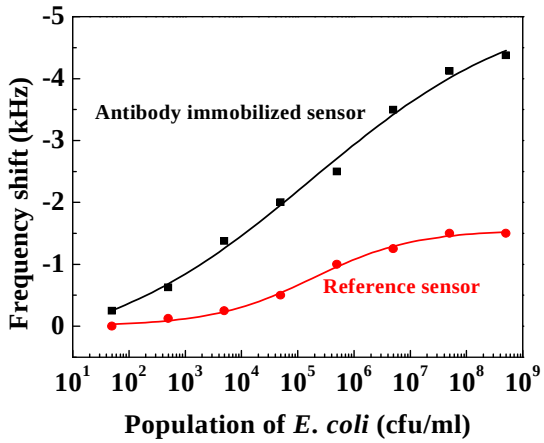

Figure 3-9. Resonance frequency shifts (Hz) change with the increasing population of the *E. coli* suspensions (cfu/ml).

The Hill plot for the sensor is shown in **Figure 3-10**. A Hill coefficient of n=0.27831 was obtained. This indicates that one *E. coli* cell was bound onto the sensor through about 4 binding sites.

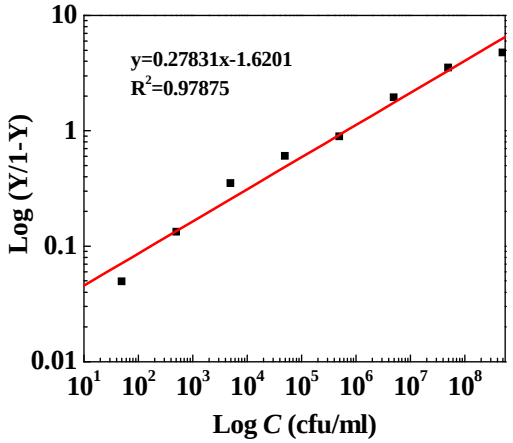

Figure 3-10. Hill plot from the dose response curve.

3.9.3 Detection of *S. aureus*

In this part of the research, the sensing element was polyclonal antibody (Pbs) anti-*S. aureus* rabbit IgG which was obtained from the 3M Corporation. The *S. aureus* culture

(5×10^8 cfu/ml) was obtained from the Department of Poultry Science at Auburn University.

A typical set of raw experimental results for a MSP sensor is shown in **Figure 3-11**, where the recorded resonance frequency of the sensor during experiment is plotted against time. Again, it was observed from the results that the sensor had a fast response. It was also found that the sensor had a detection limit better than 10^2 cfu/ml. The total change in the resonance frequency reached 4,630Hz.

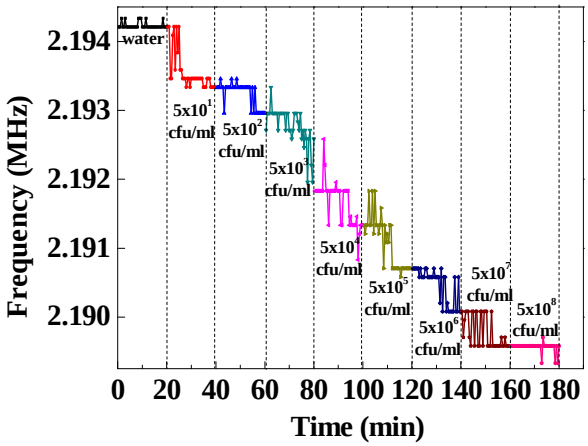

Figure 3-11. The dynamic dose response of an antibody immobilized sensor to the increasing population of *S. aureus*.

The dose response curves of the MSP sensors are given in **Figure 3-12(a)**, where the results from a reference sensor are also presented. The reference sensor is exactly the same as the sensor but without coated with the anti-*S. aureus* antibodies. It was observed that even though the frequency shift of the antibody immobilized sensor was higher than that from the reference sensor at each population, the frequency shift for the reference sensor was also fairly high showing that the non-specific binding of *S.aureus* is a concern. The dose response curves of the MSP sensors are given in **Figure 3-12(b)**, where the result from reference sensor treated with casein is also presented. Clearly, the response of

the reference sensor is much higher than that observed from the casein blocked sensor showing that casein has great blocking efficiency for preventing the nonspecific binding of *S.aureus*.

Based on the results shown in **Figure 3-12**, a linear dose response is observed for the sensor in a population range from 5 x 10^3 cfu/ml to 5 x 10^7 cfu/ml. The sensitivity of the sensor in suspensions is 595 Hz decade^{-1} (R^2=0.99828).

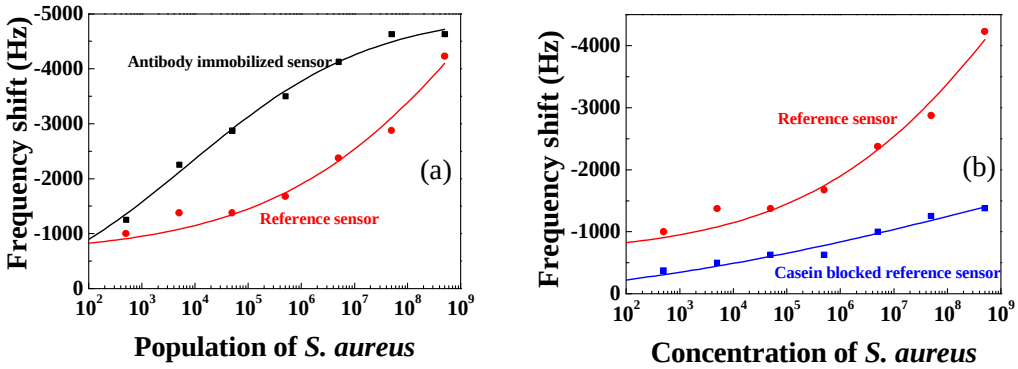

Figure 3-12(a). Resonance frequency shift (Hz) of the sensors with different treatment: (a) the antibody immobilized sensor (in black) and a reference sensor (in red), (b) a reference sensor (in red) and a casein blocked reference sensor (in blue)

The Hill plot for the sensor is shown in **Figure 3-13**. A Hill coefficient of n=0.27136 was obtained. This indicates that one *S. aureus* cell was bound onto the sensor through about 4 binding sites.

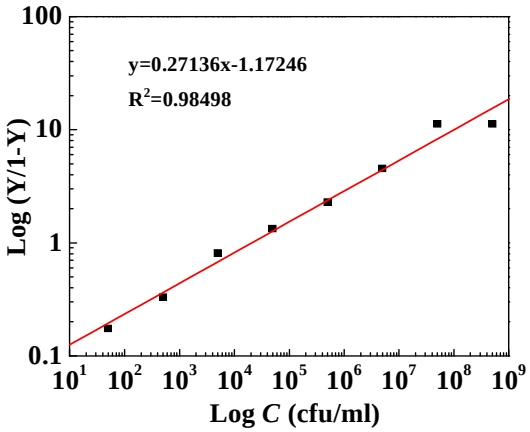

Figure 3-13. Hill plot from the dose response curve.

3.9.4 Detection of *L. Monocytogenes*

The monoclonal antibodies (MAbs) C11E9 used in this research were prepared and provided by Purdue University. The *L. monocentogene* culture (5×10^8 cfu/ml) used in this experiment was obtained from the Department of Biological Sciences and the Department of Poultry Science at Auburn University.

A typical set of raw experimental results for a MSP sensor is shown in **Figure 3-14**, where the recorded resonance frequency of the sensor during experiment is plotted against time. Again, it was observed from the results that the sensor had a fast response. It was also found that the sensor has a detection limit better than 10^2 cfu/ml. The total change in the resonance frequency reached 4,250Hz.

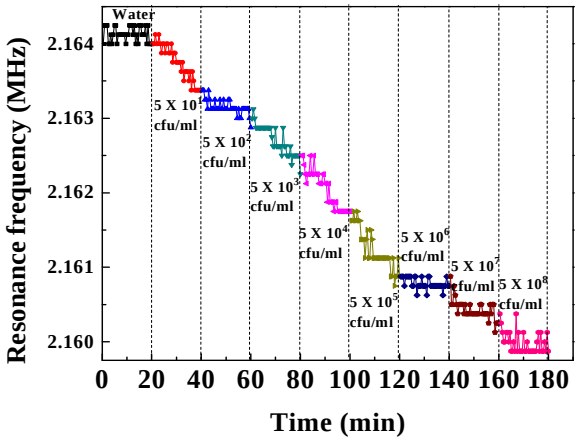

Figure 3-14. A dynamic dose response of an antibody immobilized magnetostrictive sensor to increasing populations.

The dose response curve of the sensors is given in **Figure 3-15**, where the results from a reference sensor are also presented. The reference sensor was exactly the same as the sensor but not immobilized with the antibodies. It was observed that the response of the sensor was higher than that of the reference sensor, but the difference was not very clear, showing the nonspecific binding of *L. monocytogenes* is a big concern. Based on the results shown in **Figure 3-15**, a linear dose response was observed for the sensor in a population range from 5 x 10^2 cfu/ml to 5 x 10^5 cfu/ml. The sensitivity of the sensor in suspensions is 750 Hz decade^{-1} (R^2=0.994).

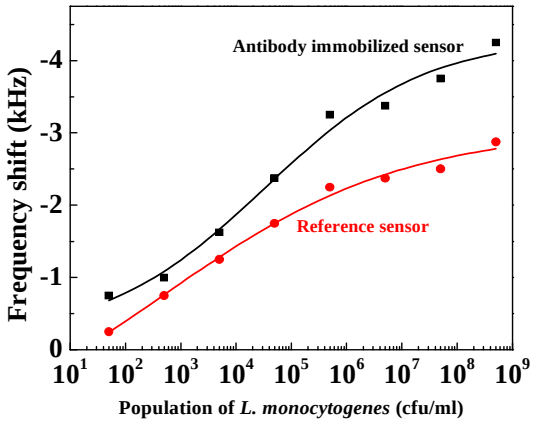

Figure 3-15. Resonance frequency shift (Hz) of the sensors with different treatment: the antibody immobilized sensor (in black) and a reference sensor (in red) change with the increasing population of the *L. monocytogene* suspensions.

The dose response curves of the MSP sensors is given in **Figure 3-16**, where the results from reference sensors treated with different blocking agents are also presented. The reference sensors were sensors without immobilized with antibodies or blocking agents, casein blocked sensors or BSA blocked sensors, respectively. Each point is the average value of three sensors with the same size and under the identical experimental condition. Clearly, the responses of the sensors were much higher than that observed from the reference sensor. It was found that both casein and BSA show a similar good blocking efficiency for preventing the nonspecific binding of *L. monocetogenes*.

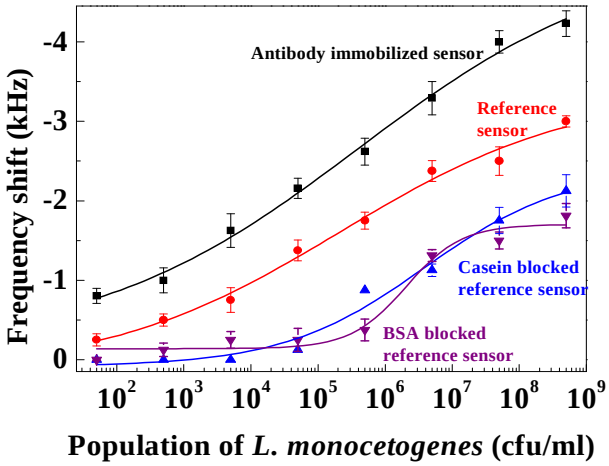

Figure 3-16. The Resonance frequency shift (Hz) of the sensors with different treatment: magnetostrictive biosensors (black square), reference sensors (Red dot), Casein blocked controlled sensors (blue triangle), and BSA blocked controlled sensors (purple reciprocal triangle).

The Hill plot for the sensor is shown in **Figure 3-17**. A Hill coefficient of n=0.2087 wasobtained. This indicates that one *L. monocytogene* cell was bound onto the sensor through about 5 binding sites.

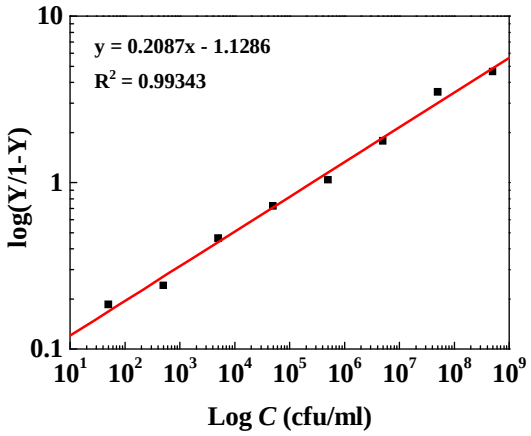

Figure 3-17. Hill plot from the dose response curve showing the kinetics of antibody and bacteria binding.

Typical SEM photomicrographs of binding to the sensors with different surface treatments after exposed to $5x10^8$cfu/ml *L. monocytogene* suspensions are shown in **Figure 3-18**. The differences in number of bacteria on the sensor surface can be clearly observed. The SEM results strongly agree with that of **Figure 3-16**.

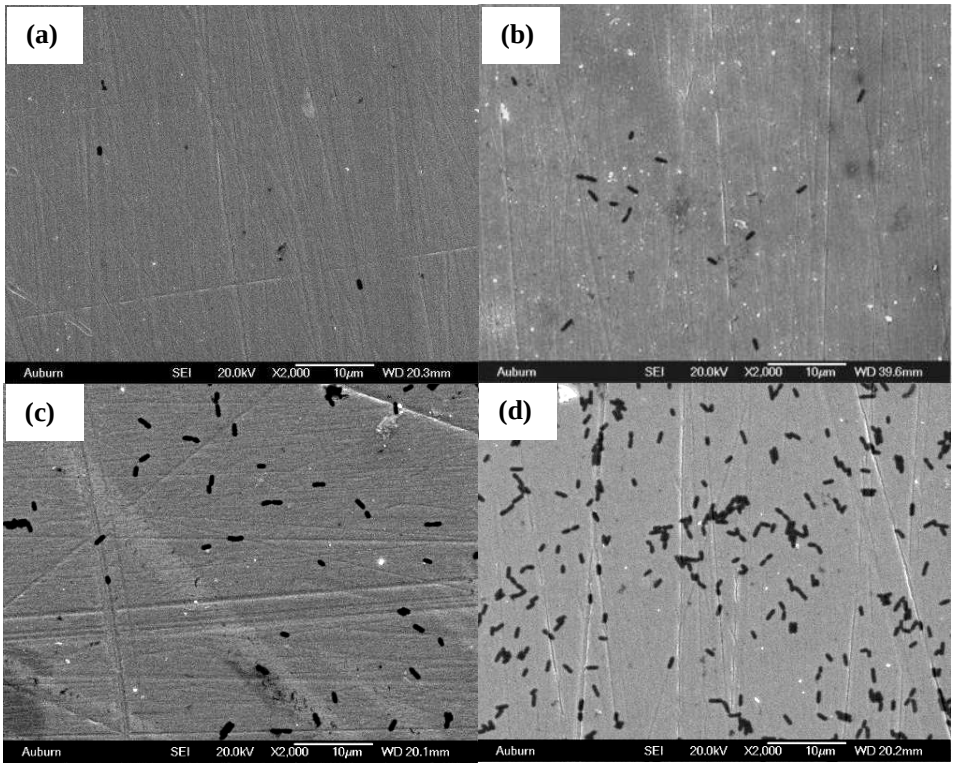

Figure 3-18. SEM images of *L. monocetogenes* on (a) The Casein controlled sensor, (b) The BSA controlled sensor (c) The reference sensor (devoid of antibody immobilization), and (d) The antibody-immobilized magnetostrictive sensor.

3.10 Conclusions

The dynamic dose responses of the biosensor to different bacterial cultures with the populations ranging from 10^1 cfu/ml to 10^8 cfu/ml have been studied. Phage E2 has shown a good specificity to *S. typhimurium*. The dose response results show the detection limit of a biosensor with a size of 1.0 mm × 0.3 mm × 15 μm is better than 10^2 cfu/ml. Casein has good performances on preventing the binding of *S. typhimurium*, *E. coli*, *S.*

aureus, and *L. monocetogenes* on the sensor surfaces. Both casein and BSA have good blocking efficiency on preventing the binding of *L. monocetogenes* on the sensor surfaces. SEM analyses of the sensor surfaces provided a visual verification that the bound of bacteria on the sensor surface was correlated to the measured frequency responses. The results also indicate that the surface modification of antibodies does not affect the function of antibodies.

References

1. R. Guntupalli, J. Hu, R.S. Lakshmanan, T.S. Huang, J.M. Barbaree, B.A. Chin, A magnetoelastic resonance biosensor immobilized with polyclonal antibody for the detection of *Salmonella typhimurium*, Biosensors and Bioelectronics 22 (2007) 1474–1479.
2. R.S. Lakshmanan, R. Guntupalli, J. Hu, V.A. Petrenko, J.M. Barbaree, B.A. Chin, Detection of *Salmonella typhimurium* in fat free milk using a phage immobilized magnetoelastic sensor, Sensors and Actuators B 126 (2007) 544–550.
3. J.H. Wan, M.L. Johnson R. Guntupalli, V.A. Petrenko, B.A. Chin. Detection of *Bacillus anthracis* spores in liquid using phage-based magnetoelastic micro-resonators, Sensors and Actuators B 127 (2007) 559–566.
4. M.L. Johnson, J.H. Wan, S.C. Huang, Z.Y. Cheng, V.A. Petrenko, D.J. Kim, I.H. Chen, J.M. Barbaree, J.W. Hong, B.A. Chin. A wireless biosensor using microfabricated phage-interfaced magnetoelastic particles, Sensors and Actuators A, 144 (2008) 38–47.
5. F. Schreiber, Structure and growth of self-assembling monolayers Progress in Surface Science 65 (2000) 151-256.

6. L.L. Fu, Development of phage/antibody immobilized magnetostrictive biosensors, Dissertation, Auburn University, 2010.

7. M.A. Sentandreu, L. Aubry, F. Toldr, A. Ouali, Blocking agents for ELISA quantification of compounds coming from bovine muscle crude extracts, European food research and Technology 224 (2007) 623–628.

8. T.T. Huang, J. Sturgis, R. Gomez, T. Geng, R. Bashir, A.K. Bhunia, J. P. Robinson, M.R. Ladisch, Composite Surface for Blocking Bacterial Adsorption on Protein Biochips, Biotechnology and Bioengineering 81 (2002) 618-624.

9. J. H. Andrews, I.C. Tommerup, Advances in Botanical Research: Incorporating Advances in Plant Pathology, Academic, 1997.

10. V. Nanduri, S. Balasubramanian, S. Sista, V.J. Vodyanoy, A.L. Simonian, Highly sensitive phage-based biosensor for the detection of β-galactosidase, Analytica Chimica Acta 589 (2007) 166–172.

11. O.H. Lowry, N.J. Rosebrough, A.L. Farr, R.J. Randall, Protein measurement with the Folin phenol reagent, Journal of Biological Chemistry 193 (1951) 265-275.

12. V.A. Petrenko, V.J. Vodyanoy, Phage display for detection of biological threat agents, Journal of Microbiological Methods 53 (2003) 253– 262.

13. V.A. Petrenko, G.P. Smith, X. Gong, T. Quinn, A library of organic landscapes on filamentous phage, Protein Engineering 9 (1996) 797–801.

CHAPTER 4

INTERROGATION DEVICES

4.1 Introduction

Currently, the resonance behaviors of the magnetostrictive/magnetoelastic resonators are characterized using frequency domain technology, in which some commercially available instruments such as a lock-in amplifier [1] and a network analyzer [2-4] are used. These bulky and expensive interrogation systems work excellently as stationary systems. As discussed previously, the MSP sensors are great candidates for an in-field test, for which a stationary system is not suitable. Therefore, portable devices/units for interrogating magnetostrictive/magnetoelastic resonators, such as MSP sensors, are highly desirable. Due to its importance, some research has been done in the development of a portable interrogation device/system for characterizing the resonance behavior of magnetostrictive/magnetoelastic resonators. For example, a portable interrogation device based on a threshold-crossing counting technique [5] and a device based on impedance analysis [6] have been developed and work well at frequencies below 1 MHz since the technologies used in these systems are very sensitive to high frequency noise. However, from the sensor performance point of view, MSPs in a small size are highly desirable since an MSP with a small size exhibits a high sensitivity that is strongly needed for detection technology. It is also known that a small MSP also means a higher f_r. For an MSP with a length of 1 mm, the resonance frequency is already more than 2 MHz as shown in Chapters 2 and 3. Therefore, what is needed is to develop a

portable interrogation device for the characterization of magnetostrictive/magnetoelastic resonators with a resonance frequency of f_r > 1 MHz. In this study, two different principles/technologies were exploited for the development of a portable interrogation unit for the characterization of magnetostrictive/magnetoelastic resonators with high resonance frequency. One was based on the frequency-domain technology, but it used a different principle, in which a reference was used. The other was based on time-domain technology. The reason for exploring both frequency- and time-domain technologies at the same time is that the frequency domain can provide a higher precision in determining f_r but needs more time, while the time domain technology is faster but with a lower precision.

4.2 Equivalent circuit of magnetostrictive/magnetoelastic resonator

As shown in Chapter 2 and 3, a magnetic resonator (i.e. magnetostrictive/ magnetoelastic resonator) is usually placed inside of a coil for measurement. The coil with a vibrating magnetic resonator inside is called the device under test or DUT for short, which can be modeled as a RLC oscillation circuit [7] as shown in **Figure 4-1**, where Z_l, Z_p, and Z_m are the impedance of three different parts and C_s represents the capacitance of the coil alone. Z_l is the impedance of the coil, which can be represented using an equivalent resistor R_l and an equivalent inductor L_s in series as shown in **Figure 4-1(b)**. Z_p is the impedance of the magnetic material in the coil (here the resonator) at static condition, which is represented using an equivalent resistor R_p and an equivalent inductor L_p in series as shown in **Figure 4-1(b)**, while Z_m is the impedance due to the resonance behavior of the magnetic material in the coil (here the resonator), which is represented using an equivalent resistor R_m, an equivalent capacitor C_m, and an equivalent inductor L_p

in series as shown in **Figure 4-1(b)**.

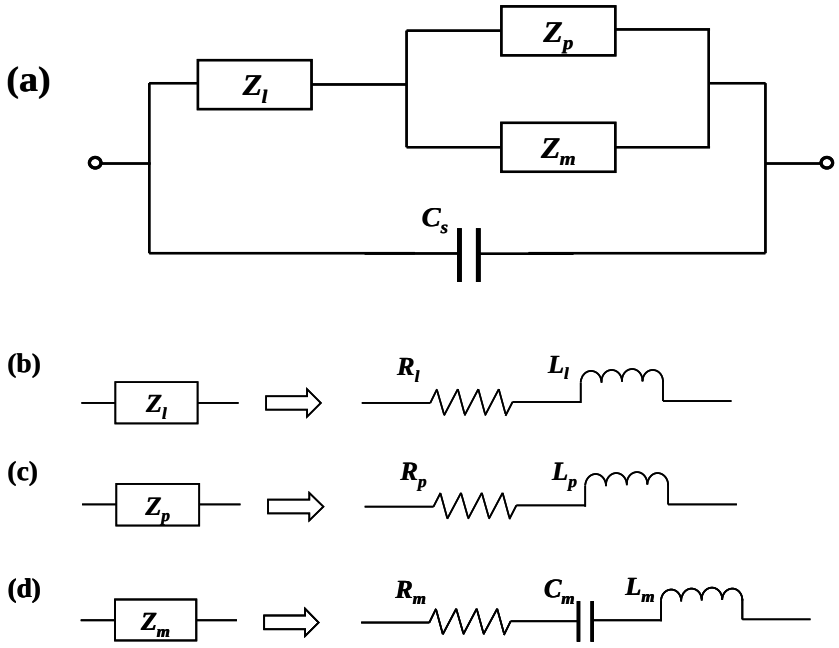

Figure 4-1. The equivalent circuit of the device under test (DUT). (a) the overall equivalent circuit. (b), (c), and (d) show the details of the equivalent circuit for three main parts of the circuit shown in (a), where *R*, *L* and *C* are resistor, inductor, and capacitor, respectively.

Based on the model shown in **Figure 4-1**, the total impedance $Z(\omega)$ of the DUT is:

$$\frac{1}{Z(\omega)} = \frac{1}{\left(Z_l(\omega) + \frac{1}{1/Z_p(\omega) + 1/Z_m(\omega)} \right)} + j\omega C_S \qquad (4\text{-}1)$$

where ω is the angular frequency and j is $\sqrt{-1}$, and

$$Z_l(\omega) = R_l + j\omega L_l \qquad (4\text{-}2')$$

$$Z_p(\omega) = R_p + j\omega L_p \qquad (4\text{-}2'')$$

$$Z_m(\omega) = R_m + j\omega L_m + \frac{1}{j\omega C_m} \qquad (4\text{-}2''')$$

Here, the *R*, *C*, and *L* are the resistance, capacitance, inductance of the resistor, capacitor, and inductor defined above, respectively.

If the impedance of the DUT at different frequencies is determined, the resonance

behavior can be obtained from the frequency dependence of the impedance as shown in **Figure 4-2**, where both amplitude and phase of the impedance are plotted as the function of the frequency.

From the results shown in **Figure 4-2**, three characteristic frequencies are obtained: f_r and f_{ar} in **Figure 4-2(a)** are the resonance frequency and anti-resonance frequency, respectively, while f_0 in **Figure 4-2(b)** is the characteristic frequency. The f_r is the frequency at which the impedance $|Z(\omega)|$ reaches its maximum, while the f_{ar} is the frequency at which the impedance $|Z(\omega)|$ reaches its minimum. The f_0 is a frequency between f_r and f_{ar} at which the phase reaches its peak. The f_0 is related to the resonance frequency and also to other factors, such as the magnetoelastic coupling effect and the mechanical/magnetic properties of the magnetic material. That is, by using the frequency dependence of the impedance, one can determine the resonance frequency as well as the Q value of a magnetic resonator. This is the principle of the technologies currently used to determine the resonance frequency/behavior of a magnetic resonator.

In current measurement technologies, the absolute value of the impedance of the DUT is directly measured as shown in **Figure 4-2**. In the real experiment, an ac current $I(\omega)$ at a frequency (ω) is applied and the voltage $U^*(\omega)$ across the DUT is measured and then the complex impedance $Z^*(\omega)$ at the frequency ω is determined using $Z^*(\omega) = U^*(\omega)/I(\omega)$. During the measurement, the frequency is swept over a range that covers the resonance frequency. In this study, an indirect approach, in which a reference is used, is studied based on frequency domain technology.

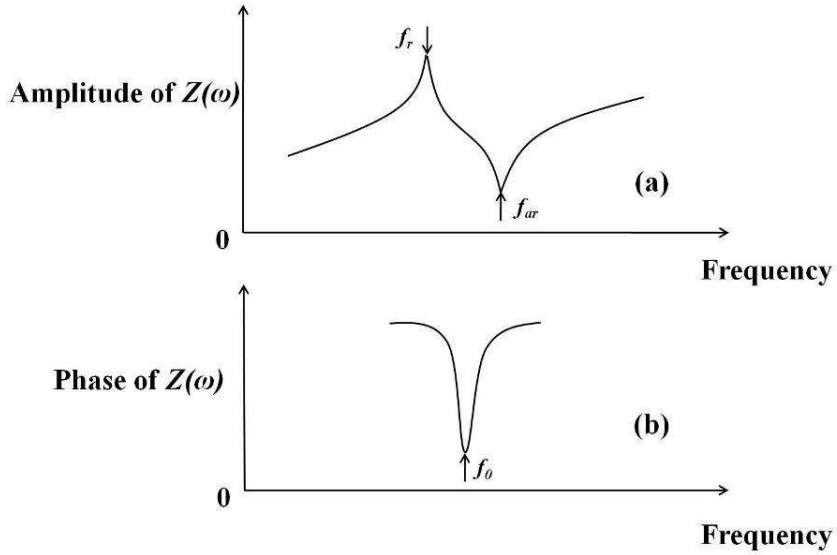

Figure 4-2. Frequency dependence of the impedance $Z(\omega)$ of a magnetic resonator in a coil: (a) amplitude of $Z(\omega)$ and (b) phase of $Z(\omega)$.

Figure 4-3 schematically shows a pulse current when applied through the DUT (as shown in **Figure 4-1)**. That is, the voltage is actually changing with time at a constant frequency with decreasing amplitude. The frequency of this voltage signal is the resonance frequency of the magnetic resonator, while the change in the amplitude of the voltage signal with the time reflects the Q value of the resonator. Therefore, the resonance behavior of a magnetic resonator can also be determined using this time-domain technology.

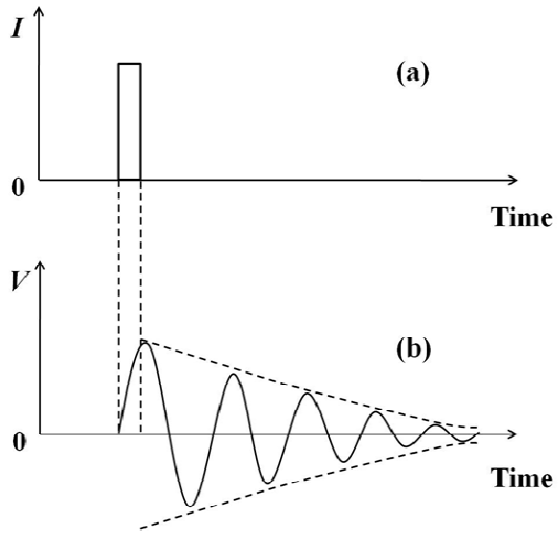

Figure 4-3. Schematic of time domain technique, (a) a pulse current is applied on to a DUT, (b) a voltage across the two ends of the DUT is generated. The voltage changes with the time.

Although both the frequency-domain and time-domain techniques can be used to characterize the resonance behavior of a resonator, each technique has some advantage and drawbacks. For the frequency-domain technique, the frequency has to be swept and the measurement has to be done at each frequency. Therefore, it needs more time for the measurement but provides a high precision in the determination of the characteristic frequency of a resonator. For time-domain technique, the experiment is done with one time measurement and the measured signal is the real resonance signal of a sensor. Therefore, the time-domain technique needs a much shorter time for performing one measurement. Although the precision of the time-domain technique can be enhanced by using multiple pulses, the precision in the determination of the characteristic frequency of a resonator is lower. For magnetostrictive resonators, a dc bias is required when using the frequency-domain technique, but the dc bias can be avoided for the time-domain technique. Therefore, which of these two techniques is better depends on the application. For example, for the MSP sensors, if the change in the characteristic frequency of a

sensor is big, the time-domain technique would be better due to the facts that it is fast and no dc bias is needed. However, for a case where the change in the characteristic frequency is very small, the frequency-domain technique would be better since it provides high precision in determining characteristic frequencies. Therefore, in this study, both frequency-domain and time-domain techniques are exploited.

4.3 Characterization of resonance behavior of magnetostrictive/magnetoelastic resonator

4.3.1 Indirect approach for the frequency-domain technique

For sensor applications, it is the characteristic frequency of a magnetic resonator rather the real resonance frequency and the absolute value of the impedance that are used to define the performance. Therefore, as long as some kind of characteristic frequency, which is related to the resonance frequency, can be easily determined, this characteristic frequency can be used as the measurement signal for the sensor characterization. Based on these considerations, an indirect approach is introduced here. The principle and circuitry design are given first and then a device made based on the design was built and tested is described. The results demonstrated that the approach works are presented and discussed.

4.3.1.1 Principle

The principle of this indirect technique is based on following. As illustrated in **Figure 4-1**, a magnetic resonator in a coil can be presented as a device (i.e. DUT) with an impedance of $Z^*(\omega)$. Therefore, if a current is applied through the device, a potential difference $U_1^*(\omega)$ is generated between the two ends of the device as shown in **Figure 4-4(a)**. Similarly, if a current is applied on a device with an impedance $Z_r^*(\omega)$, an electrical

potential difference $U_2^*(\omega)$ is generated across the two ends as shown in **Figure 4-4(b)**.

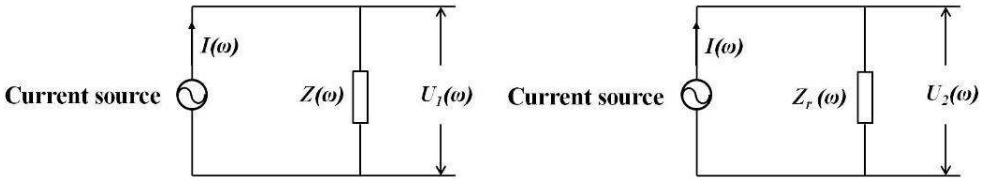

(a) **(b)**

Figure 4-4. The schematic circuit for (a) the DUT, (b) the reference.

If two identical ac $I(\omega)$ are applied to these two devices respectively, it is obtained:

$$U_1^*(\omega) = I(\omega)Z(\omega) = |U_1|e^{j(\phi_1+\omega t)} \quad (4\text{-}3)$$

$$U_2^*(\omega) = I(\omega)Z_r(\omega) = |U_2|e^{j(\phi_2+\omega t)} \quad (4\text{-}4)$$

where it is assumed that the ac current is

$$I(\omega) = I_0 e^{j\omega t} \quad (4\text{-}5)$$

where ω is the angular frequency and I_0 is the amplitude of $I(\omega)$. In Equation (4-3) and (4-4), ϕ_1 is the phase difference between $U_1(\omega)$ and $I(\omega)$, and ϕ_2 is the phase difference between $U_2(\omega)$ and $I(\omega)$.

By combining Equations (4-3) and (4-4), the impedance $Z(\omega)$ is obtained as:

$$Z^*(\omega) = Z_r^*(\omega)\frac{U_1^*(\omega)}{U_2^*(\omega)} = Z_r^*(\omega)\frac{|U_1|e^{j(\omega t+\phi_1)}}{|U_2|e^{j(\omega t+\phi_2)}}$$
$$= Z_r^*(\omega)\left|\frac{U_1}{U_2}\right|e^{j(\phi_1-\phi_2)} \quad (4\text{-}6)$$

where the $\left|\frac{U_1(\omega)}{U_2(\omega)}\right|$ is usually referred to as the gain, while the phase difference, ϕ_1 - ϕ_2, is called the phase signal.

If the impedance of the reference $Z_r(\omega)$ is a constant, the gain, $\left|\frac{U_1(\omega)}{U_2(\omega)}\right|$ is

proportional to $\left|Z^*(\omega)\right|$. Therefore, one can use this gain signal to represent the impedance of the device to be characterized since the frequency dependence of the gain will be exactly the same as the frequency dependence of the amplitude except that the values in y-axis (i.e. amplitude and gain) have a constant ratio at the same frequency. Similar with the discussion above about **Figure 4-2(a)**, both f_r^* and f_{ar}^* can be determined from the frequency dependence of the gain. If the $Z_r(\omega)$ is dependent on the frequency without a peak, the frequency dependence of the gain will be different with the frequency dependence of the impedance $Z(\omega)$. However, in this case, the frequency dependence of the gain will still show two peaks: one frequency (f_r^*) at which the gain reaches its maximum, the other frequency (f_{ar}^*) at which the gain reaches its minimum. These two characteristic frequencies of the gain are related to the resonance frequency and anti-resonance frequency of the device and are also affected by other factors including the $Z_r(\omega)$.

Similarly, if the ϕ_2 is dependent on the frequency without a peak, the frequency dependence of the phase difference, $\phi = \phi_1 - \phi_2$, will be different with the phase of the device's impedance. However, there is still a frequency (f_0*) at which the phase signal reaches its peak. This frequency is again related to the f_0 and other factors. That is, based on the gain and phase, three characteristic frequencies (f_r, f_{ar}, and f_0) can be obtained. Although these three characteristic frequencies are different with the corresponding f_r, f_{ar}, and f_0 of the impedance, they are related to the f_r, f_{ar}, and f_0. For sensor applications, any one of these three characteristic frequencies can be used as the signal. This is an indirect method.

Figure 4-5 shows the numerical fit based on the equivalent circuit and Equation (4-

1) for the experimental result of the resonance behavior of an MSP with a size of 1.0 mm x 0.3 mm x 30 µm in air. The parameters used in Equation (4-1) for the fitting are: C_s = 1.1*10^{-8} F; C_m = 0.6905*10^{-9} F; R_l = 0.038 Ω; R_m = 0.23 Ω; R_p = 0.034 Ω; L_l = 1*10^{-8} H; L_m = 0.81*10^{-5} H; L_p = 0.126*10^{-7} H.

It can be observed that for the phase signal, the fitting curve fits the experimental result very well while the simulated amplitude does not fit the experimental gain well which is as expected. However, the characterization frequencies f_r, f_{ar}, and f_0 from the simulated result are close to the corresponding frequencies from the experimental result which is consistent with the discussion above.

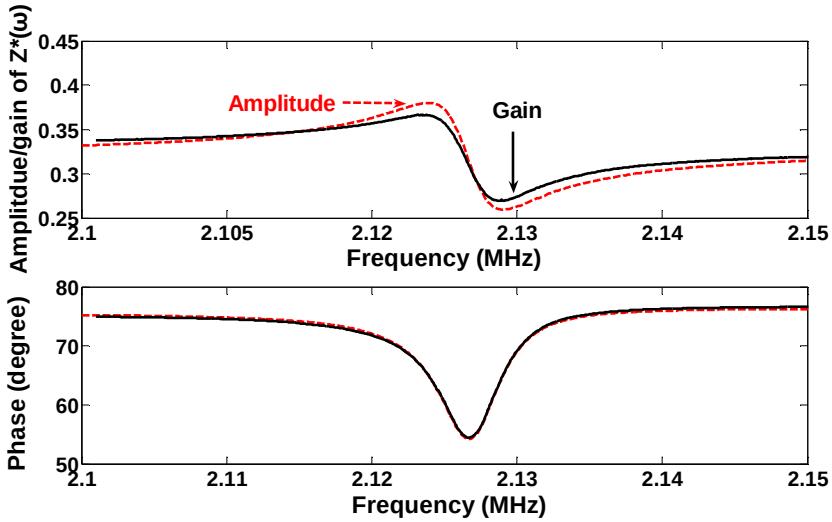

Figure 4-5. Fitting for the resonance phase behavior of a sensor in the size of 1.0 mm x 0.3 mm x 30 µm in air. The red dash lines are the fitting results while the black solid lines are the experimental results.

4.3.1.2 Circuitry design and considerations

Based on the discussion above, two identical ac current sources are needed. In this study, a high speed direct digital synthesizer (DDS) chip AD9959 was selected, which had four identical ac current sources and the frequency of the current ranged from 0 to 200 MHz. For the measurement of the phase signal and gain signal, a phase and gain

detector AD8302 was used. This chip had a maximum measurement frequency up to 2.7 GHz. Therefore, by using these two chips, the circuitry would have a capability to perform at frequencies up to 200 MHz.

The outputs signals of the AD8302 are two analog voltages: one is proportional to the gain signal, the other is proportional to the phase signal. These two analog signals are converted into digital signals using an A/D converter for the data recording. For the purpose of this study, the speed of the A/D converter is dependent on the frequency sweeping rate. That is, even for a 200 MHz measurement, the speed of an A/D can be very slow. The data recording is conducted using a regular PC or laptop.

Based on these considerations and device selections, a design of the circuitry is shown in **Figure 4-6**, where the communication between the computer and the circuitry is through a USB port. Therefore, any computer can be used here. The overall circuitry can be divided into five functional components. The specifications of each component are given below.

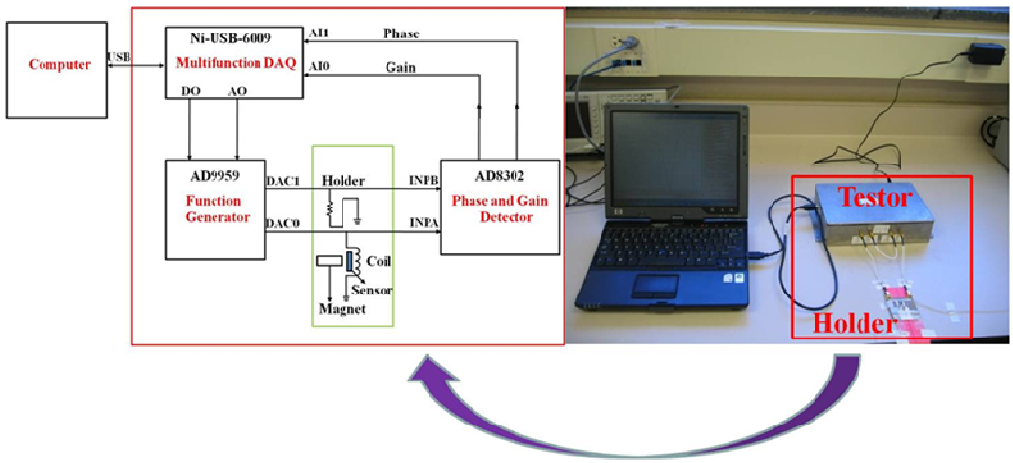

Figure 4-6. (left) block diagram of the interrogation device, (right) picture of the interrogation device.

The picture shown in **Figure 4-7** is the circuitry built based on the design shown in

Figure 4-6. In **Figure 4-6**, the right side is the picture of the outside of the box in which the circuit is built.

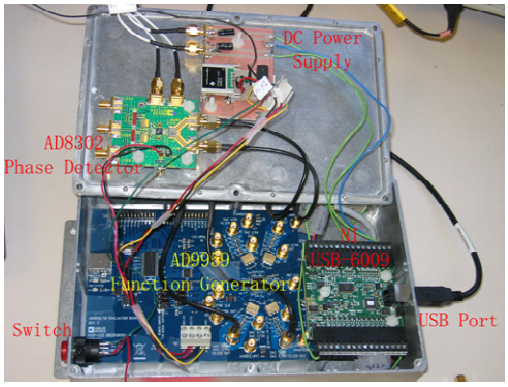

Figure 4-7. The picture of the circuit built based on the design shown in **Figure 4-5**.

Specifications of the current sources: The function generator used in the circuit is a four-channel high speed direct digital synthesizer (DDS) chip AD9959 from Analog Devices [8]. The AD9959 consists of four direct DDS cores that provide independent frequency, phase, and amplitude control on each channel. Because all channels share the same system clock, they are inherently synchronized. In the current design, only two channels are used to generate two synchronized current sine signals (i.e. the same frequency, amplitude and phase): one (called DAC1) connects with the reference $Zr(\omega)$, the other (called DAC0) connects with the DUT (i.e. sensor). The frequency range is 0 to 200MHz. The full-scale output current is from 1.25mA to 10mA with a resolution of 10 bits. The operating temperature is over the range of −40°C to +85°C. The output capacitance is 3 pF.

Holder: The holder is where the sensor, reference, and coil are. In the current device, it is a circuit board with the reference channel and sensor channel on as shown in **Figure 4-8**. The reference channel is simply a resistor, while the sensor channel has the magnetic resonator and coil(s) (i.e. DUT). If it is needed, additional resistors and capacitors can be

connected in series/parallel into the reference/sensor channel as discussed below. The dc magnet field can be generated using a magnet.

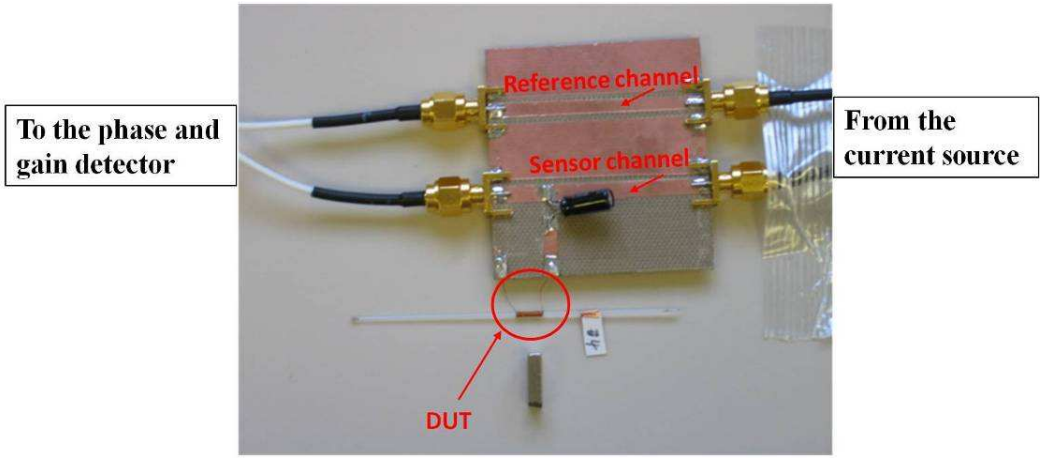

Figure 4-8. The holder built on a circuit board, where both reference and DUT channels are included. The backside of the board is grounded.

Specifications of the phase/gain measurement: The phase and gain detector AD8302 is a chip from Analog Devices which measure the phase difference between two input signals and the amplitude ratio (i.e. the gain) of the two input signals [9]. In the current device, the two input signals are the electric potential of the end of the reference and the potential of the end of the DUT, as shown in **Figure 4-5**. The ac coupled input signals ranges from –60 dBm to 0 dBm in a 50 Ω system, and from a few Hz up to 2.7 GHz [9]. The outputs provide an accurate measurement of gain over a ±30 dB range scaled to 30 mV/dB, and of phase over a 0° – 180° range scaled to 10 mV/degree [9]. The operating temperature is over the range of −40 °C to +85 °C.

Specifications of the A/D converter: In the current device, an A/D converter from National Instruments (NI), USB-6009, is used. This A/D converter is a multifunction data acquisition (DAQ) module [10]. It has eight analog input (AI) lines with a resolution of 14-bits and twelve digital I/O lines. Here analog input lines AI0 and AI1 are used to

sample the analog signals, the phase signal and gain signal from the phase and gain detector. The digital I/O lines are used to generate time sequence to control AD9959 to generate current signals. The NI USB-6009 is connected with a computer through a USB port which is simple enough to quick acquire data and generate time sequence by programming software code.

Personal computer (PC)/laptop: A graphical user interface (GUI) designed using the Microsoft Visual C++ 6.0 is run on a PC as shown in **Figure 4-9**. The GUI allows the user to set frequency sweeping range, frequency steps, data file name, and control data acquisition process and dynamically monitor the change in frequency of sensor. In **Figure 4-9**, the spectrum at top shows the phase versus frequency while the spectrum at bottom shows the frequency f_0^* versus time.

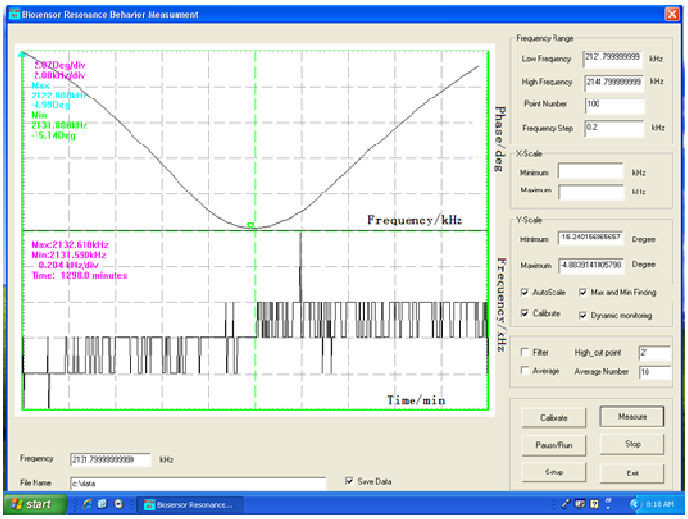

Figure 4-9. The graphical user interface (GUI).

4.3.1.3 Test results

A device was built based on the circuitry discussed above as shown in **Figure 4-6**. The device was tested to validate the principle introduced here for the characterization of a magnetic resonator using an indirect approach. **Figure 4-10** shows the resonance

frequency spectrums of an MSP with a size of 1.0 mm x 0.3 mm x 15 μm tested in air using the network analyzer and the indirect approach under the same conditions (i.e. the same dc field, sensor, and coil: L = 8.0 mm, d = 0.1mm) where in **Figure 4-10(a)** the phase signals obtained from the network analyzer and using the indirect approach are plotted as the function of frequency, while in **Figure 4-10(b)** the amplitude signal obtained from the network analyzer and gain signal obtained using the indirect approach are plotted as the function of frequency. Clearly, the phase signal shows a peak and the gain shows a maximum and a minimum. These are consistent with the expectation from the principle of this indirect approach. It is observed that the phase signals from both approaches have the similar curvatures. The frequency f_r and f_r^* at the two phase peaks are 2.126 MHz and 2.127 MHz, respectively. It is also very interesting to notice that the phase peak height from the indirect approach is much higher. For example, the phase peak height for network analyzer is about 6^o, while it is about 20^o using the indirect approach. Regarding the amplitude/gain shown in **Figure 4-10(b)**, the curvature of the relationship between the gain and the frequency is different with the curvature of the relationship between the amplitude and the frequency is as expected. For example, the amplitude of S_{11} reaches its minimum (27 dB) at a lower frequency (2.123 MHz) and reaches its maximum (34 dB) at a higher frequency (2.128 MHz), while the gain signal reaches its maximum (0.37) at a lower frequency (2.124 MHz) and reaches its minimum (0.27) at a higher frequency (2.129 MHz). However, the corresponding characteristic frequencies are close. That is f_r close to f_r*, and f_{ar} close to f_{ar}*.

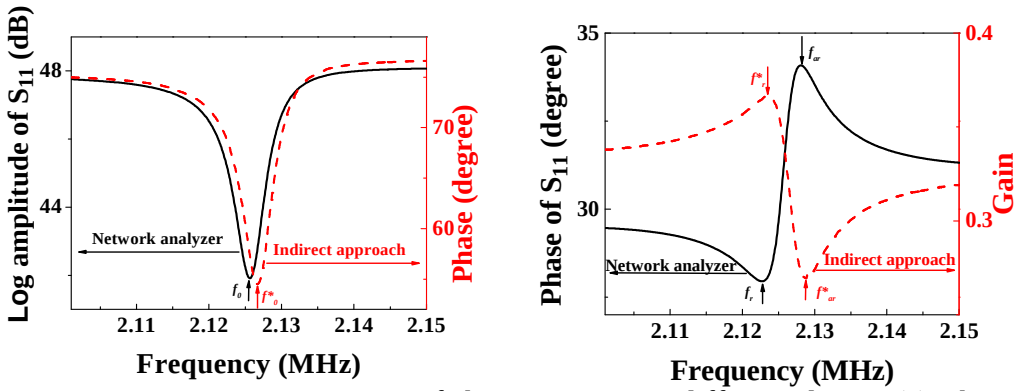

Figure 4-10. Resonance spectrum of the sensor using different device (a) Phase in relation to frequency, (b) amplitude and gain in relation to frequency where the black solid line represents the measured result using network analyzer and the red dash line represents the measured result using the indirect approach.

Figure 4-11 shows the phase and gain signal from one measurement, in which the reference was a resistor with a resistance of 3200 Ω, while the DUT was an MSP in a coil. The MSP was 1.0 mm x 0.3 mm x 30 µm in size and placed in a glass tube, while the handmade coil was wound on the outside of the glass tube using copper wire (L = 4.5mm, d = 0.1mm). In the measurement, the glass tube was filled with either air or water. That is, the MSP was tested in air or water. Based on these, three characteristic frequencies, f_0*, f_r*, and f_{ar}*, are obtained, as shown in **Figure 4-11**.

Compared with the results obtained from the MSP in air, the MSP in water exhibits a weaker signal and all three characteristic frequencies are lower than corresponding characteristic frequencies obtained from the MSP in air. Additionally, the resonance peaks observed from the MSP in water are broader than these in air. All these are consistent with resonance behavior of the MSP as discussed in Chapter 2.

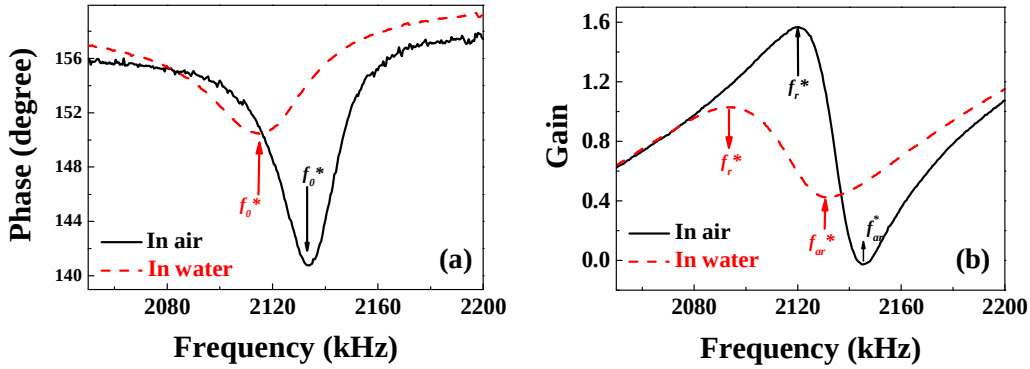

Figure 4-11. (a) Phase of $Z(\omega)$ frequency in air in relation to frequency in water; (b) Gain of $Z(\omega)$ in relation to frequency in air and in water.

The results shown in **Figures 4-10** and **4-11** indicate that the indirect measurement approach introduced here works. Based on the specifications of the components, the device built here can work at frequency up to 200 MHz. It should be noticed that the resonance frequency of the MSP here is above 2 MHz already.

To show the capability of the device for the characterization of MSPs with higher resonance frequencies, two smaller MSPs with a size of 0.75 mm x 0.15 mm x 30 µm and 0.5 mm x 0.1 mm x 30 µm respectively were tested using the device and the results are shown **Figure 4-12**. The handmade coil used for the MSP with a size of 0.75 mm x 0.15 mm x 30 µm was wound using a copper wire with a diameter of 100 µm and a length of 7.5 mm, while the coil used for the MSP in size of 0.5 mm x 0.1 mm x 30 µm was wound using a copper wire with a diameter of 25 µm and a length of 1.25 mm. The characterization frequency f_0^* of these two MSPs is about 2.85 MHz and 4.43 MHz in air and 2.81 MHz and 4.32 MHz in water, respectively. Clearly, the device works for these MSPs. Although this demonstrates the capability of the device for the characterization of the sensors with higher resonance frequencies, one can see by comparing the results shown in **Figure 4-11** and **Figure 4-12** that the signal for a smaller sensor is weaker. This

is true for the sensor as demonstrated by current impedance methods and expected by physics of the sensor! However, this makes the characterization of a small sensor difficult. Therefore, it would be interesting to enhance the signal.

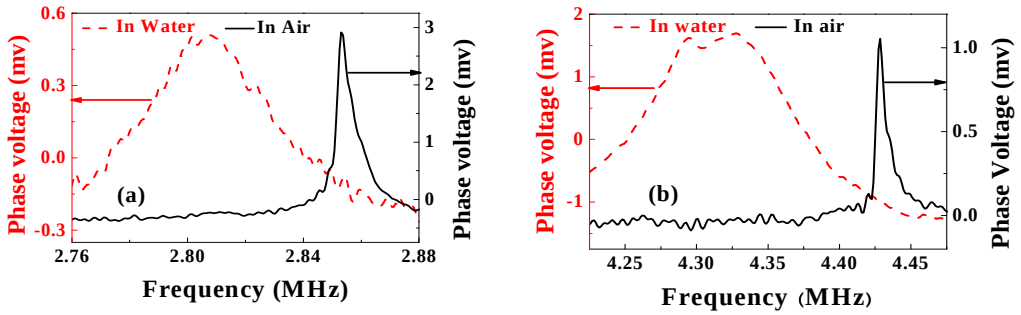

Figure 4-12. Phase signal of MSP in coil in relation to frequency. (a) MSP in size of 0.75 mm x 0.15 mm x 30 µm, (b) MSP in size of 0.5 mm x 0.1 mm x 30 µm. The dash red lines are the results for MSPs in water, while the solid black lines are the results for MSPs in air.

4.3.1.4 Study of signal enhancement

For the current impedance methods, since the absolute value of the impedance is used, the signal is fixed for a device (i.e. a magnetic resonator and a coil). However, for the indirect method introduced here, it is the gain and the phase, the difference between the magnetic resonator and a reference, rather than real impedance of the device that is measured. This would provide a way to enhance the signal. This is critical for the measurement of small resonators as demonstrated above (comparing Figure 4-10 and 4-11).

As reflected in Equation (4-6), the phase signal reflects the phase difference between the sensor and the reference. If the reference or the sensor channel is modified using a component, such as *R* and *C*, the phase signal would be changed. Therefore, it is possible to enhance the phase and gain signal by adding electronic components to the reference or sensor channel. In this study, capacitors and resistors with different

capacitances and resistances are added either in series or parallel with the DUT to explore the approach(s) to enhance the phase signal.

4.3.1.4.1 Capacitors in parallel with the DUT

Figure 4-13 shows the configuration in which a capacitor connects in parallel with the DUT.

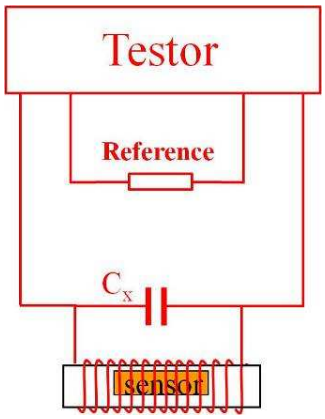

Figure 4-13. Schematic configuration of a capacitor in parallel with the DUT.

The results shown in **Figure 4-13** are the frequency dependence of both the phase signal (**Figure 4-14(a)**) and the gain signal (**Figure 4-14(b)**) for an MSP (1.0 mm x 0.3 mm x 30 µm) in a coil. In the experiment, an additional capacitor, C_x, was connected in parallel to the DUT as shown in **Figure 4-13**. The capacitance of C_x was from 150 pF to 24.7 nF.

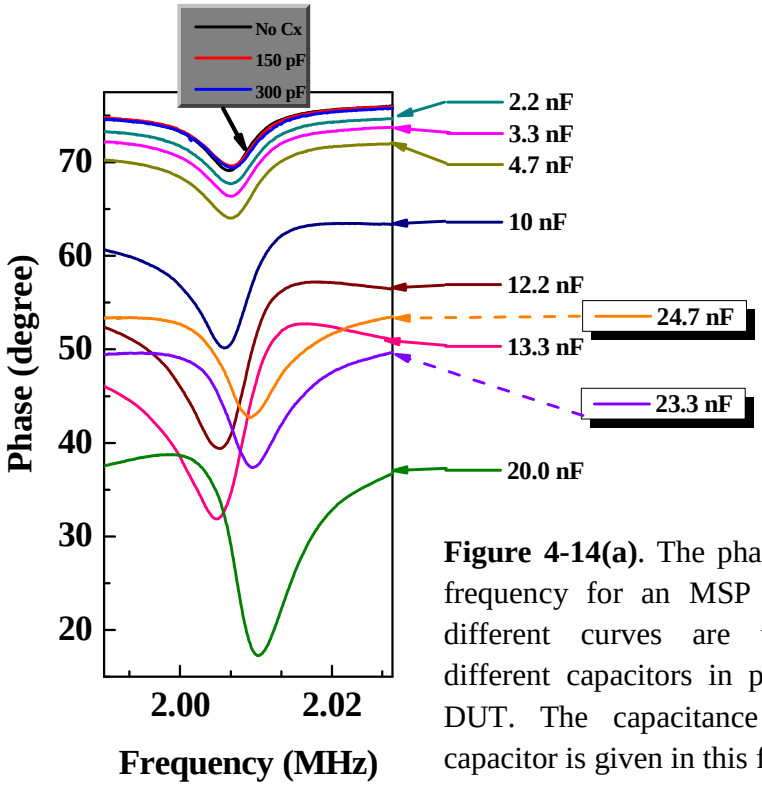

Figure 4-14(a). The phase in relation to frequency for an MSP in a coil. The different curves are the results of different capacitors in parallel with the DUT. The capacitance (C_x) of each capacitor is given in this figure.

From the results shown in **Figure 4-14(a)** (i.e. phase signal), it is found that when there is no additional C_x, the phase peak height is about 5^o. When a small C_x (i.e. C_x <3.3 nF) is added to the DUT, the peak height undergoes almost no change. However, as the C_x further increases, the phase peak height clearly increases along with increasing the capacitance of the C_x. It seems that at a C_x of about 13.3~20.0 nF the phase peak height reaches its maximum, which is about 20^o or 4 times higher than the results obtained without C_x. If the capacitance of the C_x is further increased, the phase peak height decreases with increasing capacitance of C_x. It is also observed that the characteristic frequency f_0* decreases as the C_x increases initially. However, when the C_x is higher than 13.3 nF, the f_0* increases to a higher frequency, and when the C_x is higher than 20.0 nF, the f_0* decreases again with increasing capacitance of C_x.

Regarding the gain signal shown in **Figure 4-14(b)**, it is found that the curvature of the relationship between the gain and the frequency changes with C_x. For example, when the capacitance is small, a maximum at lower frequency and a minimum at higher frequency are observed in the curve of the gain versus frequency. However, when the C_x is large, a maximum is observed at higher frequencies, while a minimum is observed at lower frequencies. It was also found that the difference between the maximum and the minimum changes with the C_x. It seems that the biggest difference between the maximum and the minimum is obtained at the C_x of about 20 nF.

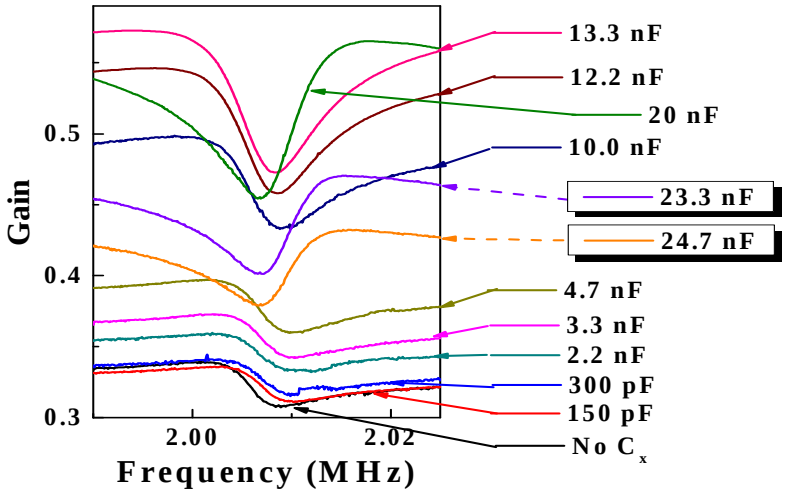

Figure 4-14(b). The gain in relation to frequency for an MSP in a coil. The different curves are the results of different capacitors in parallel with the DUT. The capacitance (C_x) of each capacitor is given in this figure.

To further study the experimental results regarding the phase signals, numerical simulation based on the equivalent model was employed. **Figure 4-15** shows the simulated results regarding the phase dependence of frequency for a 1.0 mm long MSP when different values of capacitance are added in parallel with the sensor, respectively. The parameters used in Equation (4-1) for the simulation are: C_s = $1.0*10^{-11}$ F; C_m =

$1.0*10^{-9}$ F; C_l = $1.0*10^{-9}$ F; R_l = 2.0 Ω; R_m = 0.2 Ω; R_p = 0.3 Ω; L_l = $1.0*10^{-6}$ H; L_m = $4.9*10^{-6}$ H; L_p = $1.0*10^{-7}$ H. The capacitance of C_x is from $1.0*10^{-11}$ F to $1.0*10^{-5}$ F with 60 capacitances used. The 60 capacitances are uniformly distributed over the capacitance range in a logarithm scale.

In **Figure 4-15(a)**, the *Y* axis denotes the actual phase value while in **Figure 4-15(b)**, the *Y* axis denotes the absolute value of the phase. Each curve represents a resonance spectrum for a capacitance of the C_x. Based on the results shown in **Figure 4-15(a)**, it is found that the peak height increases initially and then decreases with increasing C_x. This is consistent with the experimental results shown in **Figure 4-14(a)**. However, the value of f_0* decreases continuously with increasing capacitance of C_x, that is, the resonance peak continually moves in the same trend from upward to downward (as shown in the blue arrows) with increasing capacitances. This is different with the experimental results. However, the curves in **Figure 4-15(b)** show the same trend as the experimental results. This is due to the limit of the phase and gain detector (AD8302) because this chip can only measure the phase in the range of 0^o-180^o, which means that when the phase value is negative, it will measure the absolute value of the phase. Therefore, a sudden increase in resonance frequency is observed in the measured results. However, if the measured resonance spectrum consists of both positive and negative phase values (i.e. the red curves shown in the **Figure 4-15(a)**), the measured resonance behavior will not be the same as the expected behavior. In this case, the measured results will be same as the ones shown in **Figure 4-15(b)** (i.e. the red curves).

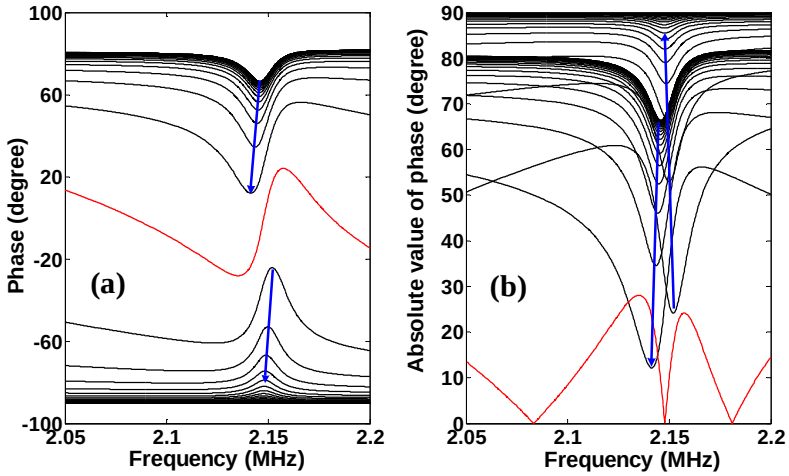

Figure 4-15. (a) Phase in relation to frequency, (b) absolute value of phase in relation to frequency. In (a) from top to bottom, the curves correspond the increase in the capacitance of C_x.

Figure 4-16(a) shows the phase peak height/amplitude obtained from the experimental results shown in **Figure 4-14(a)** as the function of the capacitance of C_x, while **Figure 4-16(b)** shows the phase peak amplitude (i.e. the difference between the maximum and minimum of the phase over the frequency range) obtained from the simulated results shown in **Figure 4-15(a)** as the function of the capacitance of C_x. Both figures show a similar trend for the dependence of the peak height/amplitude on the capacitance of C_x. All these results indicate that the height/intensity of the phase peak can be enhanced by adding a C_x and that there is an optimized capacitance for achieving a maximum phase peak height.

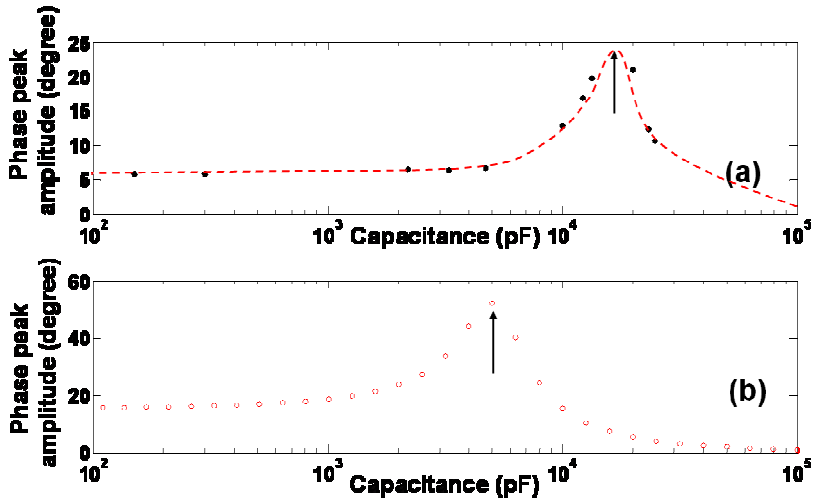

Figure 4-16. The phase peak amplitude in relation to capacitance of *Cx*: (a) experimental results, (b) simulated results.

4.3.1.4.2 Capacitors in series with the DUT

Figure 4-17 shows the configuration of a capacitor connected in series with the DUT. The experimental results regarding the resonance spectrum of the MSP (as discussed above) with different capacitances of C_x in series with the DUT are shown in **Figure 4-18**. It is observed that when the capacitance is very small, both the resonance phase signal and gain signal are so weak that almost no resonance behavior is observed. As the capacitance of the C_x increases, the resonance behavior becomes more clear and stronger. However, further increase in capacitance does not help much for enhancing both signals.

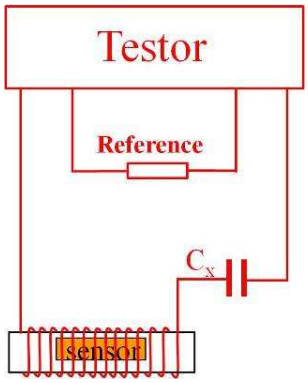

Figure 4-17. Schematic configuration of a capacitor in series with the DUT.

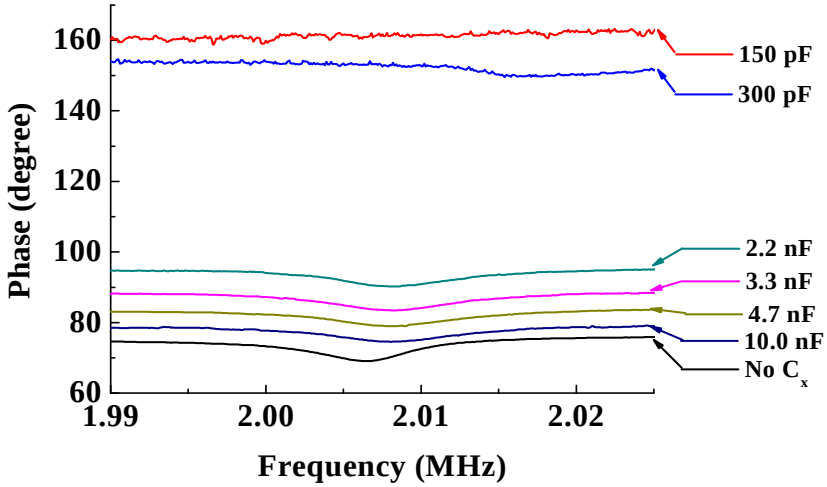

Figure 4-18(a). The phase in relation to frequency for an MSP in a coil. The different curves are the results with different capacitors in series with the DUT. The capacitance of each capacitor is given in this figure.

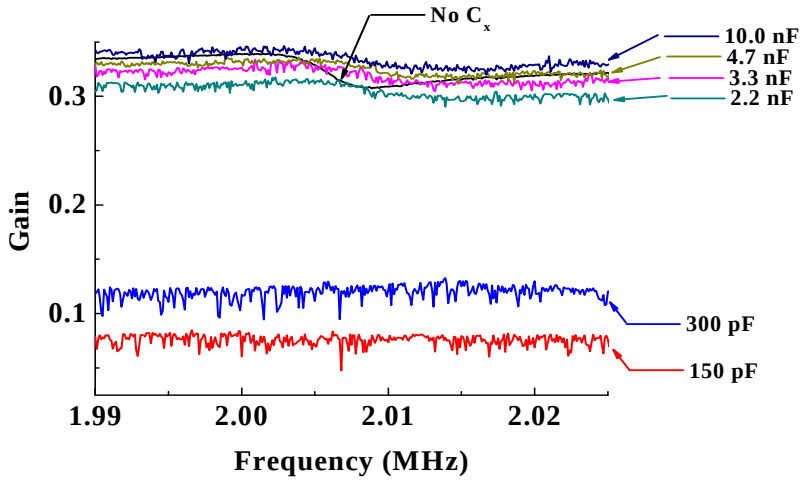

Figure 4-18(b). The gain in relation to frequency for an MSP in a coil. The different curves are the results with different capacitors in series with the DUT. The capacitance of each capacitor is given in this figure.

The simulated results regarding the resonance spectrum of this MSP with different capacitances (C_x) in series with the DUT are shown in **Figure 4-19**. The parameters used in Equation (4-1) for the simulation are the same as those used for the C_x in parallel with the DUT. A similar trend with the experimental results is observed. That is, the resonance phase curve moves from top to bottom as the capacitance of C_x increases (as shown in the red arrow) and the phase peak amplitude increases with the capacitance of C_x.

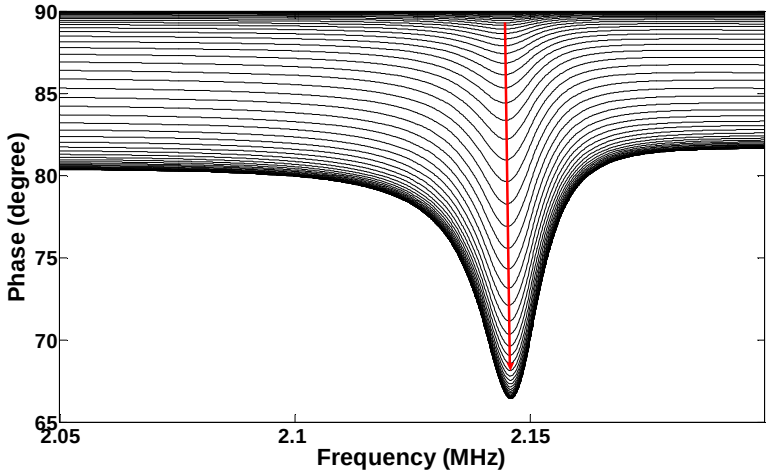

Figure 4-19. The simulation of phase in relation to frequency. The curves from top to bottom correspond to the increase in the capacitance of C_x.

Figure 4-20(a) shows the phase peak amplitude obtained from the experimental results shown in **Figure 4-18(a)** as a function of the capacitances of C_x, while **Figure 4-20(b)** shows the phase peak amplitude obtained from the simulated results shown in **Figure 4-19** as the function of the capacitance of C_x. Both figures show a similar trend for the dependence of the peak height/amplitude on the capacitance of C_x. All these indicate that the intensity of the phase peak cannot be enhanced by adding a C_x in series with the DUT.

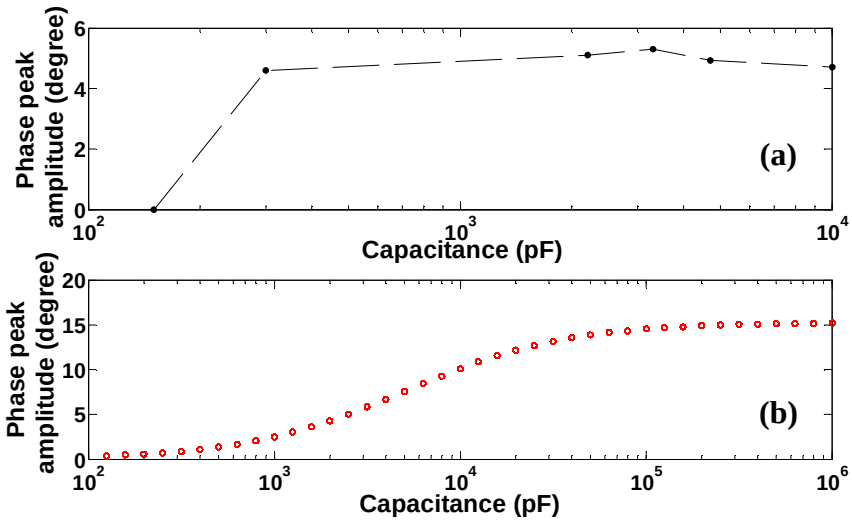

Figure 4-20. Phase peak amplitude in relation to capacitance of C_x: (a) experimental results, (b) simulated results.

4.3.1.4.3 Resistors in parallel with the DUT

Figure 4-21 shows the configuration of a resistor (R_x) connected in parallel with the DUT. The experimental results about the resonance spectrum of an MSP (the same as above) with different values of resistor in parallel with the DUT are shown in **Figure 4-22**. It is found that when the resistance of R_x is large, the resonance behavior doesn't change much with the resistance of R_x. As the resistance of R_x decreases, the resonance behavior becomes weaker. It is also found that f_0* decreases with decreasing resistance of R_x.

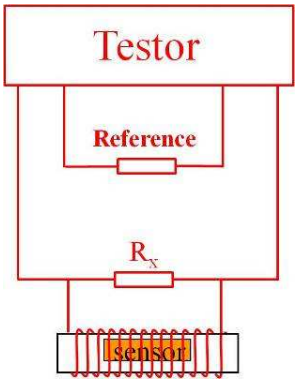

Figure 4-21. Schematic configuration of a resistor in parallel with the DUT.

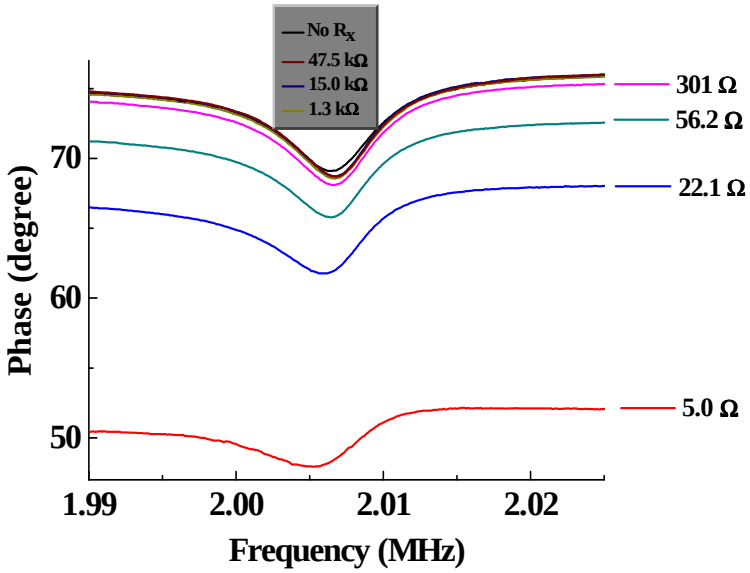

Figure 4-22(a). The phase in relation to frequency for an MSP in a coil. The different curves are the results of different resistors in parallel with the DUT. The resistance of each resistor is given in this figure.

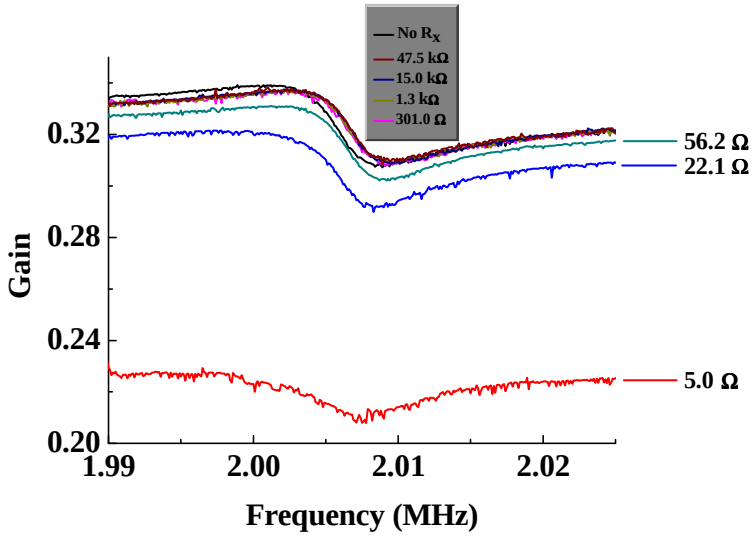

Figure 4-22(b). The gain in relation to frequency for an MSP in a coil. The different curves are the results of different resistors in parallel with the DUT. The resistance of each resistor is given in this figure.

Regarding the gain signal, the results shown in **Figure 4-22(b)** show the similar trend as the phase signal as shown in **Figure 4-22(a)**. That is, by adding R_x, the resonance behavior becomes weaker.

The simulated results regarding the resonance phase spectrum of this MSP with different resistances (R_x) in parallel with the DUT are shown in **Figure 4-23**. The parameters used in Equation (4-1) for the simulation are the same with those for the C_x in parallel/series with the DUT except that the resistance of R_x is used instead of C_x. The resistance of R_x ranges from 0 Ω to $1.0*10^6$ Ω with 60 resistances used. The 60 resistances are uniformly distributed over the capacitance range in logarithm scale. A similar trend with the experimental results was observed. That is, the resonance curve moved from bottom to top as the resistances (R_x) increase (as shown in the red arrow). The phase peak amplitude increases with the resistances (R_x).

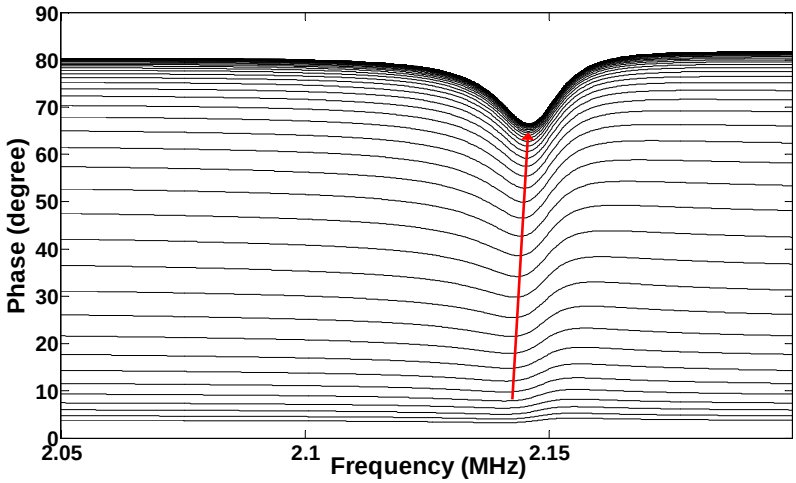

Figure 4-23. The simulation of phase in relation to frequency. The curve moves from bottom to top corresponding to the increase in the resistance of R_x.

Figure 4-24 shows the phase peak amplitude as a function of resistances of R_x based on the measured results and simulated results, respectively. In both figures, a similar trend is observed. That is, as the resistance of R_x increases, the phase peak amplitude increases at first and eventually approaches to amplitude without the resistance of R_x.

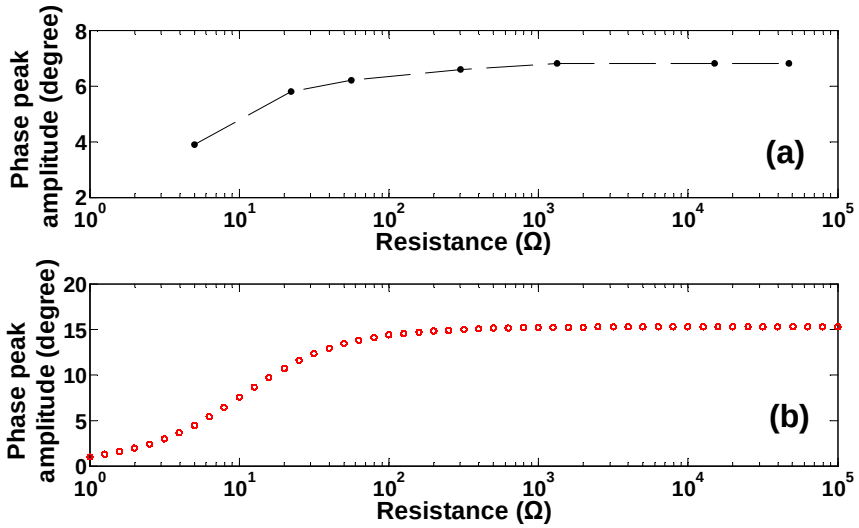

Figure 4-24. Phase peak amplitude in relation to resistances of R_x. (a) experimental results, (b) simulated results.

4.3.4.2 Resistors in series with the DUT

Figure 4-25 shows the configuration of a resistor of R_x connected in series with the DUT. The experimental results with respect to the resonance spectrum of an MSP, which is the same as in section 4.3.4.1 having different values of resistor in series with the DUT, are shown in **Figure 4-26**. It was found that when the resistance of R_x was very small, the resonance signal didn't change much. However, as the resistance increased, the resonance phase signal became weaker.

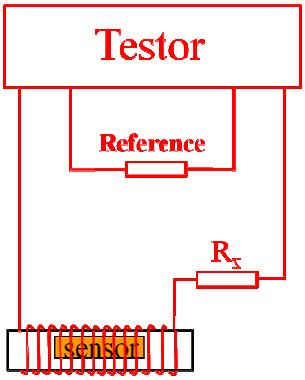

Figure 4-25. Schematic configuration of a resistor in series with the DUT.

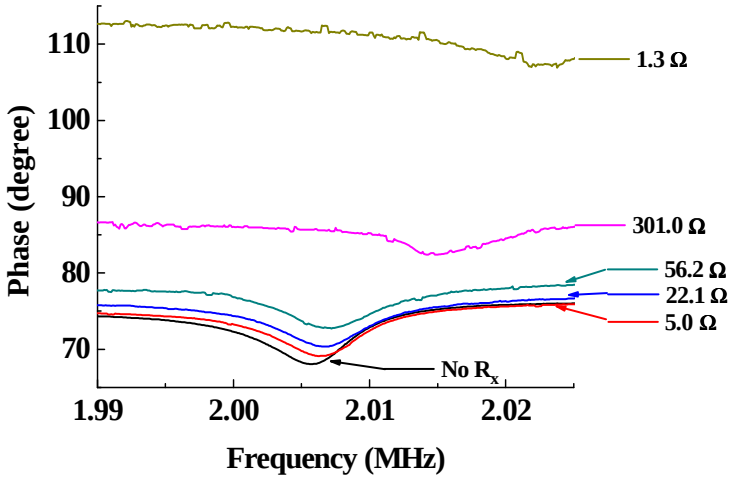

Figure 4-26(a). The phase in relation to frequency for an MSP in a coil. The different curves are the result of different resistors in series with the DUT. The resistance of each resistor is given in this figure.

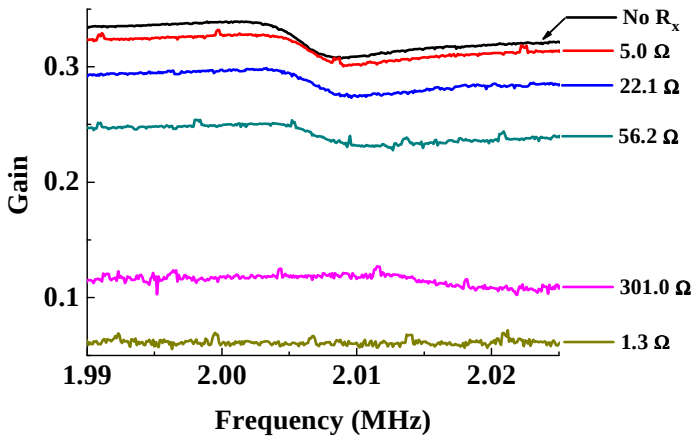

Figure 4-26(b). The gain in relation to frequency for an MSP in a coil. The different curves are the result of different resistors in series with the DUT. The resistance of each resistor is given in this figure.

The simulated results about the resonance phase spectrum of this MSP with different resistances of R_x in parallel with the DUT are shown in **Figure 4-27**. The parameters used in Equation (4-1) for the simulation are the same with those for the R_x in parallel with the DUT. A similar trend with the experimental results was observed. That is, the resonance curve moved from top to bottom as the resistances of R_x increased (as shown with the red arrow). When the resistance of R_x is very small, the resonance phase behavior is very close to the one without the resistance of R_x. The phase peak amplitude decreases with the resistance of R_x.

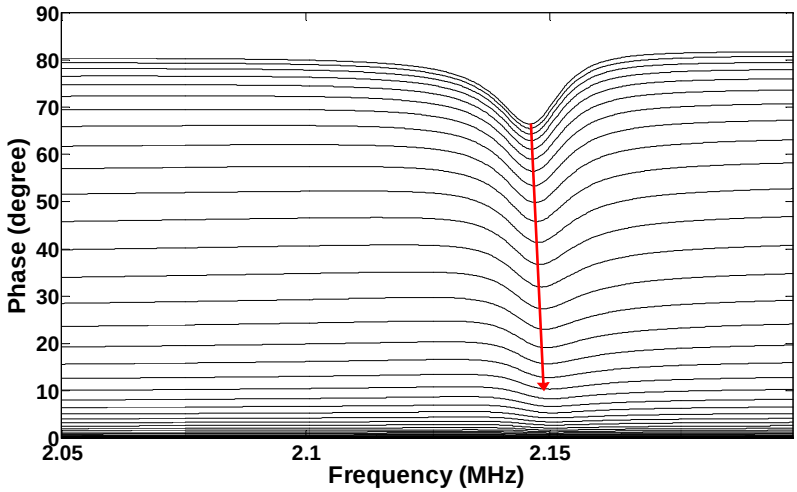

Figure 4-27. The phase in relation to frequency for an MSP in a coil. The curves from the top to the bottom correspond to the increase in the resistance of R_x.

Figure 4-28 shows the spectrum of phase peak amplitude as a function of resistances based on the measured results and simulated results, respectively. In both figures, a similar trend is observed. That is, as the resistance increases, the phase peak amplitude decreases with the resistance of R_x and eventually approaches zero.

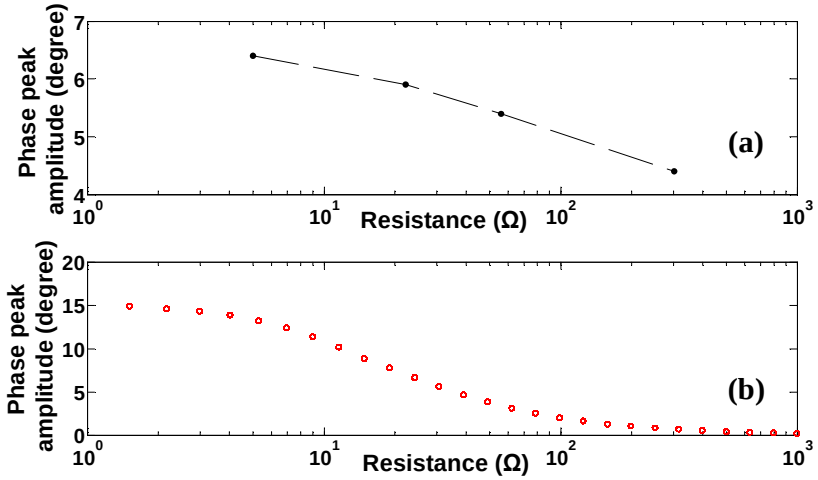

Figure 4-28. Phase peak amplitude in relation to resistances of R_x. (a) experimental results, (b) simulated results.

Taken together, if capacitors are connected in parallel to the DUT, there is a critical value of capacitance of C_x for obtaining the maximum phase signal amplitude. If

capacitors are connected in series to the DUT, there is also maximum signal amplitude when the capacitance increases to a certain value. However, for both ways (i.e. in parallel and in series) to connect resistors with the DUT, phase signal becomes weaker no matter the values of the resistance of R_x.

4.3.1.5 New design for the DUT

As discussed above (in section 4.1), a dc is needed. In the setup discussed above and the setup based on network analyzer, the dc magnetic field is provided by a permanent magnet. However, the magnetic field is not uniform. Therefore, it is of interest to determine whether the uniformity of the dc magnetic field has a significant influence on the resonance behavior (or the performance) of the MSP sensor. To generate a uniform magnetic field, a coil with a new configuration must be constructed as shown in **Figure 4-29**. Here two coils– one for an ac magnetic field and the other for a dc magnetic field are used. The ac coil is placed inside of the dc coil.

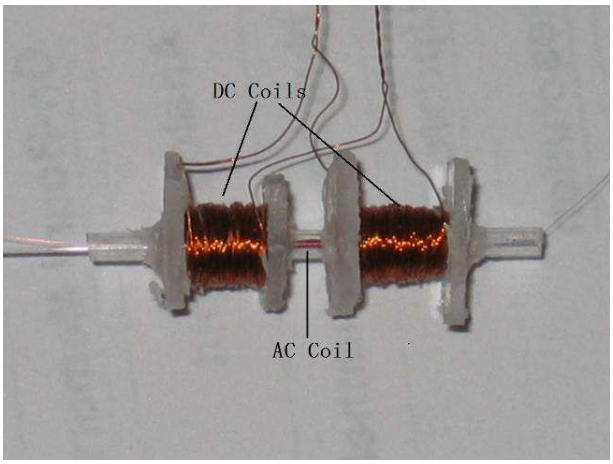

Figure 4-29. New design for dc and ac coils.

The resonance behavior of an MSP with a size of 0.75 mm x 0.15 mm x 30 μm was tested using this new coil and the results are shown in **Figure 4-30**, where only the phase

signal is plotted as the function of the frequency. The dc field was controlled using the current through the dc coil. The background of the phase signal has been deduced from the data shown in **Figure 4-30**. It is found that the characterization behavior and signal amplitude changes with the dc current. This is consistent with the results obtained from the impedance methods [11]. To further study the resonance behavior, the resonance frequency as the function of dc current and the phase signal amplitude as the function of dc current were plotted as shown in **Figure 4-31(a)** and **Figure 4-31(b)**, respectively. It was observed that the resonance frequency first decreases and then increases as shown in **Figure 4-31(a)** while the phase peak amplitude first increases and then decreases and suddenly increases as the dc current increases.

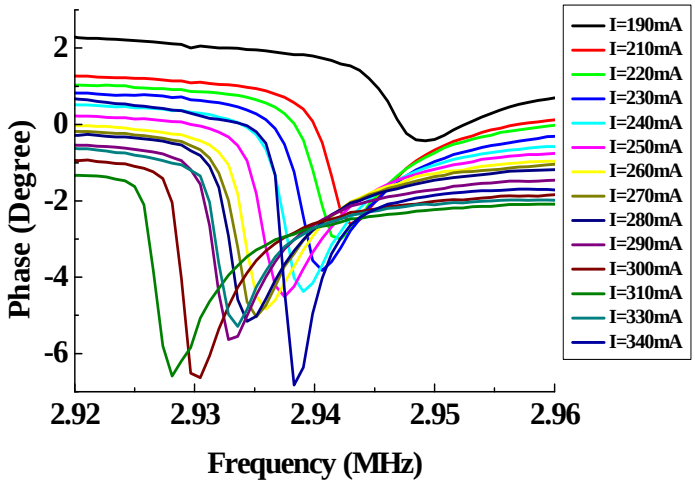

Figure 4-30. Phase in relation to frequency under different dc

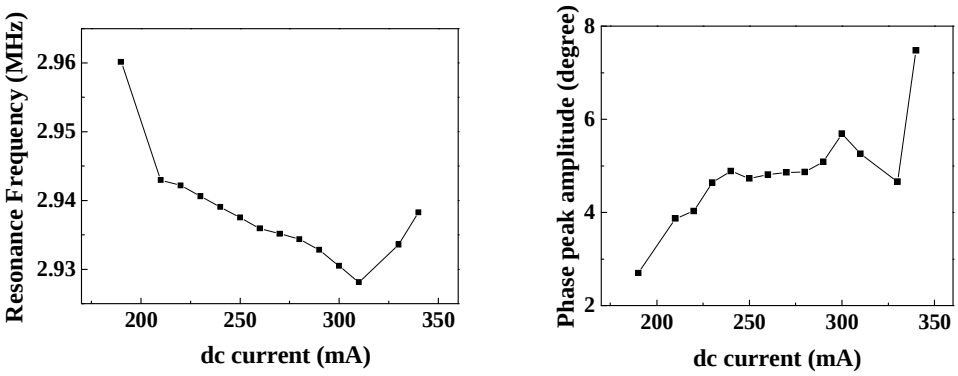

Figure 4-31. (a) Resonance frequency in relation to dc for the same sensor, (b) Phase peak amplitude in relation to dc for the same sensor.

4.3.1.6 Multiple sensor detection

One of the unique advantages of the MSP over otcher sensors is the multiple-sensor approach [11], in which multiple sensors are employed simultaneously. The multiple sensor approach provides a way to simultaneously detect different targets in an analyte. This would significantly reduce the experimental times/period and cost and is especially important in case a very limited amount of analyte is available.

In this study, only two sensors (MSP-1 and MSP-2) were used and tested. For a multiple sensor approach, different sensors may be characterized differently. To exploit the possible ways, three different configurations for the sensor channel of the setup were studied.

Configuration I: As shown in **Figure 4-32**, the two sensors are placed in one single coil.

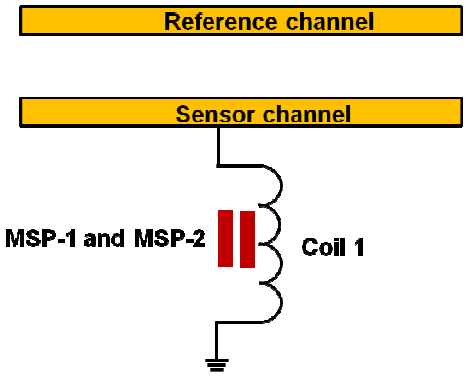

Figure 4-32. Schematic configuration I of the holder where two sensors (MSP-1 and MSP-2) were put in one coil.

The phase signal obtained is shown in **Figure 4-33** as a function of the frequency. Two peaks are clearly observed. These two peaks correspond to the characteristic frequencies of MSP-1 and MSP-2, respectively. The results demonstrate that the setup developed here can be used to characterize multiple sensors.

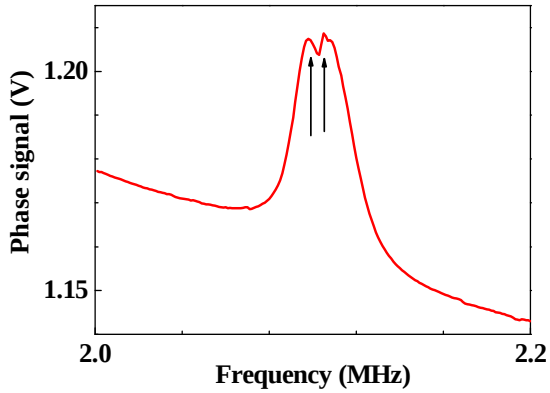

Figure 4-33. The phase signal vs. frequency for two sensors (MSP-1 and MSP-2) in one coil.

Configuration II: The two sensors (same as above) were not placed into one single coil, but each sensor was placed in one coil and the two coils were connected in parallel as shown in **Figure 4-34**.

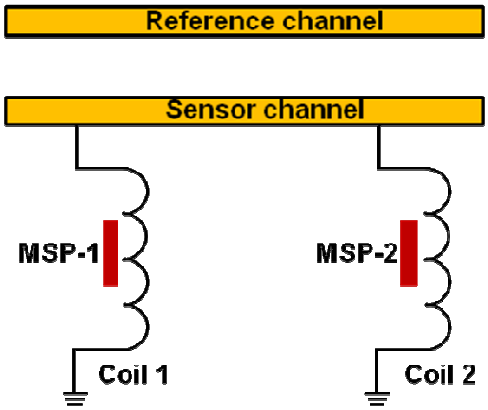

Figure 4-34. Schematic configuration of the holder where two coils are connected in parallel.

The experimental result is shown in **Figure 4-35** where only the phase signal is plotted as the function of frequency. Two peaks are clearly observed at 2.09 MHz and 2.12 MHz, respectively. These peaks are the characteristic frequency of these two MSPs showing that one sensor signal is stronger and the other sensor is weaker. Two peaks are clearly observed in this figure, and these two peaks correspond to the frequency of the two sensors.

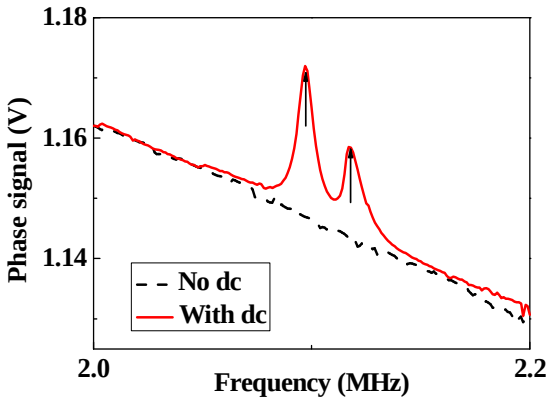

Figure 4-35. The phase signal vs. frequency for two coils: coil-1 and coil-2 connecte parallel. The MSP-1 was placed in coil-1 and MSP-2 was placed in coil-2.

Configuration III: Two coils were connected in series and each sensor was placed in one

coil as shown in **Figure 4-36**.

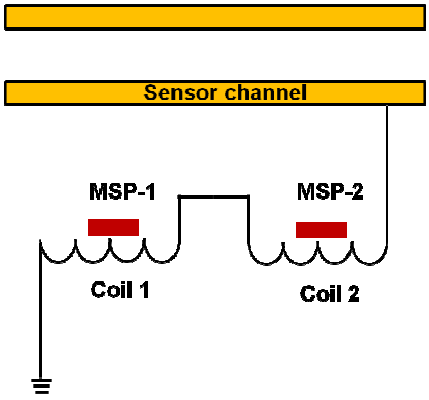

Figure 4-36. Schematic configuration III of the holder where two coils were connected in series.

The experimental result for the two sensors is shown in **Figure 4-37** where the phase signal is plotted as a function of frequency. Again, two resonance frequencies are clearly observed. The two phase signal amplitudes are different.

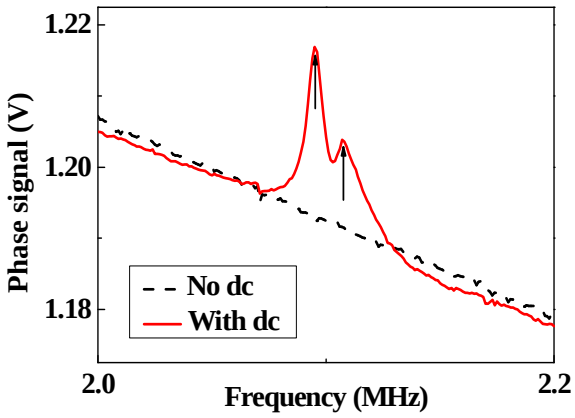

Figure 4-37. The phase signal vs. frequency for two coils: coil-1 and coil-2 connected in series. The MSP-1 was placed in coil-1 and MSP-2 was placed in coil-2.

Based on the experimental results, all the three configurations shown in **Figures 4-32**, **4-34**, and **4-36** are able to characterize multiple sensors simultaneously.

4.3.1.7 Real-time detection for *S. typhimurium*

The bacteria and phage E2 culture and sensor preparation are the same as those mentioned in Chapter 3. The experimental setup is similar to the one mentioned in Chapter 3 (section 3.6) except that the indirect frequency-domain interrogation device described in this chapter is used instead of the network analyzer.

The dose response curve of an MSP sensor (1.0 mm x 0.3 mm x 15 µm) is given in **Figure 4-38**, where the frequency shift is plotted versus the bacterial population. As can be seen in the results shown in **Figure 3-38**, a linear dose response was observed for the sensor in a population range from 5 x 10^3 cfu/ml to 5 x 10^7 cfu/ml. The sensitivity of the sensor in suspensions was 594 Hz decade^{-1} (R^2=0.992). The total change in the characterization frequency f_0^* was 5950 Hz which is close to the result (6320 Hz) from the network analyzer.

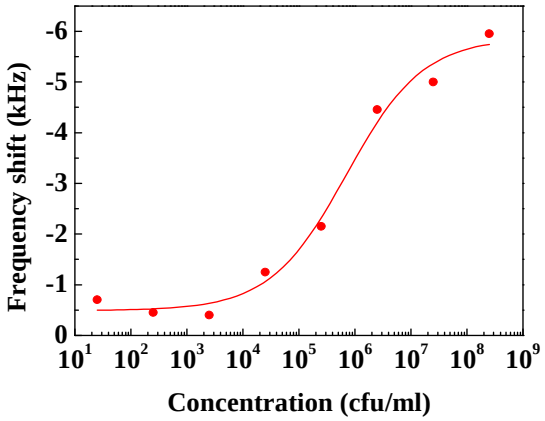

Figure 4-38. Resonance frequency shift (Hz) change with the increasing population of the *S. typhimurium* suspensions.

4.3.2 Time-domain technique

4.3.2.1 Principle

When a square pulse magnetic field is applied to a magnetic resonator, the resonator

starts vibration at its resonance frequency and the amplitude of this vibration decreases with time as shown in **Figure 4-3**. A square pulse magnetic field can be generated using a square pulse current through a coil. A single square pulse field *H(t)* as shown in **Figure 4-39** can be written as:

$$H(t)=\begin{cases} H_0 \ldots\ldots\ldots\ldots |t| < T/2 \\ 0, \ldots\ldots\ldots\ldots |t| > T/2 \end{cases} \qquad (4\text{-}7)$$

where H_0 is the pulse height and T is the pulse width.

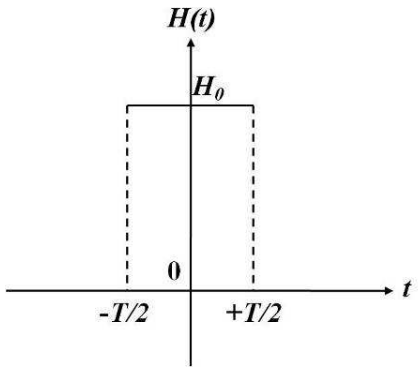

Figure 4-39. Schematic definition of a square pulse as a function of time.

By mathmatics, the square pulse function as shown in **Figure 4-39** and Equation (4-7) can be treated as a combination of many sine wave functions. Based on the Fourier Transform (FT), the relation between the single pusle and these sine waves is shown in **Figure 4-40** and expressed as:

$$H(\omega)=H_0\frac{\sin(\omega T/2)}{(\omega T/2)}=H_0\sin c(\omega T/2) \qquad (4\text{-}8)$$

where $H(\omega)=H_0$, for $\omega = 2n\pi/T$ (n =0, 1, 2…).

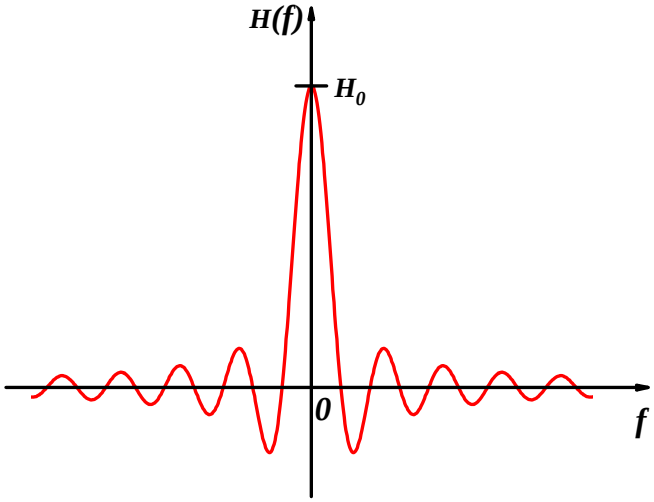

Figure 4-40. Schematic diagram of a FT magnitude spectrum of a square pulse.

After having been excited by a square pulse, the resonance behavior of an MSP sensor can also be determined once the sensor signal as a function of time is converted to a signal as a function of frequency, using FT. As a demonstration, the resonance signal of a magnetostrictive sensor after being excited by a square pulse is simulated using the NI circuit software as shown in **Figure 4-41**, where in **Figure 4-41(a)** the signal amplitude is plotted as the function of time, and in **Figure 4-41(b)** the signal amplitude is plotted as the function of frequency.

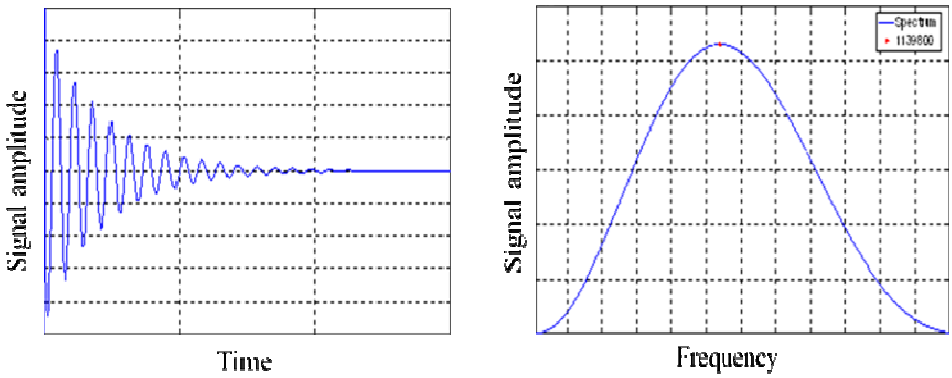

Figure 4-41. (a) Signal amplitude vs. time, (b) signal amplitude vs. frequency.

4.3.2.2 Circuitry design and considerations

When one considers on the discussion above, a square pulse current source is needed. In this study, a microcontroller ATmega32 was selected to generate the square pulse current. Since a small sensor needs a strong excitation signal, the signal amplifier MIC4451 was used for the amplification of excitation signal. A holder with a driving coil and a pick-up coil was used to drive the sensor to oscillate and pick up the sensor signal. The signal amplifier LM7171 was used to further amplify the sensor response signal. The oscilloscope TDS1001B was used to display and store the sensor response signals. The data recording was conducted using a laptop.

Based on these considerations and device selections, a design of the circuitry is shown in **Figure 4-42**, where the communication between the laptop and the circuitry is through a USB port. The overall circuitry shown in **Figure 4-43(a)** can be divided into six functional components as shown in **Figure 4-42**. Three functional components (i.e. the microcontroller and the two amplifiers) are integrated in a metal box as shown in **Figure 4-43(b)**. The specifications of the total six components are given below.

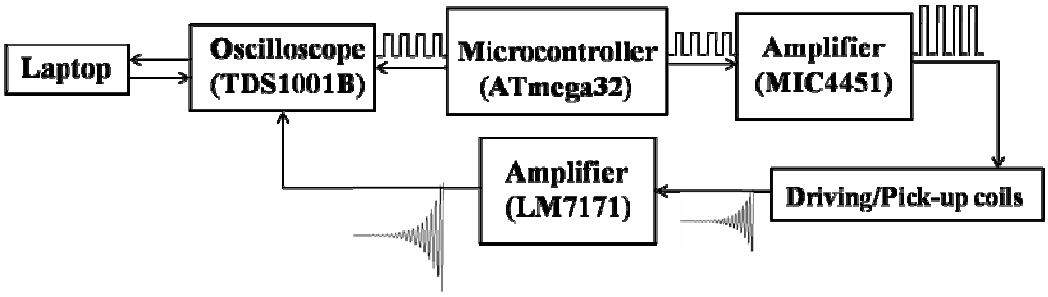

Figure 4-42. Schematic block diagrams for the time-domain interrogation device.

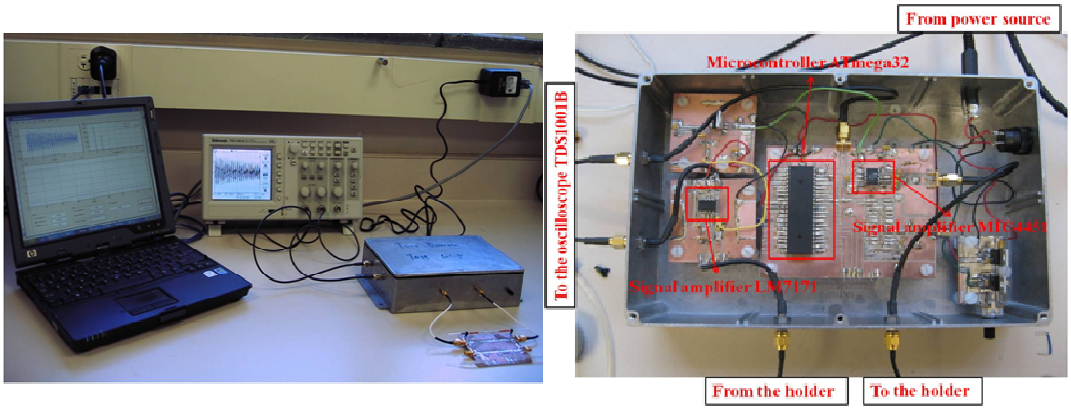

Figure 4-43. (a) Picture of the circuitry based on the design, (b) Picture of circuitry in the metal box as shown in Figure 4-44(a).

Microcontroller ATmega32 (from the Atmel Corporation) was used to generate square pulse signals and was controlled by a laptop via programming the code in 8051 assembly language [12]. An ultraviolet eraser and a universal programmer were used to erase and program the microcontroller. The ATmega32 offered a range of 4.5~5.5 V operating voltage, a maximum speed of 16 MHz and 32 K bytes of In-System Self-Programmable Flash, 1024 bytes EEPROM and 2 K byte Internal SRAM [12].

Signal amplifier MIC4451 (from the California Micrel Incorporation) was used to amplify the excitation square pulse signal [13]. It offered an operating voltage range of 4.5 V – 18 V, a 12A maximum output current, 1.0 Ω output impedance, an equivalent input capacitance of 7Pf, a 25ns of matched rise and fall times, and 30ns delay time [13]. In this design, an operating voltage of 15V was used. The operating temperature range was from -40 ^{o}C to +85 ^{o}C [13].

Holder (with driving coil and pick-up coil): A driving coil was used to induce the pulse magnetic field to excite the sensor to oscillate and a pick-up coil was used to sense the signal. In order to remove the background signal (i.e. the excitation pulse signal and other noises from coils), a pair of pick-up coils was wound with the same number but in the

opposite direction as shown in **Figure 4-44**. During measurement, the sensor was put in either end of the coils.

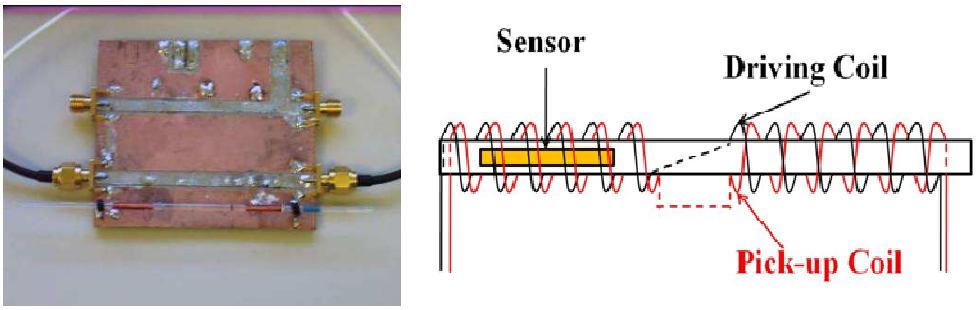

Figure 4-44. (a) Picture of the holder, (b) schematic diagram of the driving and pick-up coils.

Signal amplifier LM7171 (from National Semiconductor Corporation) was used to amplify the sensor signal. The operating voltage was specified for ± 15 V and ± 5 V [14]. In this design, a ± 5V voltage was used for amplifying. The differential gain and phase were 0.01% and 0.02^{o}, respectively. The output current was 100mA and the operating temperature range was from -40 ^{o}C to +85 ^{o}C [14].

Digital storage oscilloscope TDS1001B (from TekNet Electronics Incorporation) was used to display/capture the waveform of the sensor signal and convert the analog signal to digital signal. It had two channels and 2 USB 2.0 ports. The sample rate was 500 MS/s in real time. The input impedance was 1 MΩ in parallel with 20 pF [15]. The bandwidth was 40 MHz. The time base range is 50 ns/div to 50 s/div [15].

PC/laptop was used to receive the output signals from the oscilloscope and converted the signals to frequency-domain signal by FFT. A graphical user interface (GUI) was designed using the MATLAB 7.0 and run on a laptop as shown in **Figure 4-45**. It displayed the sensor response in time-domain behavior (as shown in left up) and also in frequency-domain behavior (as shown in right up). It also displayed the resonance

frequency as the function of time (as shown in bottom).

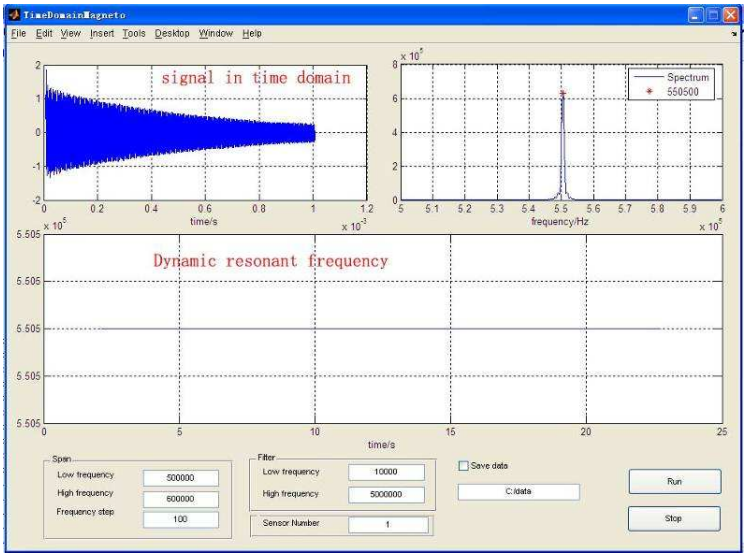

Figure 4-45. The graphical user interface (GUI).

During measurement, the microcontroller generated two identical square pulse signals with a voltage amplitude of 5V to the DUT (coils and sensor) and the oscilloscope, simultaneously. The signal that is serving as an excitation signal first passes through the signal amplifier (MIC4451), followed by the driving coil and then the signal amplifier (LM7171**)**, and finally it goes to the oscilloscope (TDS1001B). The other pulse signal went directly to the oscilloscope as a trigger signal which was used to set a position for the oscilloscope to sample the sensor response signal. After finishing sampling, the oscilloscope transferred the data to the laptop. By doing FFT, the resonance peak of the sensor was determined and recorded by the laptop.

4.3.2.3 Test results

The device, which was built based on the circuitry shown in **Figure 4-43,** was tested to validate the principle introduced here for the characterization of a magnetic resonator.

Figure 4-46 shows the result of an MSP sensor (6.0 mm x 1.0 mm x 30 µm) from one measurement. The sensor was placed in a glass tube, while the handmade coil was wound on the outside of the glass tube using copper wire (L = 10.0 mm, d = 0.1 mm). In the measurement, the glass tube was filled with either air or water. That is, the MSP was tested in air or water. Each sensor signal clearly shows a peak.

Comparing the results obtained from the MSP in air, the MSP in water exhibited a weaker signal and the resonance frequency was lower than corresponding resonance frequency obtained from the MSP in air. All of these are consistent with resonance behavior of the MSP as discussed in Chapter 2.

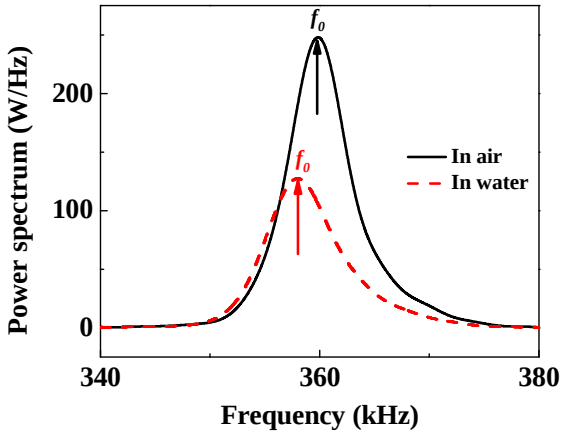

Figure 4-46. The power spectrum vs. frequency for an MSP sensor.

4.3.2.4 Multiple sensor detection

As mentioned above, multiple sensor detection is one of the unique advantages of the MSP over other sensors. In this study, four sensors (MSP-1: 8.0 mm x 1.0 mm x 30 µm and MSP-2: 6.0 mm x 1.0 mm x 30 µm, MSP-3: 2.0 mm x 0.3 mm x 30 µm, MSP-4: 1.5 mm x 0.3 mm x 30 µm,) were tested in air and in water but only two sensors were tested at one time. During the measurement, the two sensors were placed at the two ends

of the coil, respectively. The coil was made of copper wire (L = 10.0 mm, d = 0.1 mm).

Figure 4-47 shows the power spectrum signals as the function of the frequency. Clearly, two peaks are observed for each curve. In the two figures, the four peaks in black solid curve correspond to the resonance frequencies of the four sensors in air while the four peaks in the red dashed curve are the resonance frequencies of the four sensors in water. It was observed that the resonance frequency in water for each sensor is lower than that in air which is consistent with the discussion in Chapter 2. The results demonstrate that the setup developed here can be used to characterize multiple sensors.

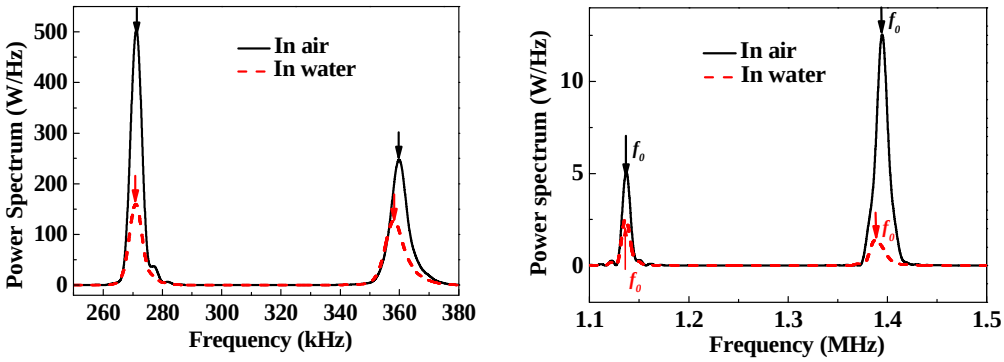

Figure 4-47. The power spectrum vs. frequency for (a) two sensors (MSP-1 and MSP-2) in air and in water, (b) two sensors (MSP-3 and MSP-4) in air and in water.

4.3.2.5 Effect of pulse voltage on resonance behavior

From the experimental results shown in **Figure 4-47**, it was also found that when the signal of sensor with a smaller size is much weaker than a sensor with a bigger size. Since the MSP sensor is actuated by the excitation pulse, it is of interest to study the effect of the pulse voltage on the resonance behavior of an MSP sensor. In this study, the effect of different pulse voltages on the resonance behavior of a sensor was studied. **Figure 4-48** shows the power spectrum of a sensor (13.5 mm x 1.0 mm x 30 µm) as the function of frequency under different pulse voltages. From the results, it can be observed

that the resonance frequency of the sensor increases with the voltage. The signal amplitude first increases with the voltage and then decreases with the voltage. This indicates that there is a certain voltage at which, the signal amplitude reaches its maximum. This is consistent with the magnetostrictive effect which was discussed in Chapter 1. Since the dc field is proportional to the voltage, the maximum output signal amplitude should be expected to be at a certain value of voltage/dc.

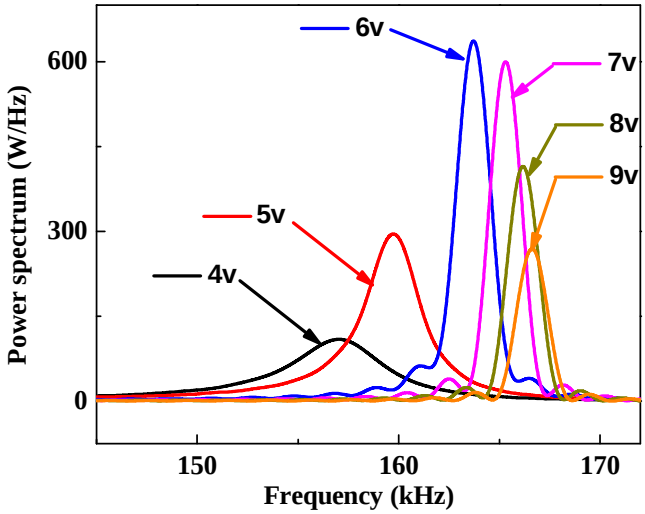

Figure 4-48. The power spectrum vs. frequency under different pulse voltages for an MSP sensor.

4.3.2.6 Real-time detection of *S. typhimurium*

The preparation of *S. typhimurium* and phage E2 cultures were the same as those mentioned in Chapter 3. The sensor used in this experiment was in size 2.0 mm × 0.4 mm × 30 µm. The phage immobilization and detection procedure was also the same as that mentioned in section 3.3. The flow rate for this experiment was 0.11 ml/min. The experimental setup for detecting bacteria was similar to the frequency-domain technique mentioned in section 3.6. The only difference was that the time-domain interrogation

device was used instead of other interrogation devices.

Figure 4-49 shows the frequency shift of the phage immobilized sensor, reference sensor (sensor devoid of phages and casein) and casein wt 5% controlled sensor in response to the increasing populations of *S. typhimurium*. The results show that the dose responses are linear for the phase immobilized sensor in the range from 5 x 10^2 cfu/ml to 5 x 10^7 cfu/ml. The sensitivity of the sensor is 400Hz decade^{-1} (R^2=0.9970). The results show that the frequency shift of the casein controlled sensor is the smallest, the reference sensor is the second smallest, and the phage immobilized sensor is the largest. The results show the fewest bacterial cells binding on the casein controlled sensor and the most bacterial cells binding on the phage immobilized sensor.

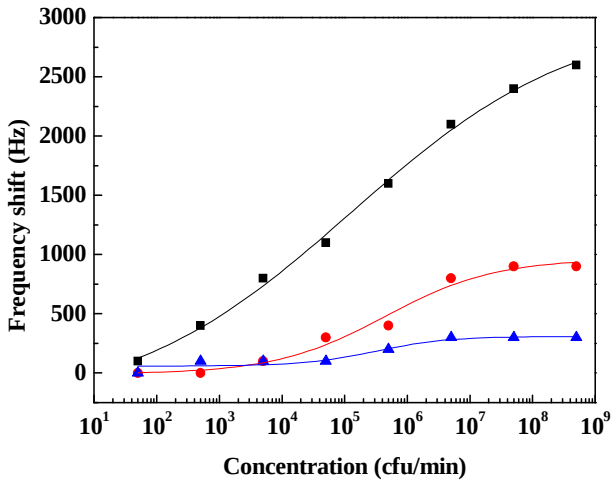

Figure 4-49. The dose response of a magnetostrictive phage immobilized sensor (Black square), Reference sensor (Red dot), and casein blocked sensor (Blue triangle).

4.4 Conclusions

Two types of portable, high frequency setups based on frequency-domain and time-domain techniques for the interrogation of MSP sensors were developed and studied. The devices were validated by measuring the MSPs in air and in water. For the frequency-

domain technology based indirect approach, the resonance behavior (i.e. phase and gain) was simulated based on the assuming equivalent circuits using MATLAB. It was found that the simulated result can fit the experimental result very well. It also shows that the sensor signals can be enhanced by combining additional capacitances parallel to the sensor channel. Three different configurations of the device under test (DUT) were designed and tested for the application of multiple sensor detection. The results showed that all the three designs are capable of multiple sensor detection. A new configuration of the DUT which can generate a uniform dc magnetic field was design and tested. The effects of different dc currents on the resonance behaviors of an MSP were studied. The device was employed to characterize the characterizing frequency of an MSP biosensor (1.0 mm x 0.3 mm x 15 μm) for the detection of *S. typhimurium*. A similar result was obtained as that when using the network analyzer. For the time-domain technology, the effects of different pulse voltages on the sensor signal were studied. The results show that the sensor signal can be enhanced when the pulse voltage is at a critical value. The device was also employed to characterize the resonance frequency of an MSP biosensor (2.0 mm x 0.4 mm x 30 μm) for the detection of *S. typhimurium*.

Based on the experimental results, both of the devices show good performance at characterizing MSPs and are capable of in-field detection. For frequency-domain based indirect approach, the measurement speed is slower but can obtain a stronger sensor signal. For the time-domain device, the output sensor signal is weaker but the measurement speed is faster. Therefore, whether to use a time-domain or frequency-domain device for the sensor application depends on which need dominates.

References

1. L.L. Fu, S.Q. Li, K.W. Zhang, I.H. Chen, V.A. Petrenko, Z.Y. Cheng, Magnetostrictive Microcantilever as an Advanced Transducer for Biosensors, Sensors 7 (2007) 2929-2941.
2. M.L. Johnson, J.H. Wan, S.C. Huang, Z.Y. Cheng, V.A. Petrenko, D.J. Kim, I.H. Chen, J.M. Barbaree, J.W. Hong, B.A. Chin, A wireless biosensor using microfabricated phage-interfaced magnetoelastic particles, Sensors and Actuators A 144 (2008) 38–47.
3. R.S. Lakshmanan, R. Guntupalli, J. Hu, D.J. Kim, V.A. Petrenko, J.M. Barbaree, B.A. Chin, Phage immobilized magnetoelastic sensor for the detection of *Salmonella typhimurium*, Journal of Microbiological Methods 71 (2007) 55–60.
4. R. Guntupalli, J. Hu, R.S. Lakshmanan, T.S. Huang, J.M. Barbaree, B.A. Chin, A magnetoelastic resonance biosensor immobilized with polyclonal antibody for the detection of *Salmonella typhimurium*, Biosensors and Bioelectronics 22 (2007) 1474–1479.
5. K.F. Zeng, C.A. Grimes, Threshold-crossing counting technique for damping factor determination of resonator, Sensors75 (2004) 5257-5261.
6. K.F. Zeng, K.G. Ong, X. Yang, G.A. Grimes, Board level integrated microsystern design and associated technique for impedance analysis of resonator sensors, Review of Scientific Instruments Sensor Letters 4 (2006) 388-397.
7. R.L. Copeland, M. Kopp, Analysis of A Magnetoelastic Sensor, IEEE Transactions on Magnetics 30 (1994) 3399-3402.
8. "http://www.analog.com/static/imported files/data_sheets/AD9959.pdf."
9. "http://www.datasheetcatalog.org/datasheet/analogdevices/797075782AD8302_a.pdf

10. “http://www.ni.com/pdf/products/us/20043762301101dlr.pdf.”
11. S.Q. Li, Development of novel acoustic wave biosensor platforms based on magnetostriction and Fabrication of magnetostrictive manowires, Dissertation, Auburn University, 2007.
12. “http://www.datasheetcatalog.org/datasheet/atmel/2503S.pdf.
13. “http://www.datasheetcatalog.org/datasheet2/2/05acqj96l0ywk7wiozea3oyd2jcy.pdf.”
14. “http://www.datasheetcatalog.org/datasheet/nationalsemiconductor/DS012385.PDF.”
15. “http://www.valuetronics.com/vt/assets/pdfs/TEK_TDS1000B_2000BDatasheet.pdf.”

CHAPTER 5

SYNTHESIS OF AMORPHOUS COBALT-IRON-BORON ALLOY FOR MAGNETOSTRICTIVE BIOSENSOR PLATFORM APPLICATION

5.1 Introduction

To review what was said in Chapters 1 and 2, the theoretical simulation and experimental results indicate that the sensitivity of the MSP increases when the size of its features decrease and that the smaller the MSP, the higher the resonance frequency. Therefore, MSPs in micro/nano-sizes are strongly desired to develop highly sensitive sensors. The MSPs used currently are made from a commercially available magnetostrictive alloy, Metglas 2826MB^{TM} [1-5]. Although this alloy exhibits excellent qualities, such as high *Q* value and good corrosion resistance, the alloy is not suitable for the fabrication of nano-sized MSPs since this alloy is cast by liquid-quenching technique [6]. Therefore, it is necessary to synthesize the magnetostrictive materials with techniques that can be combined with the micro/nano structure fabrication process. Additionally, it is required that the magnetostrictive materials exhibit good magnetostrictive effect at high frequency. Unfortunately, to the best of our knowledge, very little research has been done on this topic. By using sputtering and electrochemical deposition techniques, an amorphous Fe-B alloy was prepared in thin film and bars with reasonable magnetostrictive performance as the alloy had a composition of about 80 atm% of Fe and 20 atm% B [7, 8]. However, this Fe-B alloy has a low corrosion resistance, which strongly limits the application of this material in the development of high performance

biosensors.

In this research, the Co-Fe-B alloy in micro/nano scale was considered as a candidate for a magnetostrictive alloy operated at high frequency. This alloy was prepared using electrochemical deposition. The Co-Fe-B alloy was fabricated in the shape of a thin film, bar, and tube. Based on the property study of bulk Co-Fe-B alloy, it is known that this alloy exhibits a better corrosion resistance.

5.2 Materials preparation

The Co-Fe-B thin films and nanobars/nanotubes were electrochemically deposited from an aqueous basic solution of cobalt (II) chloride ($CoCl_2 \cdot 6H_2O$), iron sulfate heptahydrate ($FeSO_4 \cdot 7H_2O$), boric acid (H_3BO_3), dimethylamino borane (DMAB) ($BH_3NH(CH_3)_2$), sodium citrate ($C_6H_5Na_3O_7$), glycine ($C_2H_5NO_2$), and sodium saccharin ($C_7H_4O_3NSNa \cdot 2H_2O$) [9]. The $CoCl_2 \cdot 6H_2O$, FeSO4·$7H_2O$, and DMAB provided the sources for cobalt, iron, and boron, respectively. H_3BO_3 worked as the buffer, sodium citrate was used to prevent the formation of iron hydroxide precipitation, and Na saccharin was used to relieve stress.

All the chemicals for preparing the deposition solution (100ml) were weighted using a balance with a resolution of 0.0001 g. The preparation procedures were as below. Firstly, sodium citrate was dissolved in distilled water in order to prevent the oxidation of Fe^{2+} and precipitation. Secondly, $FeSO_4 \cdot 7H_2O$ was added into the solution and completely dissolved. Then, $CoCl_2 \cdot 6H_2O$, H_3BO_3, DMAB, Glycine, and Na saccharin were serially added into the solution and completely dissolved, respectively. Finally, a uniform reddish solution with a pH around 4.5 was formed and ready to be used.

5.3 Electrochemical deposition of amorphous Co-Fe-B thin films

In this part of the research, Co-Fe-B thin films were fabricated based on the electrochemical deposition method. All the films were deposited by galvanostatic deposition. The deposition process was controlled by an Epsilon^{TM} electrochemistry analysis network obtained from Bioanalytical System, Inc. This method used a three electrode configuration including a reference electrode, a counter electrode, and a working electrode. Compared with a two electrodes configuration which only consists of a working electrode and a counter electrode, the three electrode configuration can control the deposition process much more precisely. During the deposition, an external potential was applied to the cell, and the corresponding current went through the electrodes. In this case, a potential drop exists across the cell due to the solution resistance. During the deposition process, in order to maintain a constant *I*, the *V* was adjusted between the reference electrode and working electrode since the resistance of the solution *R* may change during deposition while the current passing between the working electrode and the counter electrode is controlled. A standard Ag/AgCl electrode, obtained from Bioanalytical System, Inc. was used as the reference electrode in this research. A platinum mesh obtained from Alfa Aesar, in the size of 2 cm x 2 cm, was used as the counter electrode. A glass slide coated with a Cu (2.5 μm)/Cr (100 nm) bilayer was used as the working electrode. The Cr layer was first deposited by RF sputtering on the glass slide as an adhesion layer, and then a Cu layer was deposited on the Cr layer using DC sputtering to form the working electrode. The working electrode and the counter electrode were placed vertically and face to face in the plating bath with 1 cm working distance as shown in **Figure 5-1**. The Co-Fe-B thin films were deposited on the surface

of the working electrode under constant current.

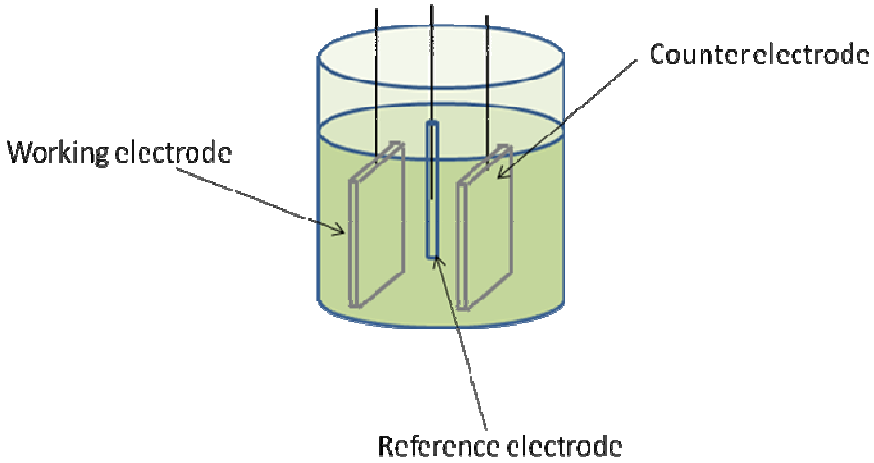

Figure 5-1. Electrochemical cell for Co-Fe-B thin film deposition.

In this part of the research, Co-Fe-B thin films were deposited from plating baths with different concentrations of $FeCl_2 \cdot 6H_2O$ and $BH_3NH(CH_3)_2$. The compositions of plating baths employed are listed in **Table 5-1**.

Table 5-1. Composition of baths for Co-Fe-B thin film deposition [9].

Composition	Concentration (mol/L)
Cobalt (II) chloride ($CoCl_2 \cdot 6H_2O$)	0.35
(iron sulfate heptahydrate) $FeCl_2 \cdot 6H_2O$	0.01–0.10
Boric acid (H_3BO_3)	0.73
Na Citrate ($Na_3C_6H_5O_7 \cdot 2H_2O$)	0.07
DMAB($BH_3NH(CH_3)_2$)	0.01-0.05
Glycine($C_2H_5NO_2$)	0.13
Na Saccharin($C_7H_4NNaO_3S \cdot 2H_2O$)	0.01

5.3.1 Feasibility of Co-Fe-B thin films

In this part of the research, Rigaku system X-ray diffractometer systems were used to characterize the Co-Fe-B thin films. All the XRD scans were performed at room temperature. For the Rigaku system, the XRD scans were performed using symmetric θ - 2θ diffraction. The X-ray source was Ni-filtered Cu Kα (wave length = 1.54 Å) radiation

at 40 kV and 40 mA.

5.3.1.1 Effect of deposition current on thin film microstructure

In order to discover the effects of deposition current on the film structure, four Co-Fe-B thin films using the same bath were prepared under different deposition currents (i.e. 4 mA, 5 mA, 6 mA, and 15 mA, respectively). The bath for fabricating the thin films is listed in **Table 5-2.**

Table 5-2. Composition of bath *A* for Co-Fe-B thin film deposition.

Composition	Bath *A* (mol/L)
$CoCl_2 \cdot 6H_2O$	0.35
$FeSO_4 \cdot 7H_2O$	0.01
H_3BO_3	0.73
Na Citrate ($Na_3C_6H_5O_7 \cdot 2H_2O$)	0.07
DMAB($BH_3NH(CH_3)_2$)	0.05
Glycine($C_2H_5NO_2$)	0.13
Na Saccharin($C_7H_4NNaO_3S \cdot 2H_2O$)	0.01

The XRD patterns of the four Co-Fe-B films are shown in **Figure 5-2**. All the films were deposited on Cu/Cr pre-coated glass slides. The results show only one broad peak on the XRD pattern in the range of angle $2\theta = 40^o \sim 50^o$ respectively, indicative of amorphous structure of Co-Fe-B. A sharp peak near 45^o corresponds to the cubic structure of FeCo (111). When I = 4mA and I = 5mA, there are two sharp diffraction peaks which correspond to the two FCC Cu reflections (111) and (200) appearing in the XRD patterns. This is due to the fact that the two films are thinner allowing the X-rays have penetrated the films at relatively larger incident angles ($40^o \sim 50^o$), yielding the information about the Cu substrate. However, when the deposition current is higher, more ions move to the Cu substrate during electrodepositing and a thicker Co-Fe-B film is obtained so that the X-ray is not able to penetrate it and thus the diffraction peaks of Cu are eliminated. The crystalline sizes of the thin films were calculated by Sherrer equation

as [9]

$$t = 0.9\frac{\lambda}{B\cos\theta} \qquad (5\text{-}1)$$

where t is the grain size, λ is the wavelength of the X-ray and B is the width of the diffraction peak at half height and 2θ is the angle at the diffraction peak.

Based on Equation (5-1), the sizes were around 17.0 Å, 16.0 Å, 17.0 Å and 45.5 Å for the films deposited under current 4 mA, 5 mA, 6 mA and 15 mA, respectively. The wavelength of 1.54 Å for Cu Kα as X-ray source was used in the calculation. For the film deposited at I = 15 mA, the diffraction peak corresponding α-Fe reflection (110) appears in the XRD pattern which indicates the low B contents in the thin film. Based on the XRD results, 5 mA was selected to be used to prepare the thin film.

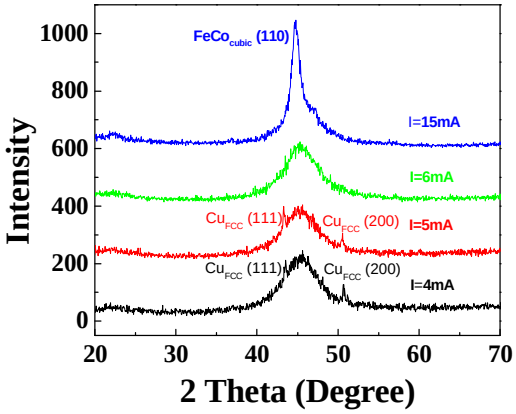

Figure 5-2. XRD patterns of Co-Fe-B thin films with different deposition currents.

5.3.1.2 Effect of *B* on thin film microstructure

In order to study the effect of Boron on the film structure, five Co-Fe-B films were prepared from five individual baths with the same concentration of cobalt and iron using the same applied current (I = 5 mA) but different concentrations of Boron. The compositions of the five individual baths are listed in **Table 5-3**.

Table 5-3. Composition of five individual baths for Co-Fe-B thin film deposition.

Composition	*Bath A*	*Bath B*	*Bath C*	*Bath D*	*Bath E*
$CoCl_2 \cdot 6H_2O$	0.35	0.35	0.35	0.35	0.35
$FeSO_4 \cdot 7H_2O$	0.01	0.01	0.01	0.01	0.01
H_3BO_3	0.73	0.73	0.73	0.73	0.73
Na Citrate ($Na_3C_6H_5O_7 \cdot 2H_2O$)	0.07	0.07	0.07	0.07	0.07
DMAB($BH_3NH(CH_3)_2$)	**0.01**	**0.02**	**0.03**	**0.04**	**0.05**
Glycine($C_2H_5NO_2$)	0.13	0.13	0.13	0.13	0.13
Na Saccharin($C_7H_4NNaO_3S \cdot 2H_2O$)	0.01	0.01	0.01	0.01	0.01

XRD patterns of the three Co-Fe-B films are shown in **Figure 5-3**. All the films were deposited on Cu/Cr pre-coated glass slides respectively. **Figure 5-3** shows that only one broad peak appears on the three XRD patterns in the range of angle $2\theta = 40^o \sim 50^o$ respectively indicative of amorphous Co-Fe-B. Again, two sharp diffraction peaks which correspond to FCC Cu reflections (111) and (200) appearing in each XRD pattern.

Based on Equation (5-1), the sizes of the ordering range were about 80.2 Å, 16.7 Å, 13.6 Å, 15.0 Å and 16.0 Å for the films deposited in baths *A*, *B*, *C*, *D* and *E*, respectively. It was found that 0.03 mol/L of DMAB is the optimized concentration to obtain an amorphous structure for the thin film. Further increase or decrease in the amount of DMAB makes the thin film more crystalline.

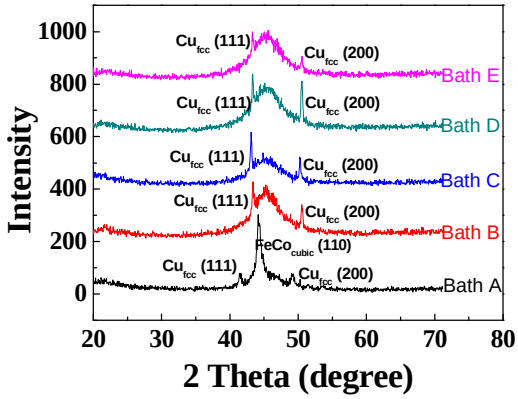

Figure 5-3. XRD patterns of Co-Fe-B thin films with different amount of DMAB.

5.3.1.3 Effect of Fe on thin film microstructure

In order to find the effect of Fe on the film structure, three Co-Fe-B films were prepared using three individual baths with the same deposition current (I = 5mA) and the same amount for the other sources but with different concentrations of $FeSO_4 \cdot 7H_2O$. The compositions of three individual baths are listed in **Table 5-4**.

Table 5-4. Composition of the five individual baths for Co-Fe-B thin film deposition.

Composition	*Bath A*	*Bath B*	*Bath C*
$CoCl_2 \cdot 6H_2O$	0.35	0.35	0.35
$FeSO_4 \cdot 7H_2O$	0.01	0.05	0.1
H_3BO_3	0.73	0.73	0.73
Na Citrate ($Na_3C_6H_5O_7 \cdot 2H_2O$)	0.07	0.07	0.07
DMAB($BH_3NH(CH_3)_2$)	0.03	0.03	0.03
Glycine($C_2H_5NO_2$)	0.13	0.13	0.13
Na Saccharin($C_7H_4NNaO_3S \cdot 2H_2O$)	0.01	0.01	0.01

XRD patterns of the three Co-Fe-B films are shown in **Figure 5-4**. All the films were deposited on Cu/Cr pre-coated glass slides respectively. **Figure 5-4** showed that as the amount of $FeSO_4 \cdot 7H_2O$ increased, the thin film structure became more crystallize. Again, there are two sharp diffraction peaks which correspond to FCC Cu reflections (111) and (200) appearing in each XRD pattern. There are also some unidentified sharp peaks in the diffraction patterns of the thin films from Bath *B* and *C* which are possibly Fe-Co structures. Based on Equation (5-1), the sizes of the ordering range are around 80.2 Å, 16.7 Å, 13.6 Å, 15.0 Å and 16.0 Å for the films deposited from bath *A*, *B* and *C*, respectively. From the XRD results, the optimized concentration of $FeSO_4$ to obtain the amorphous structure is 0.01 mol.

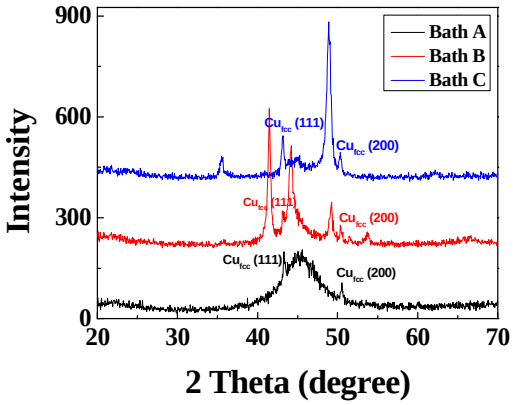

Figure 5-4. XRD patterns of Co-Fe-B thin films with different amount of $FeSO_4$.

Therefore, the optimized composition and deposition current to obtain the most amorphous Co-Fe-B thin film are: DMAB = 0.03 mol, $FeSO_4$ = 0.01 mol and I = 5mA.

5.4 Electrochemical deposition of Co-Fe-B nanobars/nanotubes

Similar to the fabrication of Co-Fe-B thin films, Co-Fe-B nanobars/nanotubes can also be fabricated using the same three electrode configuration method. The only difference would be the working electrode. Co-Fe-B thin film is deposited on a glass slide with a pre-coated Cu/Cr bilayer while Co-Fe-B nanobars/nanotubes are deposited on a gold coated porous polycarbonate membrane with pores in the size of 200 nm. Due to their inert property, these kinds of membranes can be applied in any pH range. The fabrication steps for Co-Fe-B nanobars/nanotubes are shown in **Figure 5-5**.

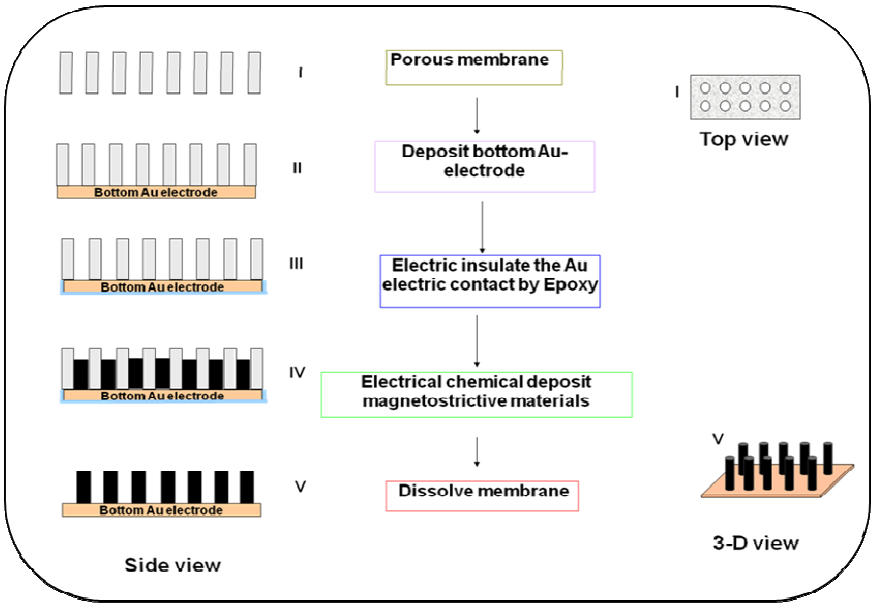

Figure 5-5. Template synthesis of Co-Fe-B nanobars/nanotubes [8].

5.4.1 Effect of deposition conditions on Co-Fe-B nanobars/nanotubes

In this research, the effects of fully gold covered template and partially gold covered template on Co-Fe-B nanobars/nanotubes were studied. The effects of different deposition currents, time, and concentration on Co-Fe-B nanobars/nanotubes were also studied.

The different deposition parameters for studying the effect on Co-Fe-B nanobars/nanotubes are listed in **Table 5-5**. The initial concentration/solution was the same as the bath *B* in **Table 5-4**. In order to make sure the template is partially covered by gold particles, a different sputtering time was tried. By observation using SEM, it was found that under the sputter condition of Sputter time-3 min, Current-28.5 mA, Vacuums-0.09 mbar, Working distance-3 cm, the polycarbonate membrane was partially covered by gold particles. It was also found that under the sputter conditions of Sputter time-6 min, Current-28.5 mA, Vacuums-0.09 mbar, Working distance-3 cm followed by the electro-deposition condition of Deposition time-30 min, Current-5 mA, Working distance-1 cm,

the template was fully gold covered.

Table 5-5. The designed deposition conditions for studying Co-Fe-B nanobars.

Partially gold covered template

(a)

Initial concentration, Deposition current =15mA	
Deposition time (min)	1
	3
	6
	15

(b)

Initial concentration, Deposition time = 3min	
Deposition current (mA)	1
	5
	15

(c)

Deposition current=15mA	
Solution concentration	Deposition time (min)
Initial	6, 15
Diluted to 4X	6, 15

Fully gold covered template

Deposition current=15mA, time =1min	
Solution concentration	Initial
	Diluted to 4X

5.5 Results and discussion

Figure 5-6 shows the SEM images of deposited Co-Fe-B nanobars/nanotubes under different conditions as designed in **Table 5-5**.

Figure 5-6(a). Partially gold covered template, Deposition current: 15 mA, Deposition time: 1 min, initial concentration.

Front view

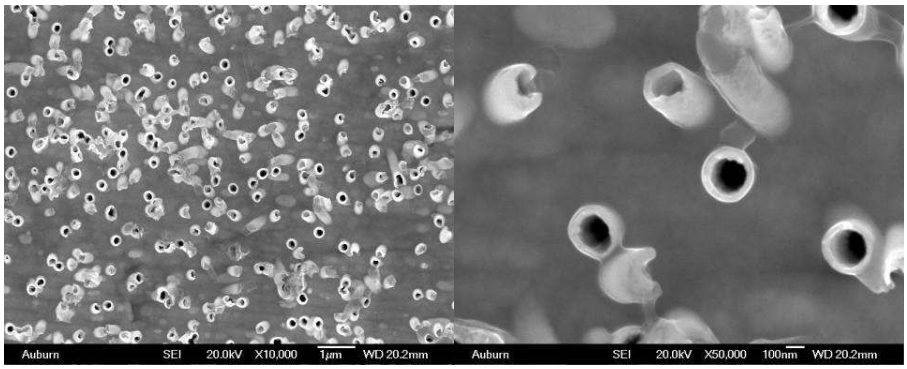

Back view

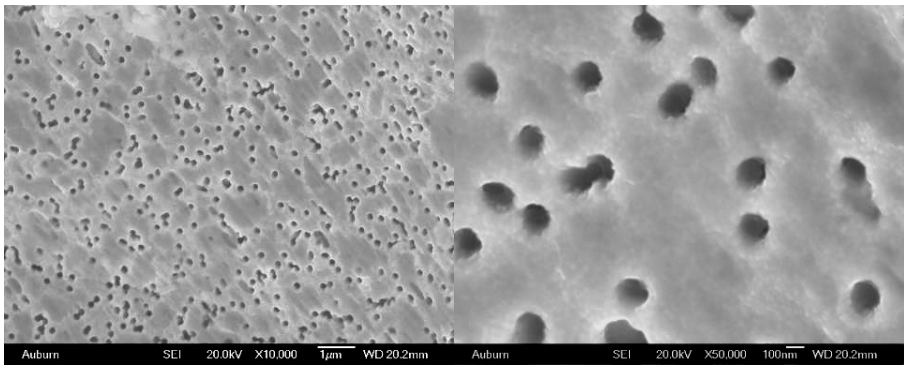

Figure 5-6 (b). Partially gold covered template, Deposition current: 15 mA, Deposition time: 3 min, initial concentration.

Front view

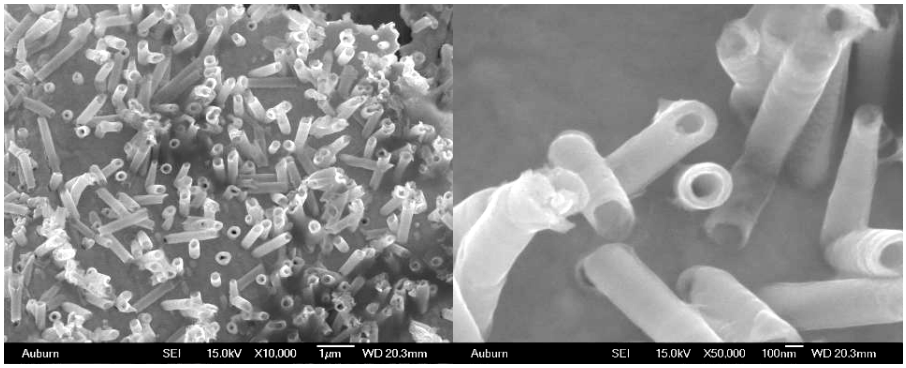

Back view

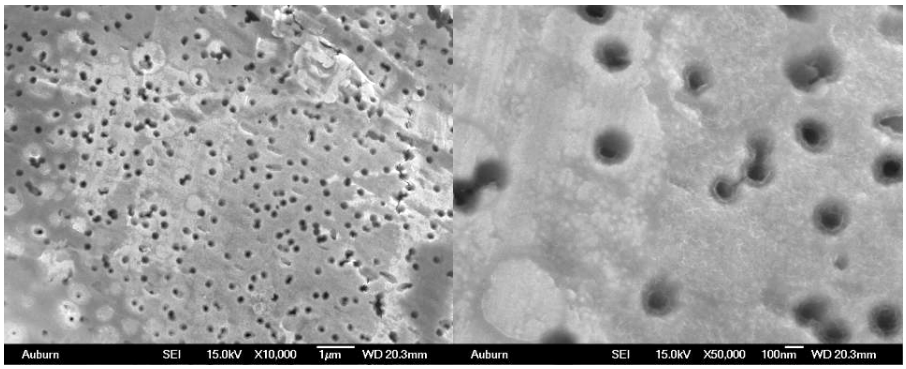

Figure 5-6(c). Partially gold covered template, Deposition current: 15 mA, Deposition time: 6 min, initial concentration.

Front view

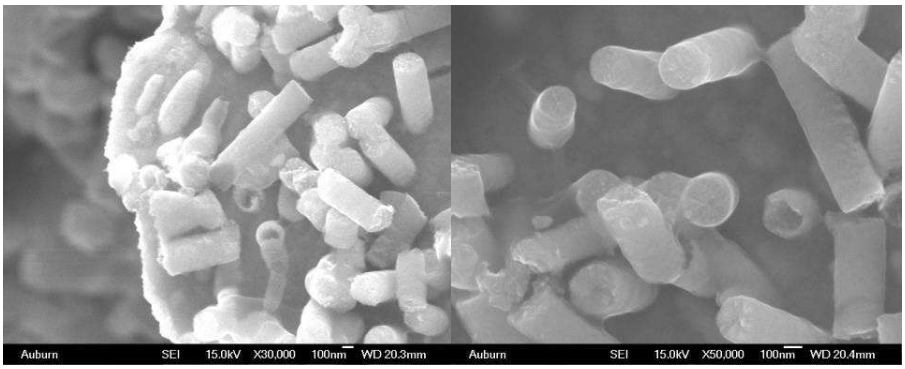

Back view

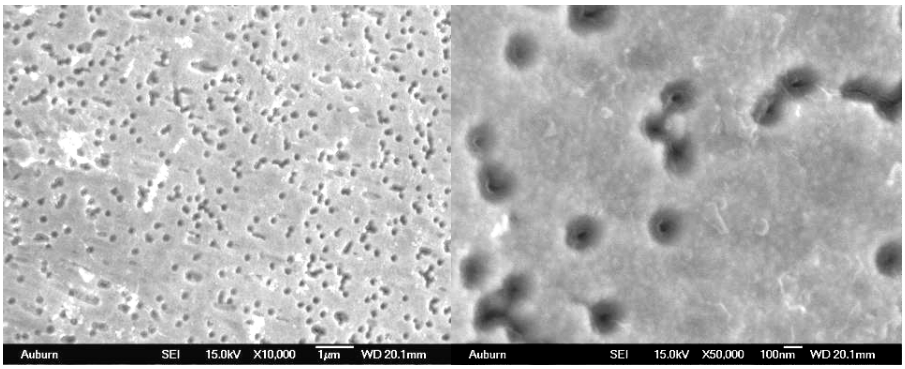

Figure 5-6(d). Partially gold covered template, Deposition current: 15 mA, Deposition time: 15 min, initial concentration.

Front view

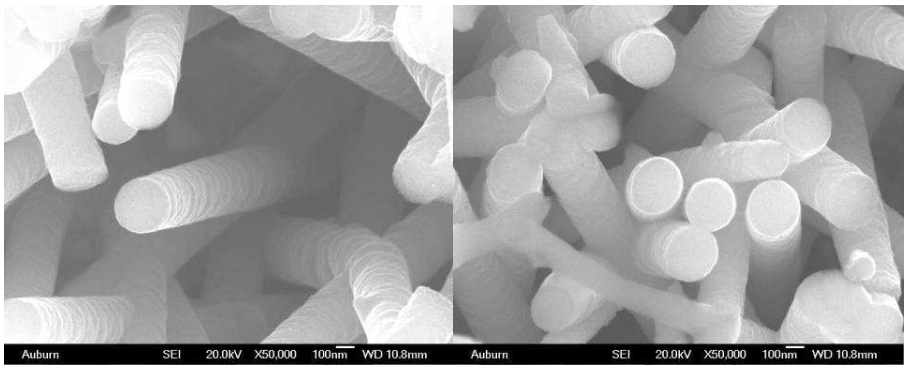

Back view

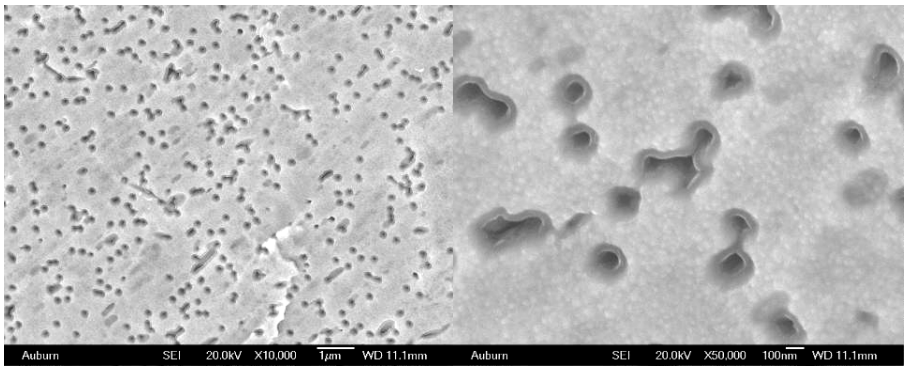

Figure 5-6(e). Partially gold covered template, Deposition current: 1 mA, Deposition time: 3 min, initial concentration.

Front view

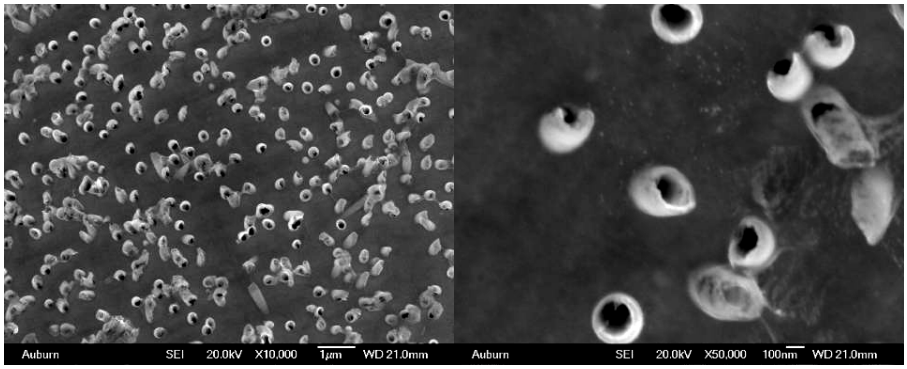

Back view

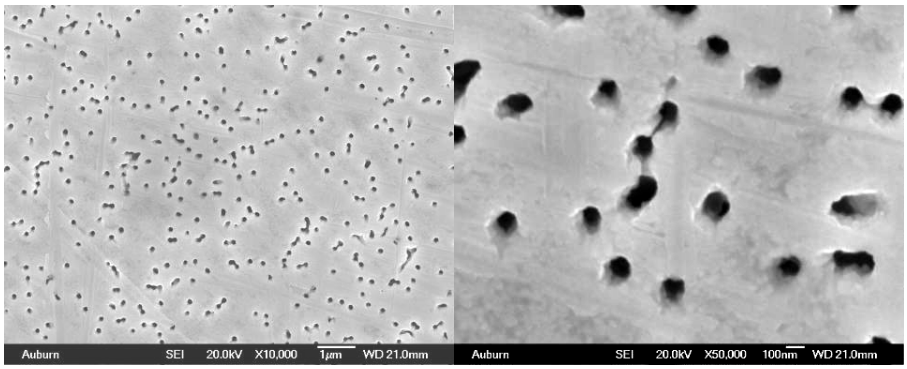

Figure 5-6(f). Partially gold covered template, Deposition current: 5 mA, Deposition time: 3 min, initial concentration.

Front view

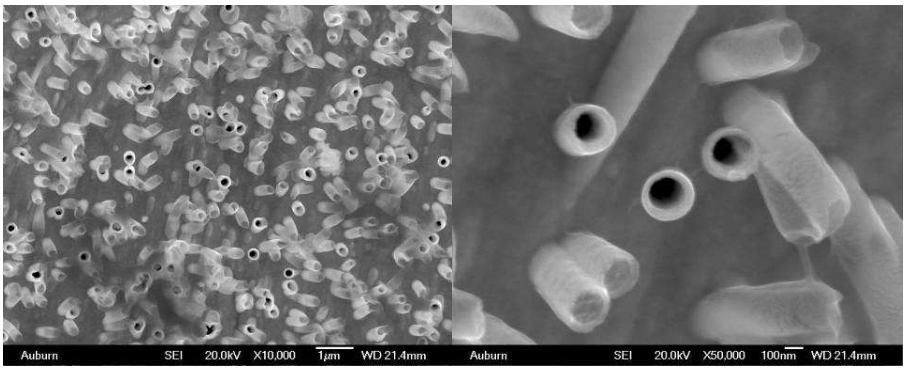

Back view

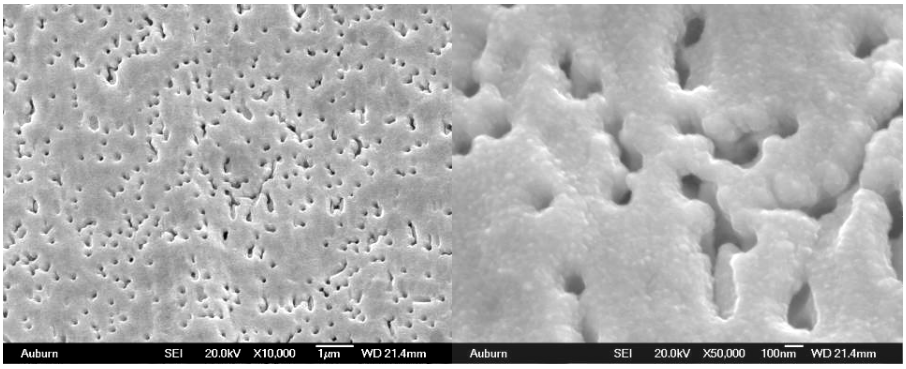

Figure 5-6(g). Partially gold covered template, Deposition current: 10 mA, Deposition time: 15 min, initial concentration.

Front view

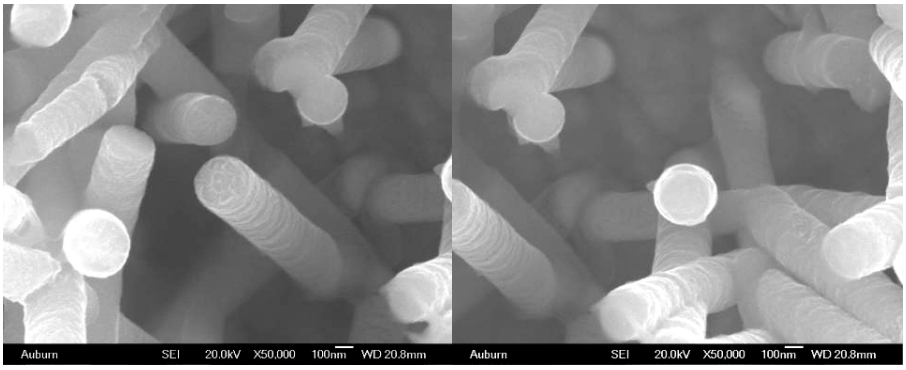

Back view

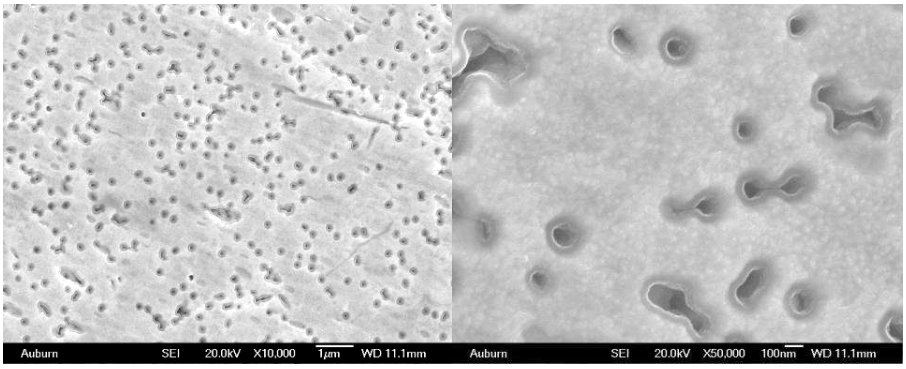

Figure 5-6(h). Partially gold covered template, Deposition current: 15 mA, Deposition time: 6 min, ¼ initial concentrations.

Front view

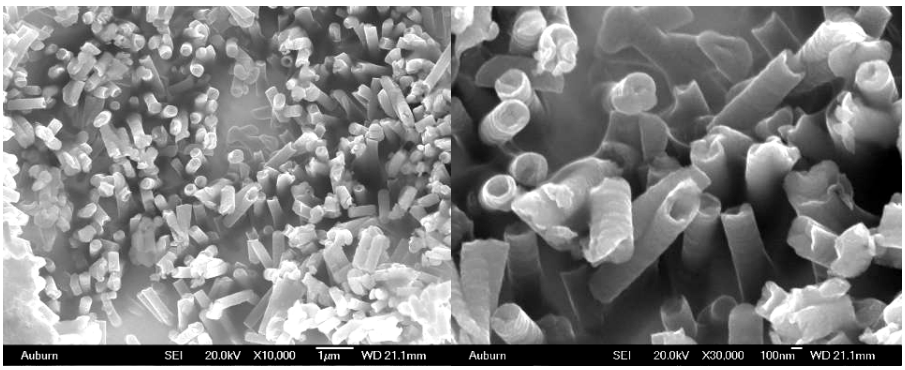

Back view

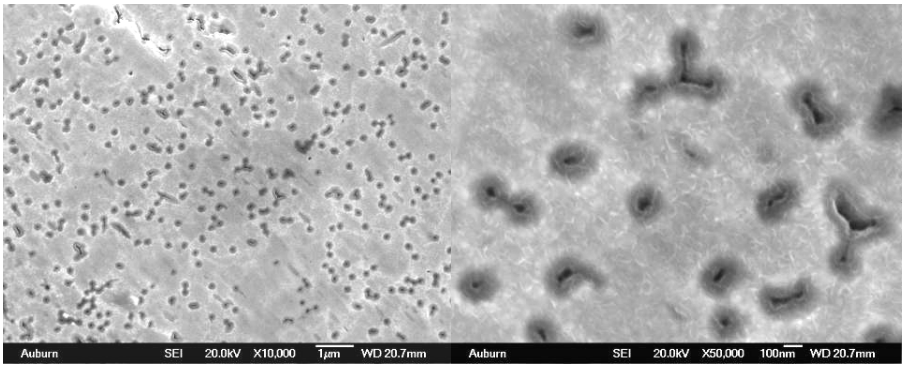

Figure 5-6(i). Partially gold covered template, Deposition current: 15 mA, Deposition time: 15 min, ¼ initial concentrations.

Front view

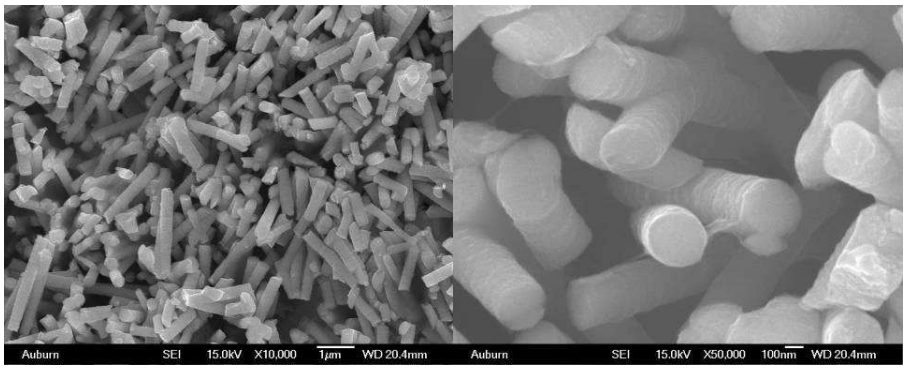

Back view

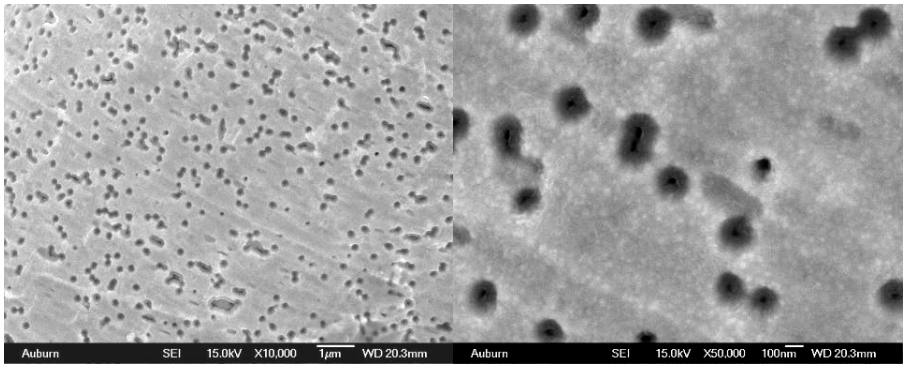

Figure 5-6(j). Fully gold covered template, Deposition current: 15 mA, Deposition time: 1 min, ¼ initial concentrations.

Front view

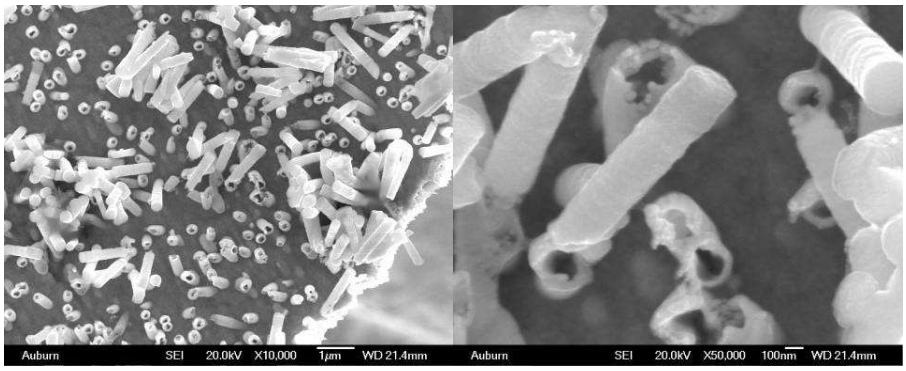

Back view

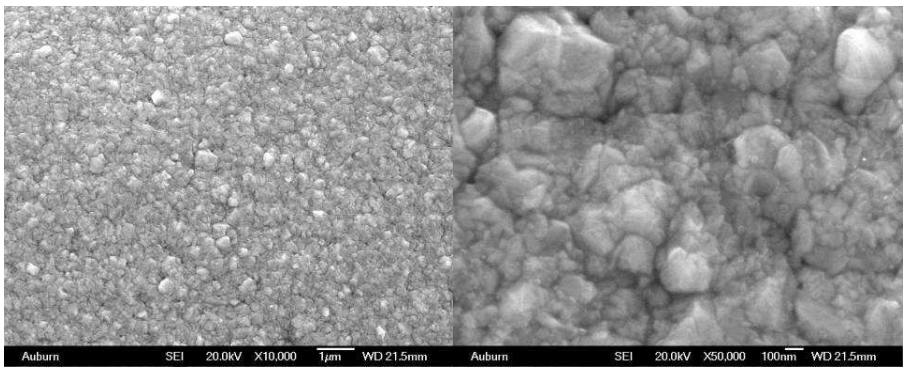

Figure 5-6(k). Fully gold covered template, Deposition current: 15 mA, Deposition time: 1 min, ¼ initial concentrations.

Front view

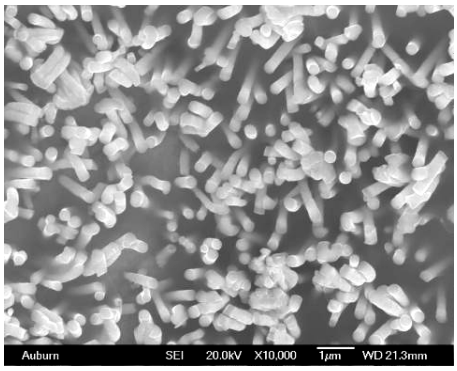

Back view

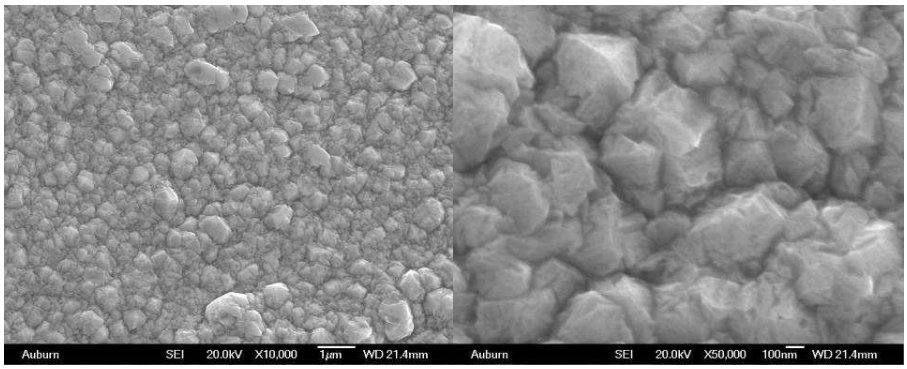

From the SEM images, it was concluded that for the partially gold covered template, nanotubes are obtained when the deposition time is less than 3 mins and that, for the same deposition current, 15 mA, and initial solution. Nanobars are obtained when further increasing deposition time above 6 mins. However, because of the presence of some broken nanobars, it was concluded that the they are actually not complete nanobars but partial nanotubes, partial nanobars. For the same deposition current (15 mA) and time (15 mins), nanobars are obtained for both the initial solution and ¼ concentration of the initial solution and that when further decreasing the deposition time to 6 mins, nanobars are still obtained. The presence of some broken nanobars, however, indicates that they are

actually not complete nanobars but partial nanotubes, partial nanobars. For the same deposition time (3 mins) and same initial solution, change in the deposition current from 1 mA to, 5 mA, to 15 mA, respectively, nanotubes are obtained. However, the length of nanotubes increase as the deposition current increases.

For fully gold covered template, using the same deposition current (15 mA) and time (1 min), nanobars are obtained for the initial solution concentration while nanotubes are obtained at first, followed by nanobars for the ¼ concentration of the initial solution.

The thickness of nanobars/nanotubes under different deposition conditions were listed in **Table 5-6**. It was found that for the same deposition currents (15 mA), as the deposition time increases, the lengths of nanotubes increase at first but that with further increase in deposition time, the length stop increasing. For the same deposition time (3 mA), the lengths of nanotubes increase with the deposition current. For the same deposition current (15 mA) and same deposition time (1 min), change in solution concentration has little effect on the lengths of nanobars/nanotubes. For the same deposition current (15mA), time (1 min) and solution concentration (initial solution), the lengths of nanobars for fully gold covered template are much longer than those of nanotubes for partially gold covered template.

Table 5-6. The dependence of thickness (μm) of Co-Fe-B nanobars/nanotubes on different deposition conditions.

Current (mA) \ Time (min)			1	3	6	15
Partially gold covered	1	Initial		0.15		
	5	Initial		0.45		
	10	Initial				1.0
	15	Initial	0.3	1.0	1.0	1.0
		¼ initial			1.1	2.6
Fully gold covered	15	Initial	1.0			
		¼ initial	1.0			

Several factors are related to the SEM results: deposition current/potential, solution concentration, and deposition time [11-16].

Regarding the electrode shape factor, when gold is sputtered on the porous membrane surface as an electrode, some gold particles may diffuse into the pores and are deposited on the side walls at the bottom pores as shown in **Figure 5-7(a)**. In this case, a high curvature for the gold layers will be formed along the side walls which have a high charge density or electric field and therefore are electrochemically more active relative to the smooth surface, as shown in **Figure 5-7(b)**. Therefore, more electrodeposition will occur along the side walls than perpendicular to the side walls. As a result, nanotubes rather than nanobars will be obtained as shown in **Figure 5-7(c)**. That is the reason why nanotubes are obtained under the same deposition conditions (15 mA, 1 min, and initial solution) for a partially gold covered template while nanobars are obtained for a fully gold covered template.

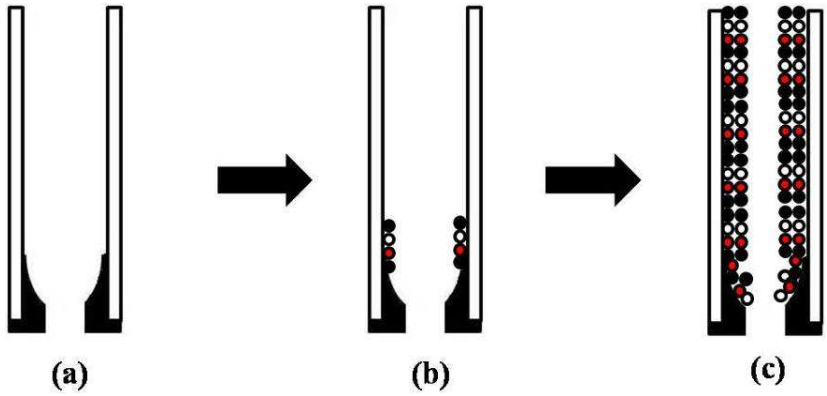

Figure 5-7. Formation process of nanotubes in the case of an annular base electrode. The different color circles denote different deposited ions [11].

Regarding the deposition current/potential factor, when the potential between the working electrode and count electrode is high enough, the deposition speed along the side walls will be much faster than perpendicular to the side walls because the direction of

applied current is parallel to the pores [11-13]. As the applied current/potential increases, longer and thinner nanotubes are expected. On other hand, a lower current/potential will result in nanobars. That is the reason that for the partially gold covered template, the same deposition time (15 min), same solution concentration (initial solution), nanobars are obtained when deposition current is 10 mA, while nanotubes are obtained when deposition current is 15 mA.

Regarding the solution concentration factor, when the solution concentration is low, there will be an insufficient ion supply. In this case, nanotubes are obtained because the ions diffused from bulk solution are deposited along the pore walls due to the interaction of ions and wall surfaces [13]. On other hand, when the solution concentration is higher, there will be enough ions flux into the pores and forms nanobars. That is the reason that for the fully gold covered template, the same deposition current (15 mA) and same deposition time (1 min), nanobars are obtained for an initial solution concentration while nanotubes are obtained for a ¼ of the initial concentration.

Regarding the deposition time factor, when deposition time is shorter, the walls of nanotubes are thinner but when the deposition time is longer, the walls of nanotubes become thicker and thicker and finally form nanobars.

There are some other factors that may affect the formation of nanobars/nanotubes. It is found that for a direct current deposition, the nucleation rate in the growing front increases due to the ion concentration gradient along the wall direction of the template pores, which results in thicker and thicker nanotubes consisting of fine grains, and finally forming caps at the ends of nanotubes as shown in **Figure 5-8**. That is the reason that for a partially gold covered template, for the same deposition current (15 mA) and the same

concentration (initial concentration), nanotubes are obtained when the deposition time is less than 3 mins and nanobars are obtained when the deposition time is more than 6 mins.

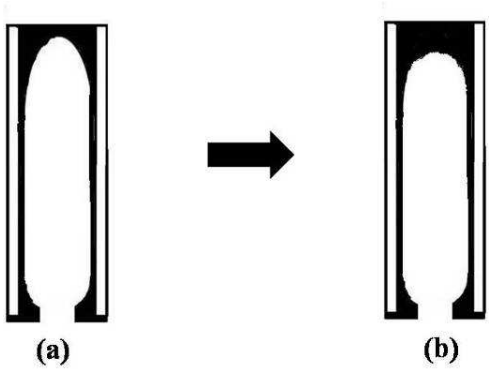

Figure 5-8. Schematic illustration of the transition from nanotube to nanobars with (a) a gradual process and (b) an abrupt process [18].

In all, the growth of nanobars/nanotubes is determined by several factors including deposition current, time, solution concentration, and electrode configuration. Nanotubes are more preferred to be obtained for a partially gold covered template, a higher deposition current, shorter deposition time, and lower solution concentration, while nanobars are more preferred for a lower deposition current, longer deposition time, and higher solution concentration. It is the same case for the fully gold covered template but the deposition current, time, and solution concentration are different to obtain nanobars/ nanotubes. If the other deposition conditions are the same, increases in any one of the conditions' value (except solution concentration) will make the nanobars'/nanotubes' lengths increase.

5.6 Conclusions

Co-Fe-B thin films and nanobars/nanotubes as candidates of magnetostrictive sensor platform have been fabricated using an electrochemical deposition method. The optimized composition of Co-Fe-B thin film for obtaining amorphous structure is found

by using XRD. Based on the SEM results, the deposition conditions including deposition time, deposition current, solution concentration and the configuration of electrodes all can affect the growth of nanobars/nanotubes.

References

1. X.J. Gao, W.Y. Yang, P.F. Pang, S.T. Liao, Q.Y. Cai, K.F. Zeng, and C.A. Grimes, A wireless magnetoelastic biosensor for rapid detection of glucose concentrations in urine samples, Sensors and Actuators B 128 (2007) 161–167.
2. R. Guntupalli, J. Hu, R.S. Lakshmanan, T.S. Huang, J.M. Barbaree, B.A. Chin, A magnetoelastic resonance biosensor immobilized with polyclonal antibody for the detection of *Salmonella typhimurium*, Biosensors and Bioelectronics 22 (2007)1474–1479.
3. S. Huang, H. Yang, R.S. Lakshmanan, M.L. Johnson, J. Wan, I.H. Chen, H.C. Wikle, V.A. Petrenko, J.M. Barbaree, B.A. Chin, Sequential detection of Salmonella typhimurium and Bacillus anthracis spore using magnetoelastic biosensors, Biosensors and Bioelectronics 24 (2009) 1730–1736.
4. W. Shen, R.S. Lakshmanan, L.C. Mathison, V.A. Petrenko, B.A. Chin, Phage coated magnetoelastic micro-biosensors for real-time detection of *Bacillus anthracis* spores, Sensors and Actuators B 137 (2009) 501–506.
5. S.J. Huang, P.F. Pang, X.L. Xiao, L.W. He, Q.Y. Cai, C.A. Grimes, A wireless, remote-query sensor for real-time detection of *Escherichia coli O157:H7* concentrations, Sensors and Actuators B 131 (2008) 489–495.
6. E.T. Lacheisserie, D. Gignoux, M. Schlenker, Magnetism - Materials and Applications, Spring, 2005.

7. M.L. Johnson, J.H. Wan, S.C. Huang, Z.Y. Cheng, V.A. Petrenko, D.J. Kim, I.H. Chen, J.M. Barbaree, J.W. Hong, B.A. Chin, A wireless biosensor using microfabricated phage-interfaced magnetoelastic particles, Sensors and Actuators A 144 (2008) 38–47.
8. S.Q. Li, Development of Acoustic Wave Biosensor Platforms Based on Magnetostriction and Fabrication of Magnetostrictive Nanowires, Dissertation, 1997.
9. M. Ciureanu, F. Beron, L. Clime, P. Ciureanu, A. Yelon, T.A. Ovari, R.W. Cochrane, F. Normandin, T. Veres, Magnetic properties of electrodeposited CoFeB thin films and nanowire arrays. Electrochimica Acta 50 (2005) 4487–4497.
10. B.D. Cullity, Elements of X-ray Diffraction, Prentice Hall, 2001.
11. L.F. Liu, W.Y. Zhou, S.S. Xie, L. Song, S.D. Luo, D.F. Liu, J. Shen, Z.X. Zhang, Y.J. Xiang, W.J. Ma, Y. Ren, C.Y. Wang, G. Wang, Highly Efficient Direct Electrodeposition of Co-Cu Alloy Nanotubes in an Anodic Alumina Template, Journal of Physics Chemical C 112 (2008) 2256-2261.
12. R. Xiao, S. Cho, Ran. Liu, S.B. Lee, Controlled Electrochemical Synthesis of Conductive Polymer Nanotube Structures, Journal of America Chemical Society 129 (2007) 4483–4489.
13. S.I. Cho, W.J. Kwon, S.J. Choi, P. Kim, S.A. Park, J. Kim, S.J. Son, R. Xiao, S.H. Kim, S.B. Lee, Nanotube-Based Ultrafast Electrochromic Display, Advanced Materials 17 (2005) 171 – 175.
14. M. Lai, J.H. Lim, S. Mubeen, Y.W. Rheem, A. Mulchandani, M.A. Deshusses, N.V. Myung, Size-controlled electrochemical synthesis and properties of SnO_2 nanotubes, Nanotechnology 20 (2009) 185602.

15. H.W. Wang, C.F. Shieh, H.Y. Chen, W.C. Shiu, B. Russo, G.Z. Cao, Standing [111] gold nanotube to nanorod arrays via template growth, Nanotechnology 17 **(**2006) 2689–2694.
16. S.I. Cho, S.B. Lee, Fast Electrochemistry of Conductive Polymer Nanotubes: Synthesis, Mechanism, and Application, Account Chemical Research 41 (2008) 699–707.
17. X.R. Li, Yi.Q. Wang, G.J. Song, Z. Peng, Y.M. Yu, X.L. She, J.J. Li, Synthesis and Growth Mechanism of Ni Nanotubes and Nanowires, Nanoscale Research Letter 4 (2009) 1015–1020.
18. X.C. Dou, G.H. Li, X.H. Huang, L. Li, Abnormal Growth of Electrodeposited BiSb Alloy Nanotubes, The Journal of Physical Chemistry C 112 (2008) 8167-8171.

CHAPTER 6

PERSPECTIVES

As a biosensor platform, an MSP provides many unique advantages over other methods. To fully utilize these advantages, different aspects of MSP sensor technology were studied in this work. The results reported here build a solid background for future development of MSP sensor technology.

1) As a foundation for the study, the experimental results reported in Chapter 2 provide some critical information for the understanding of MSP resonators. Further research is needed to study the MSP resonator by researchers in both physics and materials science to determine the correct formula and materials properties used to describe the resonance behavior of a magnetostrictive/magnetoelastic resonator. This kind of research will provide a guideline for the MSP sensor design.
2) It is experimentally demonstrated in Chapter 3 that both the phage and antibody can be used as the sensing element for MSP sensors and can be effectively immobilized onto the MSP surface. Therefore, MSP technology can be developed to fabricate various detection devices for different bacteria. As mentioned in Chapter 1, each pathogen has a different infection dose and the sensitivity of an MSP is directly dependent on its size. That is, the MSP biosensor for detecting a particular pathogen will need to have a certain detection limit, which will require the use of MSPs with a certain size. Due to the successful development of the antibody-immobilized MSPs, MSP technology may be used to monitor the antigen-antibody interaction and other

biological process. Further research on this topic would be interesting. This study also did not examine the temperature stability of antibody based sensors. It would, therefore, be critical and is an interesting topic to study the influence of the storage temperature on the performances of these sensors for detection of bacteria.

3) The following were demonstrated in Chapter 3: nonspecific binding is strongly dependent on the target species and the biological background matrix of the analyte; the reference sensor is a great approach for monitoring nonspecific binding; and different blocking agents have different blocking efficiency. Therefore, for a type of MSP biosensor designed for the detection of a particular pathogen, the blocking agent may need to vary, depending on the background of the real analyte to be tested. That is, the MSP biosensors for the detection of the same pathogen may need to have different blocking agents.

4) The development of a handheld device to interrogate the MSP sensor is critical to the development of MSP technology to be used for in-field tests. As mentioned in Chapter 4, both the frequency-domain and time-domain technologies should be studied since each has some advantages and drawbacks. The utilization of either would be dependent on the application.

4.1) For the frequency-domain technology, the indirect approach introduced and studied here provides new method for the development of handheld devices to interrogate the MSP sensors. This approach should be further studied to reduce the cost of the device and further miniaturize circuitry by selecting different chips. It would be valuable to have a LCD display integrated with the handheld device so that a computer would not be needed. As discussed in Chapter 4, the experimental results

and theoretical simulation indicate that the signal can be enhanced by using an additional capacitor. It would be of great interest to have a capacitor with changeable capacitance to be integrated with the handheld device so that the capacitance of this additional capacitor can be optimized for each MSP sensor. With the current indirect approach, it is the potential ratio of the sensor channel to a reference channel that is used in the signal characterization. It would be valuable to use the potential difference between the sensor channel and a reference as the signal for characterization. Additionally, as demonstrated in Chapter 3, a reference sensor can be used to monitor nonspecific binding. Therefore, it would be of interest to use the reference sensor as the reference channel for characterization and to determine whether or not this will further enhance the signal.

4.2) For the time-domain technology, a way to generate a strong magnetic pulse should be studied and integrated with the handheld device. Additionally, the way to enhance the signal should be exploited, which is critical for MSP sensors having a smaller size. One possible method is to have a permanent/constant dc bias applied to the MSP sensors. Another possible way would be to use repeated pulses to enhance the driving power at frequencies close to the characteristic frequency.

5) The smaller the MSP, the higher the sensitivity. The micro/nano-MSPs including nanobars and nanotubes may have unprecedented sensitivity. However, these MSPs also have a very high resonance frequency. The characterization of these MSPs at high frequency is critically needed. In this work, the amorphous Co-Fe-B alloy has been prepared in different forms, such as thin film, nanobars, and nanotubes. It would be useful to study the magnetostrictive effect of these materials at high frequency.